

The  
University  
Of  
Sheffield.

# Implementation of FAST-*forge* for Ti-5Al-5Mo-5V-3Cr and Ti-Ti composites

Emma Lucy Calvert

A thesis submitted in partial fulfilment of the requirements for the degree of  
Doctor of Philosophy

The University of Sheffield  
Department of Materials Science and Engineering

February 2019





# Abstract

Titanium alloys are desired by aerospace manufacturers such as Safran Landing Systems due to their higher strength-to-weight ratio and improved corrosion resistance over steels. However, the expense of producing titanium has limited its use for applications such as landing gear.

The aim of this project was to investigate an alternative process which would significantly reduce the number of processing steps for a metastable  $\beta$  titanium alloy, Ti-5Al-5Mo-5V-3Cr (Ti-5553), used in landing gear.

The alternative process consists of: using field-assisted sintering technology (FAST) to heat and consolidate powder into a solid billet, by the application of direct current; forging the billet in one-step; and heat treating to produce an optimal microstructure. This process is known as the FAST-*forge* process.

Initial small-scale FAST testing found that the  $\beta$  grain size could be controlled by adjusting the dwell temperature and time, which is not possible with conventional processing. Subsequent large-scale FAST testing was used to produce FAST billets, some of which were compressed to generate flow data, and one was industrially forged and heat treated: the flow curves and microstructures produced were found to be similar to those of conventionally produced Ti-5553. A microstructural prediction model was subsequently generated to predict the microstructure from the stress, and tested on a FAST-produced complex-shaped forging, which demonstrated the capability of FAST-*forge* to produce aerospace components. Composites of hard Ti-15.8Fe-36.6Mo alloy particles within a Ti-5553 matrix were produced with full diffusion bonding and an increase in compressive strength of  $>200$  MPa compared to un-reinforced Ti-5553.

Overall, FAST-*forge* has been found to be a viable process for a metastable  $\beta$  alloy such as Ti-5553, and gives greater versatility in producing composites to improve the strength. If an inexpensive powder can be produced, this process should make titanium alloys more affordable for a wide variety of applications and industries.

# Acknowledgements

I would like to thank my supervisors, Dr Martin Jackson and Prof Brad Wynne, for all their help and support throughout my project.

I would also like to thank my industrial sponsor Safran Landing Systems for providing funding and the material used in this thesis, and the Engineering and Physical Sciences Research Council for funding this project.

Special thanks go to all the technicians and researchers who have helped me throughout my project, including, but not limited to, Dr Alexander Knowles, Dr Phil Mahoney for performing nanoindentation, Mr Dean Haylock, Dr Nick Weston, Dr Ben Thomas, and Dr Jacob Pope, and I would like to thank Prof Nicola Morley for her PGR welfare support.

Thanks also go to everyone in D1 who have helped with discussions and practical work, and have generally made an enjoyable environment to work in.

I would finally like to thank all my friends in Sheffield who have made my experience at Sheffield so worthwhile.

I would like to dedicate this thesis to my family and thank them for their never-ending support, without which I never would have succeeded in finishing this thesis.

# Contents

<b>Abstract</b>	<b>ii</b>
<b>Acknowledgements</b>	<b>iii</b>
<b>1 Introduction</b>	<b>1</b>
1.1 Project aims and objectives . . . . .	3
1.2 Thesis outline . . . . .	3
<b>2 Literature Review</b>	<b>5</b>
2.1 Discovery of Titanium . . . . .	5
2.2 Titanium metallurgy . . . . .	6
2.2.1 Slip mechanisms in titanium . . . . .	6
2.2.2 Diffusion in titanium . . . . .	7
2.2.3 Titanium alloy classification . . . . .	8
2.2.3.1 $\alpha$ alloys . . . . .	8
2.2.3.2 $\alpha + \beta$ alloys . . . . .	9
2.2.3.3 $\beta$ titanium alloys . . . . .	11
2.2.3.4 Ti-5Al-5Mo-5V-3Cr . . . . .	12
2.3 Conventional processing of titanium . . . . .	13
2.3.1 Thermomechanical processing of $\beta$ titanium alloys . . . . .	14
2.3.2 Thermomechanical processing of Ti-5553 . . . . .	16
2.3.2.1 Effect of $\omega$ phase on thermomechanical processing of Ti-5553 . .	18
2.4 Novel processing route - FAST- <i>forg</i> e process . . . . .	19
2.4.1 Field-assisted sintering technology (FAST) . . . . .	19
2.4.1.1 Mechanism of FAST process . . . . .	20
2.4.1.2 Advantages of FAST . . . . .	21
2.4.1.3 Uses of FAST . . . . .	22
2.4.1.4 Titanium produced by FAST . . . . .	23

<b>3</b>	<b>Experimental Procedure</b>	<b>24</b>
3.1	Powder production . . . . .	24
3.2	Field-assisted sintering technology . . . . .	26
3.2.1	Small-scale FAST specimens . . . . .	28
3.2.2	Large-scale FAST specimens . . . . .	28
3.3	Compression testing . . . . .	29
3.3.1	High temperature compression testing . . . . .	29
3.4	Solution heat treatment and ageing . . . . .	31
3.5	Analysis techniques . . . . .	32
3.5.1	$\beta$ transus temperature determination . . . . .	32
3.5.2	Sample preparation . . . . .	32
3.5.3	Light microscopy . . . . .	33
3.5.4	Scanning electron microscopy . . . . .	33
3.5.5	Transmission electron microscopy . . . . .	34
3.5.6	Microhardness testing . . . . .	34
3.5.6.1	Post-FAST specimens . . . . .	34
3.5.6.2	Post-compressed, solution heat treated, and aged cone specimens	34
3.5.6.3	Forged and heat treated specimens . . . . .	34
3.5.7	Density measurements . . . . .	35
3.5.8	$\alpha$ volume fraction measurements . . . . .	35
3.5.9	Error . . . . .	35
3.5.10	$\beta$ grain size measurements . . . . .	36
3.5.11	Flow stress analysis . . . . .	37
3.5.11.1	Isothermal correction . . . . .	38
3.5.11.2	Friction correction . . . . .	39
3.5.12	Finite element modelling (FEM) . . . . .	40
3.5.12.1	Compression of cylindrical specimens . . . . .	40
3.5.12.2	Compression of double truncated cones . . . . .	40
3.5.12.3	Large-scale forging of double truncated cones . . . . .	40
3.5.12.4	Complex ‘eye bolt’ forging . . . . .	41
<b>4</b>	<b>Small-scale FAST of Ti-5553</b>	<b>42</b>
4.1	Outline . . . . .	42
4.2	Results . . . . .	43
4.2.1	Microstructural examination . . . . .	43

4.2.1.1	Below $\beta$ transus temperature . . . . .	43
4.2.1.2	Above $\beta$ transus temperature . . . . .	43
4.2.2	$\alpha$ volume fraction measurements . . . . .	44
4.2.3	$\beta$ grain size measurements . . . . .	46
4.2.4	Density calculations . . . . .	46
4.3	Discussion . . . . .	49
4.3.1	Analysis of specimens produced below the $\beta$ transus . . . . .	49
4.3.2	Analysis of specimens produced above the $\beta$ transus . . . . .	49
4.4	Conclusions . . . . .	52
<b>5</b>	<b>Large-scale FAST of Ti-5553</b>	<b>53</b>
5.1	Outline . . . . .	53
5.2	Experimental procedure . . . . .	54
5.2.1	Large-scale forging study . . . . .	54
5.3	Results . . . . .	56
5.3.1	Analysis of post-FAST billets . . . . .	56
5.3.1.1	Density . . . . .	56
5.3.1.2	Microstructural evolution . . . . .	56
5.3.1.3	Microhardness . . . . .	56
5.3.1.4	Transmission electron micrographs . . . . .	57
5.3.2	Analysis of compressed Ti-5553 cylinders . . . . .	59
5.3.2.1	Microstructural evolution and FEM modelling . . . . .	59
5.3.2.2	Flow curves . . . . .	59
5.3.3	Analysis of compressed and heat treated Ti-5553 cone specimens . . . . .	64
5.3.3.1	Microstructural evolution and FEM modelling . . . . .	64
5.3.3.2	Microhardness . . . . .	65
5.3.4	Analysis of large-scale forged and heat treated Ti-5553 specimens . . . . .	68
5.3.4.1	Microstructural evolution and FEM modelling . . . . .	68
5.3.4.2	Microhardness of solution heat treated and aged specimens . . . . .	71
5.3.4.3	Transmission electron micrographs . . . . .	71
5.4	Discussion . . . . .	74
5.4.1	Comparison between post-FAST, post-compression, and forged microstructures . . . . .	74
5.4.2	Cylindrical compression testing study . . . . .	75
5.4.3	Cone compression testing and heat treatment study . . . . .	77

5.4.4	Large-scale forging and heat treatment study . . . . .	78
5.4.5	Powder to heat treated Ti-5553 billet in three steps . . . . .	79
5.5	Conclusions . . . . .	82
<b>6</b>	<b>Microstructural prediction model and complex Ti-5553 forging</b>	<b>84</b>
6.1	Outline . . . . .	84
6.2	Literature review . . . . .	85
6.3	Experimental procedure . . . . .	87
6.3.1	Derivation of Bate-Brooks constant values . . . . .	87
6.3.2	Prediction of $\lambda$ from strain . . . . .	89
6.3.3	Image analysis of $\alpha$ phase . . . . .	89
6.3.4	Complex Ti-5553 ‘eye bolt’ forging . . . . .	90
6.4	Results . . . . .	92
6.4.1	Predicted flow stress . . . . .	92
6.4.2	Relationship between $\lambda$ and $\alpha$ phase microstructural parameters . . . . .	95
6.4.3	Forged Ti-5553 ‘eye bolt’ specimen . . . . .	97
6.4.3.1	Microstructural examination and FEM . . . . .	97
6.4.3.2	$\alpha$ phase analysis . . . . .	98
6.5	Discussion . . . . .	100
6.5.1	Bate-Brooks microstructural prediction model . . . . .	100
6.5.2	Forged Ti-5553 ‘eye bolt’ specimen . . . . .	101
6.6	Conclusions . . . . .	104
<b>7</b>	<b>FAST of Ti-5553–TiFeMo Composites</b>	<b>106</b>
7.1	Outline . . . . .	106
7.2	Literature review . . . . .	107
7.2.1	Current reinforcement methods for Ti-5553 . . . . .	107
7.2.2	TiFeMo alloy . . . . .	107
7.2.3	Detection of $\omega$ phase using TEM diffraction patterns . . . . .	108
7.3	Experimental procedure . . . . .	110
7.3.1	TiFeMo powder . . . . .	110
7.3.2	FAST production . . . . .	110
7.3.3	Compression testing . . . . .	111
7.3.4	Solution heat treatment and ageing . . . . .	111
7.3.5	Microscopy . . . . .	111

7.3.6	$\beta$ grain size measurements . . . . .	111
7.3.7	Chemical analysis line scans . . . . .	112
7.3.8	Micro- and nanohardness testing . . . . .	112
7.4	Results . . . . .	113
7.4.1	Microstructural examination . . . . .	113
7.4.2	Compression testing and microhardness . . . . .	113
7.4.3	Interdiffusion region analysis . . . . .	116
7.4.4	TEM lamella analysis . . . . .	117
7.5	Discussion . . . . .	121
7.5.1	Microstructural examination and microhardness testing . . . . .	121
7.5.2	Interdiffusion region analysis . . . . .	122
7.5.3	Future applications . . . . .	123
7.6	Conclusions . . . . .	124
<b>8</b>	<b>Conclusions</b>	<b>125</b>
8.1	Small-scale FAST of Ti-5553 . . . . .	125
8.2	Large-scale FAST of Ti-5553 . . . . .	126
8.3	Microstructural prediction of Ti-5553 produced by FAST- <i>forg</i> e . . . . .	127
8.4	Ti-5553–TiFeMo composites produced by FAST- <i>forg</i> e . . . . .	129
<b>9</b>	<b>Future Work</b>	<b>130</b>
<b>10</b>	<b>Appendix</b>	<b>132</b>
10.1	Rights and Permissions . . . . .	134



# List of Figures

1.1	The conventional multi-step processing route for producing forged titanium alloy components . . . . .	1
1.2	The novel FAST- <i>forg</i> e processing route for low-cost titanium alloy particulate feedstock . . . . .	2
2.1	Structures of the unit cells of (a) the $\alpha$ (hcp) and (b) the $\beta$ (bcc) phase . . . . .	6
2.2	The transformation of $\beta$ to $\omega$ phase in the incomplete (incommensurate) and complete (ideal) forms . . . . .	7
2.3	Effect of alloying element additions on the $\alpha$ and $\beta$ phases and the $\beta$ transus temperature . . . . .	8
2.4	$\beta$ isomorphous phase diagram indicating the three main classifications of titanium alloys . . . . .	9
2.5	A breakdown of the estimated cost of producing a 2.5 cm (1 inch) thick titanium plate by the conventional processing route . . . . .	14
2.6	An example of a $\beta$ annealed microstructure, $\beta$ -CEZ . . . . .	15
2.7	An example of a $\beta$ processed microstructure, Ti-6246 . . . . .	15
2.8	An example of a bi-modal microstructure, $\beta$ -CEZ . . . . .	16
2.9	Flow curves for Ti-5553 in the $\beta$ forged condition, forged at strain rates of 0.001, 0.01, and 0.1 s <sup>-1</sup> and temperatures of (a) 785°C, (b) 810°C, and (c) 835°C . . . . .	17
2.10	Flow curves for Ti-5553 in the $\alpha + \beta$ condition, forged at strain rates of 0.001, 0.01, and 0.1 s <sup>-1</sup> and temperatures of 785°C, 810°C, and 835°C . . . . .	17
2.11	Experimental set-up of the FAST process . . . . .	19
2.12	Theorised mechanism of the FAST process, where coulomb discharge is equivalent to joule heating . . . . .	20
3.1	Light micrographs of (a) Batch 1 and (b) Batch 2 of gas atomised Ti-5553 powder . . . . .	25

3.2	Annotated photographs of: (a) the FAST machine at Kennametal Manufacturing UK Ltd which was used to produce large-scale FAST specimens; (b) gas atomised Ti-5553 powder being poured into the cylindrical graphite die; (c) the punch-die-powder assembly ready to be placed into the FAST machine; and (d) a punch-die-powder assembly being raised into the furnace . . . . .	26
3.3	Typical pressure and temperature profiles for large-scale FAST testing . . . . .	28
3.4	Thermomechanical compression testing: (a) dimensions of cylindrical specimens, (b) dimensions of double truncated cone specimens, (d) annotated photograph of the thermomechanical compression machine, with (c) close-up of a specimen in the gripper arms . . . . .	30
3.5	$\beta$ transus temperature approach curve . . . . .	33
4.1	BSEI micrographs of FAST specimens produced at 3, 10, 30, and 60 min dwell times for temperatures of (a) 800°C, and (b) 850°C . . . . .	43
4.2	BSEI micrographs of FAST specimens produced at 3, 10, 30, and 60 min dwell times for temperatures of (a) 900°C, (b) 930°C, (c) 970°C, and at a 3 min dwell time only for (d) 1000°C . . . . .	44
4.3	BSEI micrographs of FAST specimens produced at 3, 10, 30, and 60 min dwell times for temperatures of (a) 1000°C, and (b) 1200°C . . . . .	45
4.4	FAST specimens produced at 800 and 850°C: effect of dwell time on (a) $\alpha$ volume fraction and (b) density . . . . .	45
4.5	Mean $\beta$ grain size against dwell temperature for various FAST dwell times . . . .	47
4.6	Mean $\beta$ grain size against dwell time for various FAST dwell temperatures . . . .	47
4.7	Mean density against dwell time for dwell temperatures 850–1200°C. Errorbars were not plotted to ensure that the mean densities could be easily interpreted. However, the relative accuracy of the mean density was calculated to be 1.57 % .	48
5.1	Examples of (a) a specimen produced by FAST, and (b) a double truncated cone machined from the FAST billet for forging . . . . .	54
5.2	Photographs of large-scale forging of the double truncated cones (a) before forging and (b) after forging, and (c) the 2100 t screw press at the Advanced Forming Research Centre (AFRC) which was used for the large-scale forging . . . . .	55

5.3	Diagram indicating where the specimens for microstructural examination, microhardness, and transmission electron microscopy (TEM) were taken from in the forged and heat treated halves of the forged cones (the thick black line indicates the faces observed under microscopy and used for microhardness testing) . . . . .	55
5.4	Comparison between (a) a light micrograph of Ti-5553 gas atomised powder, and BSEI micrographs of FAST specimens produced at 850, 930, and 1000°C for (b) low, (c) medium, and (d) high resolution . . . . .	57
5.5	Transmission electron micrographs of FAST specimens produced at 930 and 1000°C (bright field) . . . . .	58
5.6	BSEI micrographs of the specimens compressed at $1\text{ s}^{-1}$ at high strain (centre) and low strain (edge), for all FAST conditions. An example of an FEM simulation, of the specimen produced by FAST at a dwell temperature of 1000°C and compressed at 785°C and $1\text{ s}^{-1}$ , indicates where the high and low effective strain values were taken from. The compression direction is in line with the page . . . .	60
5.7	Flow curves of FAST specimens produced at 850, 930, and 1000°C, and compressed at temperatures 785, 810, and 835°C and strain rates of 0.01, 0.1, 1, and $5\text{ s}^{-1}$ . . . . .	61
5.8	Selected BSEI micrographs of the double truncated cones which have been (a) compressed at 785°C and $0.1\text{ s}^{-1}$ at high strain (centre), (b) subsequently solution heat treated, and (c) and (d) aged at 500°C for 4 h at high strain (centre) and low strain (edge), respectively, for all FAST conditions. An example of an FEM simulation, of the specimen produced by FAST at a dwell temperature of 1000°C, indicates where the high and low effective strain values were taken from. The compression direction is in line with the page . . . . .	66
5.9	Microhardness of Ti-5553 in the post-FAST, post-compression, post-solution heat treatment (ST), and post-aged conditions. All heat treatment conditions were performed following compression of the post-FAST cones (at 785°C and $0.1\text{ s}^{-1}$ ), and all ageing conditions were performed following the same solution heat treatment (785°C for 2 h) . . . . .	67
5.10	BSEI micrographs of the double truncated cone forged at 785°C, and heat treated between 750 and 850°C for 4 h and below 650°C for 8 h (HT). Micrographs were taken from the centre (high strain) to the edge (low strain) of the forged and heat treated specimens. The FEM simulation indicates the strain distribution within the forged specimen. The forging direction is in line with the page . . . . .	69

5.11	BSEI micrographs of double truncated cones forged at 810 and 835°C, and heat treated between 750 and 850°C for 4 h and below 650°C for 8 h (HT). Micrographs were taken from the centre (high strain) and the edge (low strain) only. The forging direction is in line with the page . . . . .	70
5.12	Microhardness variation from the centre (0 mm) to the edge (30 mm) of the heat treated specimens forged at 785, 810, and 835°C, with the average of all the microhardness values indicated by the horizontal lines. The microstructure corresponding to the microhardness values is shown in Figures 5.10 and 5.11. A vickers indenter with 4.905 N load was used . . . . .	72
5.13	High and low strain microstructures of the heat treated specimen forged at 810°C when imaged by: (a) and (c) transmission electron microscopy (bright field), and (b) BSEI. The forging direction is in line with the page for (b) only . . . . .	73
5.14	Flow chart illustrating the FAST- <i>forg</i> e process: from powder to heat treated specimen in three steps. BSEI micrographs of post-FAST, forged, and heat treated specimens are shown, with a light micrograph of gas atomised Ti-5553 powder, and photographs of the powder, a machined post-FAST double truncated cone, and a forged cone. FAST and forging directions are in line with the page. A BSEI micrograph of conventionally produced Ti-5553, which has been heat treated using the same temperatures and durations, is shown inside the dashed lines for comparison . . . . .	80
6.1	An example of $\alpha$ phase analysis including: (a) feret minimum, (b) feret maximum, and (c) $\alpha$ area, performed using ImageJ image analysis software . . . . .	90
6.2	Machined Ti-5553 bar produced by FAST at 1000°C, prior to forging . . . . .	90
6.3	Closed-die multi-blow forging of the near-net shaped ‘eye bolt’ at W.H. Tildesley Ltd: (a) starter (left) and finisher (right) dies, (b) forged specimen after second blow on the starter die, (c) forged specimen after tenth blow on the finisher die, and (d) closed-die drop forge . . . . .	91
6.4	Stresses predicted by the Bate-Brooks model compared to the experimental stresses for Ti-5553 produced by FAST at 930°C. The Bate-Brooks constant values derived from the model, Table 6.1, were used. Some tests were excluded due to under or over-heating during compression testing. The error was 20.66 % . . . .	93

6.5	Stresses predicted by the Bate-Brooks model compared to the experimental stresses for Ti-5553 produced by FAST at 1000°C. The Bate-Brooks constant values derived from the model, Table 6.1, were used. Some tests were excluded due to under or over-heating during compression testing. The error was 20.82 % . . . . .	94
6.6	Relationship between the measured mean feret minimum values and $\lambda$ , with different strain rates and FAST temperatures (930 and 1000°C) shown, and mid-radius points confirming the accuracy of the derived relationship . . . . .	95
6.7	Relationship between the measured median $\alpha$ area values and $\lambda$ , with different strain rates and FAST temperatures (930 and 1000°C) shown, and mid-radius points confirming the accuracy of the derived relationship . . . . .	96
6.8	Relationship between the measured aspect ratio values and $\lambda$ for different strain rates and FAST temperatures (930 and 1000°C), and mid-radius points confirming the accuracy of the derived relationships . . . . .	96
6.9	Forged Ti-5553 ‘eye bolt’ specimen and its FEM simulation, which shows the effective strain imparted during forging. Vertical lines indicate where the forged specimen was sectioned to produce a slice for microstructural examination (see Figure 6.10) and the corresponding slice taken from the FEM simulation. The forging direction is into the page . . . . .	97
6.10	FEM simulation slice of the forged Ti-5553 ‘eye bolt’ specimen, corresponding to the vertical line in Figure 6.9. Positions 1–7 indicate the progression from low to high strain throughout the forged specimen, with the corresponding microstructures shown. The forging direction is in line with the page . . . . .	98
7.1	Selected area diffraction patterns of: (a) the commensurate (ideal) $\omega$ phase (Zr-Nb alloy), (b) solution treated and quenched Ti-5553, showing the athermal incommensurate (partial) $\omega$ phase with diffuse streaking, and (c) aged Ti-5553, showing the $\alpha$ and $\beta$ phases. Key diagrams of: (d) the diffraction pattern shown in (c), (e) the position of the commensurate (ideal) $\omega$ phase, (f) the position of the incommensurate (partial) $\omega$ phase with smeared reflections, seen in Ti-Cr and Ti-V alloys, and (g) the position of the incommensurate $\omega$ phase seen in Ti-Fe alloys, where the open circles are bcc $\beta$ phase reflections and the shaded circles are $\omega$ phase reflections . . . . .	109

7.2	Low magnification BSEI micrographs of Ti-5553 (30 min dwell) and Ti-5553–TiFeMo composites: (a) post-FAST and (c) post-compression. High magnification BSEI micrographs of Ti-5553 (30 min dwell) and Ti-5553–TiFeMo composites: (b) post-FAST; (d) post-compression; and (e) post-compression, solution treat and age . . . . .	114
7.3	BSEI micrographs of a (a) TiFeMo particle (white) surrounded by the Ti-5553 matrix (dark grey). $\beta$ grains can be seen to co-exist in the Ti-5553 and TiFeMo, and (b) a microcrack in a TiFeMo particle larger than 100 $\mu\text{m}$ , in the Ti-5553–10 wt.% TiFeMo compressed specimen . . . . .	115
7.4	BSEI micrographs of the Ti-5553–25 wt.% TiFeMo post-aged composite, showing: (a) and (b) the infrequent dark nano-scale B2 TiFe intermetallic precipitates present adjacent to dark micron-sized Fe-rich prior interdendritic particles in the TiFeMo particles, and (b) the nanoindents within the TiFeMo particle in Figure 7.6e in higher resolution . . . . .	115
7.5	Mechanical properties: (a) Flow curves of Ti-5553 (i.e. 0 wt.% TiFeMo, 30 min dwell) and Ti-5553–25 wt.% TiFeMo specimens compressed at room temperature, and (b) microhardness for all compositions and conditions: post-FAST; post-compression; and post-compression, solution treat and age . . . . .	116
7.6	Interdiffusion region of Ti-5553–25 wt.% TiFeMo post-FAST composite: (a) DIC-TRA thermodynamic prediction with SEM-EDX line point scan, (b) BSEI micrograph, and (c) associated SEM-EDX line point scan. (d) nanohardness for both Ti-5553–25 wt.% TiFeMo post-FAST and post-aged composites, corresponding to indents shown in (b) and (e). Interdiffusion region of Ti-5553–25 wt.% TiFeMo post-aged composite: (e) BSEI micrograph, and (f) associated SEM-EDX line point scan. The black lines show the approximate location of the SEM-EDX line point scans. For all subfigures the Ti-5553 region is on the left and TiFeMo region is on the right . . . . .	118
7.7	TEM lamella of the interdiffusion region in the Ti-5553–25 wt.% TiFeMo post-aged composite: (a) STEM-HAADF (high-angle annular dark-field) overview, (b) SEM-EDX line point scan of the area adjacent to the TEM lamella at points i - vii, and (c) SADPs from regions; i - overlapping bcc $\beta$ , hcp $\alpha$ , and $\omega$ reflections, iii - bcc $\beta$ and Ti-5553/TiMo type $\omega$ reflections, and vi - bcc $\beta$ and TiFeMo $\omega$ variant reflections ( $[110]_{\text{bcc}}$ zone axis) . . . . .	119

- 7.8 STEM-EDX map of the Ti-5553 region of the TEM lamella, indicating the presence of the  $\alpha$  phase. Areas high in Ti and Al indicate the presence of  $\alpha$  phase, whereas areas high in Fe, Cr, V, and Mo indicate the presence of  $\beta$  phase . . . . 120

# List of Tables

3.1	Particle size distributions (PSD) of Ti-5553 gas atomised powder . . . . .	24
3.2	Chemical analyses of Ti-5Al-5Mo-5V-3Cr gas atomised powder . . . . .	25
3.3	$Q_{def}$ , activation energy for deformation, values for all FAST conditions: 850, 930, and 1000°C . . . . .	39
6.1	Initial and final Bate-Brooks constant values and parameters for 930 and 1000°C, with the error in % . . . . .	88
6.2	Estimated minimum and maximum temperatures ( $T$ ) and strain rates ( $\dot{\epsilon}$ ) at positions P1–P7 in the forged ‘eye bolt’ specimen, using the $\lambda$ values calculated from the mean feret minimum divided by 2.5 . . . . .	99
6.3	Estimated minimum and maximum temperatures ( $T$ ) and strain rates ( $\dot{\epsilon}$ ) at positions P1–P7 in the forged ‘eye bolt’ specimen, using the $\lambda$ values calculated from the median $\alpha$ area divided by 6.25 . . . . .	99
7.1	Chemical analysis of Ti-5Al-5Mo-5V-3Cr gas atomised powder, and TiFeMo alloy powder (wt.%) . . . . .	110
7.2	Particle size distribution (PSD) of spherical Ti-5553 powder, and angular TiFeMo powder (for both the Ti-5553–10 wt.% TiFeMo and Ti-5553–25 wt.% TiFeMo composites) ( $\mu\text{m}$ ) . . . . .	110
7.3	Mean $\beta$ grain size of Ti-5553 (30 and 60 min FAST dwell) and Ti-5553–TiFeMo composites (60 min dwell) ( $\mu\text{m}$ ) . . . . .	113



# Introduction

In order to make aircraft more attractive to airlines, aircraft manufacturers are reducing the cost of their ownership. Two key cost-saving options are to reduce the weight of the aircraft, or to improve components so they require less maintenance. For landing gear components, the main issues are corrosion of the maraging steel currently used, and its high density. Both issues can be addressed by replacing stainless steel components with metastable  $\beta$  titanium alloy components, as titanium has enhanced corrosion resistance and a higher strength-to-weight ratio, as outlined by Boyer and Briggs [1].

However, titanium alloy components are very expensive to produce compared to stainless steel components, and are even being replaced with aluminium and carbon fibre for cockpit window and door frames on the Boeing 787 to save money [2]. Therefore, for titanium alloys to be considered a viable replacement material for stainless steel components, the cost of producing them needs to be considerably reduced.

The conventional processing route for producing titanium alloy components consists of:

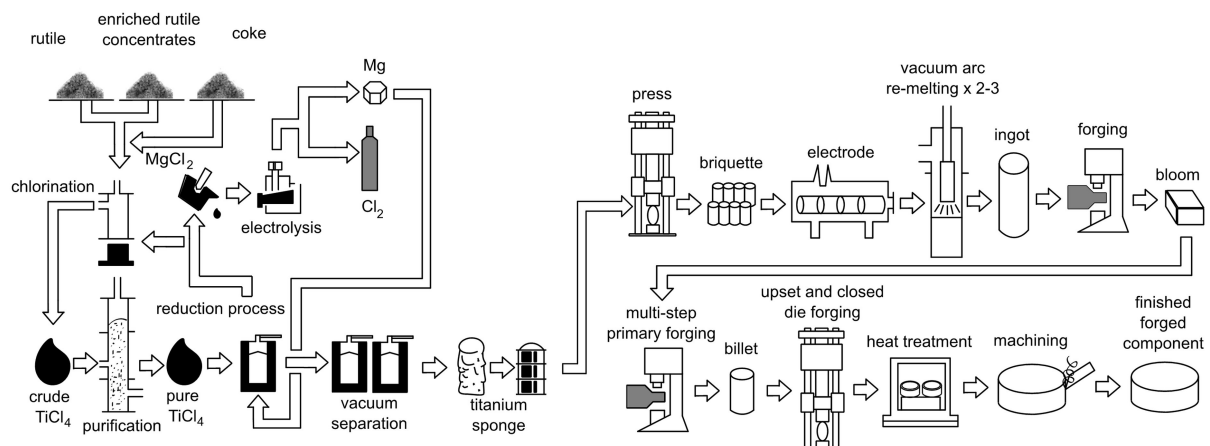


Figure 1.1: The conventional multi-step processing route for producing forged titanium alloy components. Adapted from [3]

carbochlorination extraction (Kroll process) of titanium from  $\text{TiO}_2$  which produces titanium sponge; vacuum arc re-melting (VAR) the sponge two to three times to produce an ingot; multi-step open die forging or cogging and heat treatment to breakdown the large  $\beta$  grain size and homogenise the chemistry; secondary forging of the billet, which involves conducting upset forging and closed-die forging to produce profiled shapes; and extensive machining, where, in some cases, up to 90 % of the forging is machined to swarf. The conventional processing route is summarised in Figure 1.1.

The FAST-*forge* process, as presented by Weston and Jackson [4], has been developed as a replacement for the conventional multi-step process, in order to reduce the cost of producing titanium components. This process entirely cuts out vacuum arc re-melting of the titanium sponge to produce ingot, and cuts out most of the thermomechanical processing (TMP) of the ingot which is required to achieve the desired microstructure and shape.

The FAST-*forge* process consists of consolidating titanium particulate feedstock into billet using the field-assisted sintering technology (FAST) process, forging the billet one or two times, and heat treating it to produce the desired microstructure. Such disruptive technology, coupled with lower cost alternative feedstocks, can be used to significantly lower the cost of producing titanium alloy components. A flow chart of the alternative FAST-*forge* processing route is shown in Figure 1.2, to serve as a comparison to the conventional processing route shown in Figure 1.1.

$\beta$  titanium alloys, such as Ti-5Al-5Mo-5V-3Cr (Ti-5553), are of interest due to their high strength. Many components of landing gear, where high strength is necessary, could viably be replaced by a  $\beta$  titanium alloy if the cost could be successfully reduced to compete with stainless steel, by the FAST-*forge* process.

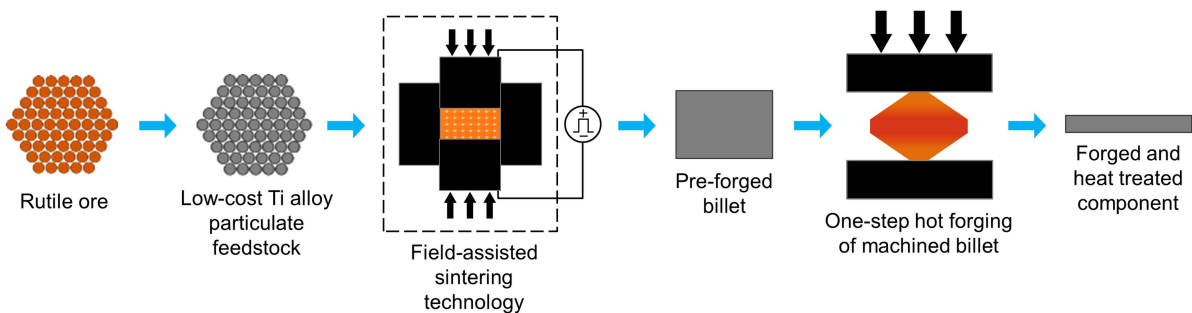


Figure 1.2: The novel FAST-*forge* processing route for low-cost titanium alloy particulate feedstock

## 1.1 Project aims and objectives

The main aim of this thesis was to investigate the ability of the FAST-*forge* process to produce a component from a metastable  $\beta$  titanium alloy, Ti-5553.

The objectives were:

- to investigate the effect of dwell temperature and dwell time on the  $\beta$  grain size and  $\alpha$  volume fraction of Ti-5553 during small-scale FAST testing
- to scale-up and produce large-scale Ti-5553 FAST components at certain temperatures, and perform compression testing and a large-scale forging study on specimens machined from them, with subsequent heat treatment
- to produce a component of complex geometry using FAST-*forge*
- to utilise the FAST-*forge* process to produce a composite of Ti-5553 reinforced with TiFeMo particles

## 1.2 Thesis outline

This thesis is split into chapters based on the stages of development of the FAST-*forge* process for Ti-5553.

Chapter 2 details the literature relevant to the work carried out in this thesis, and demonstrates where there are gaps in the current knowledge.

Chapter 3 outlines the majority of the experimental procedures used to produce the results shown in Chapters 4, 5, 6, and 7.

Chapter 4 is the initial investigative work used to produce small-scale Ti-5553 FAST specimens: the majority of the results have been previously published in a Metal Forming 2016 conference paper by Calvert et al. [5].

Chapter 5 builds on the initial work carried out in Chapter 4: FAST production was scaled up and large-scale forging was performed, as well as finite element modelling and a compression testing and heat treatment study. The majority of the results have been previously published in a Journal of Materials Processing Technology paper by Calvert et al. [6].

Chapter 6 develops a model, known as the ‘Bate-Brooks’ method, which was used to predict the microstructure from the flow stress, determined by compression testing in Chapter 5. A complex forging was produced to fulfil the aim of the project and demonstrate the FAST-*forge* process for Ti-5553 on an industrial scale. This chapter has a specific literature review

and experimental procedure on the ‘Bate-Brooks’ method and its implementation, which are supplementary to those of Chapter 2 and 3.

Chapter 7 builds on the work carried out in Chapters 4 and 5, and utilises FAST to produce composites with a Ti-5553 matrix surrounding hard TiFeMo particles. It is self-contained as the literature review and experimental procedure are more specific to composites and the TiFeMo alloy. The majority of the results have been previously published in a Scripta Materialia paper by Calvert et al. [7].

Chapter 8 gives a list of conclusions that can be drawn from this thesis, and Chapter 9 details the further work anticipated.

## Chapter 2

# Literature Review

### 2.1 Discovery of Titanium

Titanium is the fourth most abundant metal in the earth's crust and is usually found in the form of two oxide ores: ilmenite ( $\text{FeTiO}_3$ ) and rutile ( $\text{TiO}_2$ ) [8].

The titanium ore ilmenite was first discovered by British mineralogist William Gregor in 1791 in the form of black sand. In 1795 a German chemist, Martin Klaproth, analysed the ore rutile and was the first to isolate an oxide of titanium. Due to the difficulty in extracting the ore, he named the metal titanium after the Greek myth of the Titans, who were similarly imprisoned in the Earth's crust. Titanium's affinity for oxygen meant that it was impossible to commercially extract it from its ore up until the late 1930s, when the Kroll process was developed by William Kroll in Luxembourg [8,9].

Due to titanium's affinity for oxygen, the process of extracting titanium from its ores, by the Kroll process, is slow and difficult, and therefore expensive. The Kroll process involves mixing the titanium ore with chlorine gas and carbon at high temperature to produce titanium tetrachloride. The titanium tetrachloride is then mixed with either sodium or magnesium at high temperature in an inert atmosphere and reduced to give titanium sponge. This chemical reaction takes a few days to occur, and is a batch process: only a certain amount of titanium sponge can be produced at one time [10,11].

## 2.2 Titanium metallurgy

Titanium has two equilibrium phases: an  $\alpha$  phase and a  $\beta$  phase. The  $\alpha$  phase is stable at room temperature and transforms to the  $\beta$  phase upon heating at or above 882°C (in pure titanium) [12,13]. This is known as the  $\beta$  transformation temperature or the  $\beta$  transus temperature. Figure 2.1 shows the crystallographic structures of the  $\alpha$  (a) and  $\beta$  (b) phase.

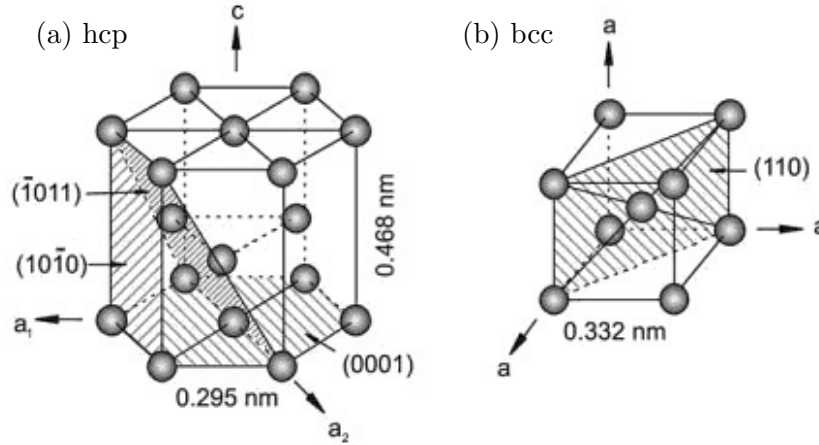


Figure 2.1: Structures of the unit cells of (a) the  $\alpha$  (hcp) and (b) the  $\beta$  (bcc) phase [9]

The  $\alpha$  phase consists of a hexagonal close packed (hcp) crystal structure, with the primary close packed plane being the basal (0001) plane, indicated in Figure 2.1a. The  $\beta$  phase consists of a body centred cubic (bcc) crystal structure: it does not contain a close packed structure. However it does contain a relatively densely packed set of planes,  $\{110\}$ , indicated in Figure 2.1b [9].

A third, non-equilibrium, phase also exists in titanium:  $\omega$  phase. It forms when the bcc  $\beta$  lattice collapses into the  $\omega$  structures shown in Figure 2.2. Partial (incommensurate) and complete (i.e. ideal) collapse results in  $\omega$  phase with the trigonal and simple hexagonal structures, respectively [13,14]. It is found in both an athermal and isothermal form, which are indicated in the  $\beta$  isomorphous phase diagram in Figure 2.4.

### 2.2.1 Slip mechanisms in titanium

Slip occurs by the dislocation glide mechanism, which allows dislocations to move along a slip plane within a crystal. Densely packed slip planes provide easier dislocation movement due to the reduced burgers vector, and therefore more slip will occur upon deformation. However, the total number of slip systems also influences the total amount of slip that can occur: more slip systems allows for more dislocation glide and therefore the material is more ductile.

As the hcp structure of the  $\alpha$  phase has only one main slip plane (the (0001) plane), within

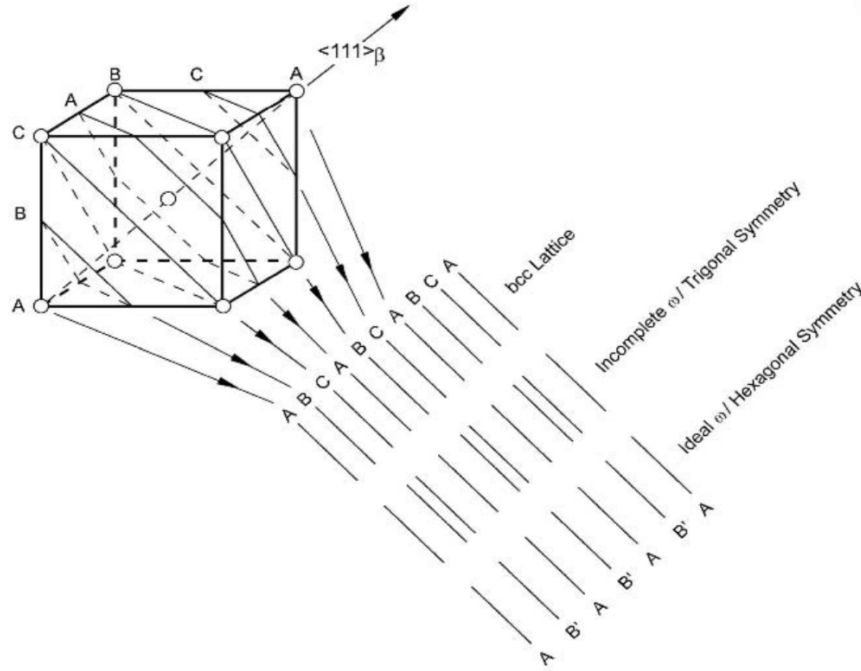


Figure 2.2: The transformation of  $\beta$  to  $\omega$  phase in the incomplete (incommensurate) and complete (ideal) forms [13]

which there are three  $\langle 11\bar{2}0 \rangle$  slip directions, it has three main slip systems in total. The bcc structure in the  $\beta$  phase has six  $\{110\}$  slip planes, each with two  $\langle 111 \rangle$  slip directions, so there are twelve slip systems in total [9]. Plastic deformation is therefore more favourable in the  $\beta$  phase than in the  $\alpha$  phase for titanium.

### 2.2.2 Diffusion in titanium

Diffusion occurs more easily in the  $\beta$  phase than the  $\alpha$  phase, as the  $(0001)$  close packed plane in the  $\alpha$  phase impedes diffusing elements. Diffusion rates are therefore much slower in the  $\alpha$  phase, with self-diffusion of titanium in the  $\alpha$  phase being  $\sim 3$  orders of magnitude slower than self-diffusion in the  $\beta$  phase. This is important as it influences any thermomechanical processing and solution heat treatment and ageing performed [13].

Any processing which produces only the  $\beta$  phase will therefore be subject to increased diffusion. Grain growth in the  $\beta$  phase at high temperatures will be influenced by the driving force for the minimisation of energy at the grain boundaries. As the grains increase in size, the grain boundary curvature will decrease which reduces the surface energy. The number of grains also decreases as certain grains preferentially grow, so the grain boundary area will decrease which also reduces the surface energy [15].

### 2.2.3 Titanium alloy classification

Titanium alloys in general have high strength, low density and excellent corrosion resistance due to the stable  $\text{TiO}_2$  layer formed upon oxidation. They are also compatible with carbon fibre as they have similar thermal expansion coefficients; and as carbon and titanium are both cathodic they therefore do not set up a galvanic cell upon contact (which reduces the risk of galvanic corrosion) [1, 8].

Titanium alloys are separated into three main groups, based on which phase is thermodynamically stable at room temperature:  $\alpha$  alloys,  $\alpha + \beta$  alloys, and  $\beta$  alloys. Different alloying elements have different effects on the stability of each of the phases and the phase diagram.

$\alpha$ -stabilising elements such as oxygen, aluminium, nitrogen, and carbon can be added to pure titanium to increase the  $\beta$  transus temperature, thereby stabilising the  $\alpha$  phase to higher temperatures [9].

$\beta$ -stabilising elements such as vanadium, molybdenum, niobium, iron, silicon, copper, chromium, and manganese can be added to reduce the  $\beta$  transus, thereby stabilising the  $\beta$  phase to lower temperatures [9].

Neutral alloying elements such as tin and zirconium can also be added, which have no effect on the  $\beta$  transus temperature. Figure 2.3 shows the effect of each alloying element addition on the phase compositions and temperatures at which they exist in phase diagrams.

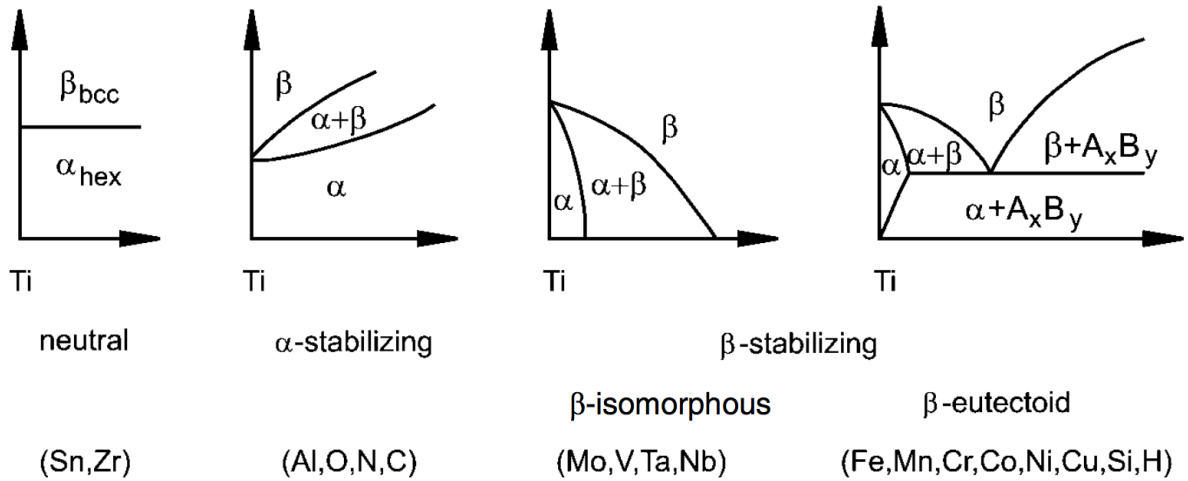


Figure 2.3: Effect of alloying element additions on the  $\alpha$  and  $\beta$  phases and the  $\beta$  transus temperature [9]

#### 2.2.3.1 $\alpha$ alloys

$\alpha$  alloys include commercially pure (CP) titanium, and alloys with mostly neutral or  $\alpha$ -stabilising element additions. Any  $\beta$ -stabilising element additions present are limited to a small volume



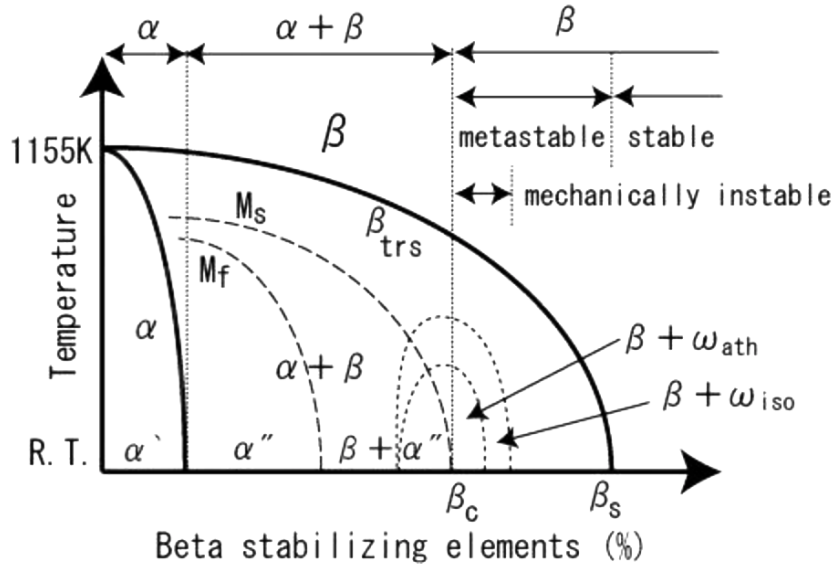


Figure 2.4:  $\beta$  isomorphous phase diagram indicating the three main classifications of titanium alloys [17]

fraction (typically a few vol%) [16].

Examples of  $\alpha$  alloys include the CP grades 1–4, which have small additions of Fe and O, and Ti-5Al-2.5Sn and Ti-3Al-2.5V, which have small additions of Al, Sn, and V [16].

CP grades are generally used for applications where excellent corrosion resistance, weldability, and fabricability are desired over strength, such as the chemical and petrochemical industries, where they are preferred to stainless steel due to their increased durability [9, 16].

Ti-5Al-2.5Sn and Ti-3Al-2.5V are used for higher strength applications than the CP grades, such as in cryogenic tanks where weldability and ductility at low temperatures are desired, and for hydraulic tubing and large pressure vessels where high strength and fabricability with good corrosion resistance are required, respectively [16].

### 2.2.3.2 $\alpha + \beta$ alloys

The three main classifications of titanium alloys are illustrated in Figure 2.4, which also shows the effect of the percentage of  $\beta$ -stabilising elements on the  $\beta$  transus temperature and on the formation of the various phases.

$\alpha + \beta$  alloys are defined as those that exist between the  $\alpha/\alpha + \beta$  phase boundary and the point at which the martensitic start temperature is equivalent to room temperature, as indicated in Figure 2.4 [13]. Both the  $\alpha$  and  $\beta$  phases are stable at room temperature, and the volume fraction of  $\beta$  phase present is determined by the amount of  $\beta$ -stabilising elements and the processing conditions.

A near- $\alpha$  alloy is an  $\alpha + \beta$  alloy which consists of mostly the  $\alpha$  phase at room tempera-

ture. Small amounts of  $\beta$ -stabilising elements ( $<10$  vol%) are added to extend the  $\beta$  transus temperature and produce higher strength and better fatigue resistance than  $\alpha$  alloys, while retaining the creep resistance of the  $\alpha$  phase. They are generally used for aerospace gas turbine applications, such as blades and disks in the high pressure compressor section; with operating temperatures of  $400\text{--}600^\circ\text{C}$  which is above the capability of other  $\alpha + \beta$  alloys with more  $\beta$ -stabilising elements [9, 13, 18].

Ti-6Al-2Sn-4Zr-2Mo-(0.1Si) (Ti-6242(S)) and Ti-5.8Al-4Sn-3.5Zr-0.7Nb-0.5Mo-0.35Si-0.06C (Ti-834) are examples of near- $\alpha$  alloys utilised at high temperature, where creep resistance and fatigue resistance are also required. They contain only small amounts of the  $\beta$ -stabilising elements Mo and Nb in order to produce higher strength microstructures which are more resistant to fatigue, while minimising diffusion which is much faster in the  $\beta$  phase (and therefore aids creep). Al, Sn, and Zr are known to improve the creep resistance in the  $\alpha$  phase, and addition of Si improves the creep resistance further and improves the fatigue strength and temperature capability [9, 18, 19].

Alloys containing larger amounts of  $\beta$ -stabilising elements are the common  $\alpha + \beta$  alloys, which occupy the large area shown in the phase diagram in Figure 2.4, and possess a combination of excellent mechanical properties and good producibility. The wide processing window, Figure 2.4, is the region in which the transformation of  $\alpha$  to  $\beta$  phase occurs slowly (before 100 %  $\beta$  phase is reached at the  $\beta$  transus), and is the reason for the superior producibility. It allows similar microstructures and properties to be produced with different processing temperatures; therefore they can be produced more easily [9]. A wide variety of microstructures, and thus mechanical properties, can be produced in the  $\alpha + \beta$  alloys by using different thermomechanical processing routes [19].

The most widely used  $\alpha + \beta$  alloy, Ti-6Al-4V (Ti-64), was developed in the 1950s and contains one  $\alpha$ -stabilising element, Al, and one  $\beta$ -stabilising element, V [9]. It has an optimal balance of: a high tensile strength-to-weight ratio; good ductility, fatigue resistance, and fracture toughness; and resistance to corrosion. These properties are maintained up to temperatures of  $\sim 300^\circ\text{C}$ , so Ti-64 is used extensively in low-temperature regions of aerospace gas turbine engines, including fan blades and disks, and low pressure compressor blades and disks. However, it is also used in structural parts of aircraft, where it is preferred to aluminium, and in the biomedical, automotive, power generation, marine, and chemical industries, as well as for sporting and jewellery [8, 19, 20].

### 2.2.3.3 $\beta$ titanium alloys

$\beta$  titanium alloys are known for their good fatigue properties, and are therefore favoured for fatigue critical applications such as landing gear [21]. They can be processed at lower temperatures and produce higher yield strengths than  $\alpha + \beta$  alloys, and have very good corrosion resistance [22].

Another common feature of  $\beta$  alloys is a reduced  $\beta$  transus temperature compared with  $\alpha + \beta$  alloys, which allows for reduced deformation temperatures and lower flow stresses during thermomechanical processing, and therefore a reduction in the die forces required for deformation [23]. Diffusion is much faster in the  $\beta$  phase than the  $\alpha$  phase, and consequently processes of diffusional deformation, recovery, and recrystallisation occur at lower temperatures and higher strain rates in  $\beta$  alloys than in  $\alpha + \beta$  alloys [24].

There are two main classes of  $\beta$  titanium alloy: the high strength (metastable) and heavily stabilised alloys. Metastable  $\beta$  alloys, e.g. Ti-10V-2Fe-3Al and Ti-5Al-5Mo-5V-3Cr, exist within the equilibrium  $\alpha + \beta$  region of the phase diagram and can therefore contain  $\alpha$  phase at room temperature. However, there is no martensitic transformation upon quenching to room temperature, Figure 2.4, and it is possible to retain 100 % metastable  $\beta$  upon cooling from the  $\beta$  phase field [23]. Their high strength is attributable to fine  $\alpha$  laths that precipitate out during ageing, and provides them with higher yield strengths than  $\alpha + \beta$  alloys. Heavily stabilised  $\beta$  alloys, e.g. Ti-15-3 and Beta C, are further to the right of the phase diagram as they contain more  $\beta$  stabilising elements than the metastable  $\beta$  alloys, such that only the  $\beta$  phase is thermodynamically stable at room temperature. Their lower volume fraction of  $\alpha$  phase results in a lower strength than metastable  $\beta$  alloys [22].

The main  $\beta$  alloys currently used were developed between the 1970s and the 1990s, when there was a gap in the market for good forging alloys (Ti-10V-2Fe-3Al and Ti-5Al-5Mo-5V-3Cr), strip alloys (Ti-15333), and alloys for springs and fasteners (Beta C). Along with Beta21S and Alloy C, these  $\beta$  alloys cover the heat treatable Mo range of 10 to 16 %, which offers a stable  $\beta$  alloy and fills the potential market for  $\beta$  alloys.

Developing a new  $\beta$  alloy is expensive due to: the inclusion of high-cost elements such as Mo, V, and Cr in high concentration in most  $\beta$  alloys; the high formulation costs when compared to alloys such as Ti-64; and increased time to promote homogeneity in the melt, when compared to alloys such as Ti-64. The new alloy would also take years to develop and validate, especially for application in the aerospace industry where standards on reliability are very strict. These issues are especially compounded by the fact that there is currently no express need to produce a new alloy, as the range of uses for  $\beta$  alloys has already been addressed in the established

alloys. If a new alloy can be produced at a reduced cost, as is suggested in this thesis, this could be enough to allow  $\beta$  alloys to break into other areas of interest where they are currently seen as too expensive. Some of the current issues with  $\beta$  alloys are: the propensity for ingot segregation during melting; the lack of robust chemistries; and narrow processing windows [23].

It is hoped that the FAST-*forge* processing route will be able to address these issues with  $\beta$  alloys. As melting is avoided, the material should have a more homogenous chemistry, and minimal forging will be required which will make a narrow processing window less significant.

#### 2.2.3.4 *Ti-5Al-5Mo-5V-3Cr*

The metastable  $\beta$  titanium alloy, Ti-5Al-5Mo-5V-3Cr (Ti-5553), was investigated in this thesis due to its use for landing gear applications. It is used because of its optimum mix of ductility, fracture toughness, fatigue strength, and yield strength [22].

Ti-5553 was introduced in the late 1990s by VSMPO as a variation of the alloy VT-22 (Ti-5Al-5V-5Mo-1Cr-1Fe), and was commercialised for major die forging applications on the Boeing 787 Dreamliner in the 2000s. The chemistry of VT-22 was altered slightly, by increasing the Cr content and decreasing the Fe content, to produce Ti-5553 which has a more uniform macrostructure and microstructure, and improved hardenability [23]. It succeeded Ti-10V-2Fe-3Al (Ti-1023) as the major  $\beta$  alloy used in landing gear applications, and offers improved strength and toughness, with an ultimate tensile strength of between 1163 and 1332 MPa [25].

However it has many other advantages over Ti-1023, including: its improved processability, as Ti-5553 has a shallower  $\beta$  transus approach curve which allows for a wider processing window for thermomechanical processing and heat treatment; it displays a lower microstructural temperature sensitivity, which is especially advantageous in large cross-section forgings where the temperature throughout the workpiece is hard to control [23,26]; and it has low quench sensitivity so there is no microstructural difference between the air cooled and the water quenched conditions (when cooled from the solution heat treatment temperature), which results in more homogeneous microstructures at the surface and centre of large cross-section forgings [25,26].

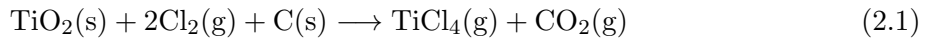
These advantages of Ti-5553 are due to the addition of Mo, which Ti-1023 does not contain. Mo diffuses slowly, thereby delaying the onset of precipitation and inhibiting coarsening so that  $\alpha$  dissolution is slow [26].

These advantages are also the reason Ti-1023 has been replaced by Ti-5553 in many landing gear components, as they ensure easier processing and improved reproducibility as Ti-5553 is less microstructurally sensitive to the processing parameters (strain, strain rate, and temperature) [26].

## 2.3 Conventional processing of titanium

Due to titanium's affinity for oxygen, the process of extracting titanium from its ores by the Kroll process is slow and difficult, and therefore expensive, despite its abundance. An overview of the conventional processing route for titanium is shown in Figure 1.1.

The Kroll process begins with the reaction of titanium ore with chlorine gas and carbon at high temperature ( $>1000^{\circ}\text{C}$ ) to produce titanium tetrachloride,  $\text{TiCl}_4$ , as shown in Equation 2.1. The titanium tetrachloride is then purified to greater than 99.9 %, before reduction with either sodium or magnesium at high temperature ( $>1000^{\circ}\text{C}$ ) in an argon atmosphere forms porous titanium sponge (Equation 2.2). This chemical reaction takes a few days to occur, so only a fixed amount (batch) can be produced at one time [11].



After the titanium sponge is formed, it is broken into very small pieces and blended with the required alloy additions, before being pressed into a compact. Multiple compacts are plasma welded together to produce electrodes, which are used as feedstock for the vacuum arc remelting (VAR) process [27]. During this process, which is performed two or three times to ensure homogeneity of chemistry and structure, the electrode is melted in a vacuum by an electric arc and then cooled in the water-cooled crucible to form a solidified ingot [11, 28].

This part of the processing of titanium is also very expensive due to the need for titanium to be melted multiple times in a vacuum (to prevent oxidation), and due to the large amounts of electricity used during this process. The final ingot is then thermomechanically processed, in order to produce the desired microstructure and properties in the final component. Multi-step open die forging (cogging) and heat treatment is used to breakdown the large  $\beta$  grain size and homogenise the chemistry; with secondary forging of the billet, involving upset forging and closed-die forging, used to produce profiled shapes; followed by extensive machining, where, in some cases, up to 90 % of the forging is machined to swarf.

A breakdown of the estimated cost of producing a 2.5 cm thick titanium plate by the conventional processing route is given in Figure 2.5, in order to illustrate the main areas of expense in titanium production. As shown, the current processing route involves expensive steps: such as titanium extraction from rutile ore (the Kroll process - chlorination and reduction); vacuum arc

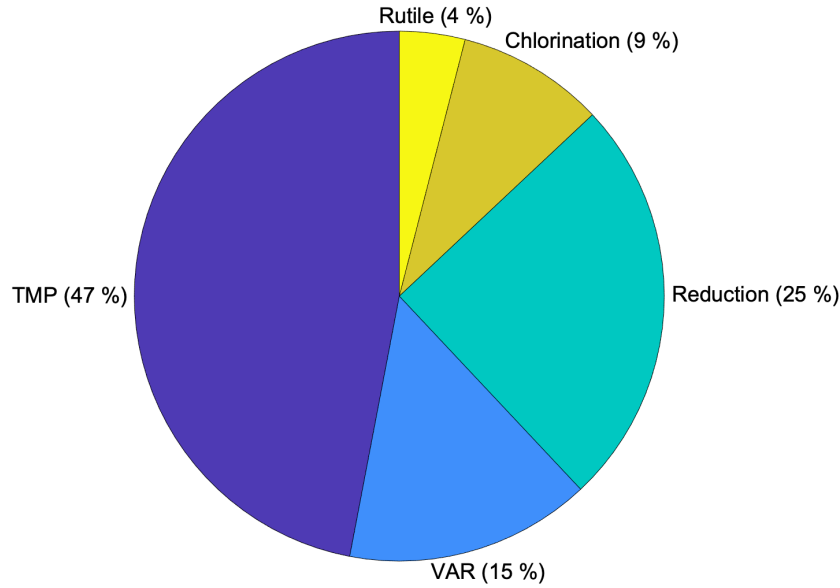


Figure 2.5: A breakdown of the estimated cost of producing a 2.5 cm (1 inch) thick titanium plate by the conventional processing route [29]

re-melting (VAR) to produce homogeneous titanium alloys; and thermomechanical processing (TMP) to produce optimal microstructure and mechanical properties.

### 2.3.1 Thermomechanical processing of $\beta$ titanium alloys

Overall in  $\beta$  alloys, the thermomechanical processing needs to be tailored to produce a microstructure with the necessary mechanical properties. The  $\beta$  grain size, primary and secondary  $\alpha$  morphology, size, and volume fraction, and prevention of detrimental grain boundary  $\alpha$  all need to be considered [21].

There are three main types of microstructure produced by different thermomechanical processing routes:  $\beta$  annealed,  $\beta$  processed, and bi-modal.

The  $\beta$  annealed condition is predominantly used for heavily stabilised  $\beta$  alloys, and involves deformation in the  $\alpha + \beta$  or  $\beta$  phase fields, subsequent recrystallisation in the  $\beta$  phase field, and ageing in the  $\alpha + \beta$  phase field. This produces relatively equiaxed  $\beta$  grains, with continuous  $\alpha$  at the grain boundaries and  $\alpha$  laths within the grain forming upon ageing, Figure 2.6. This microstructure provides good strength and fracture toughness due to the predominance of fine secondary  $\alpha$  laths which have mixed orientations [22]. This condition is generally not used for metastable  $\beta$  alloys as the grain boundary  $\alpha$  reduces the ductility, due to the strain being localised in the less ductile  $\alpha$  phase (at the grain boundary), which leads to crack nucleation and fracture at the grain boundaries [21].

The  $\beta$  processed condition involves deformation in the  $\beta$  phase field to highly deform the  $\beta$  grain boundaries, cooling to allow coarse  $\alpha$  plates to grow within the grains, and subsequent

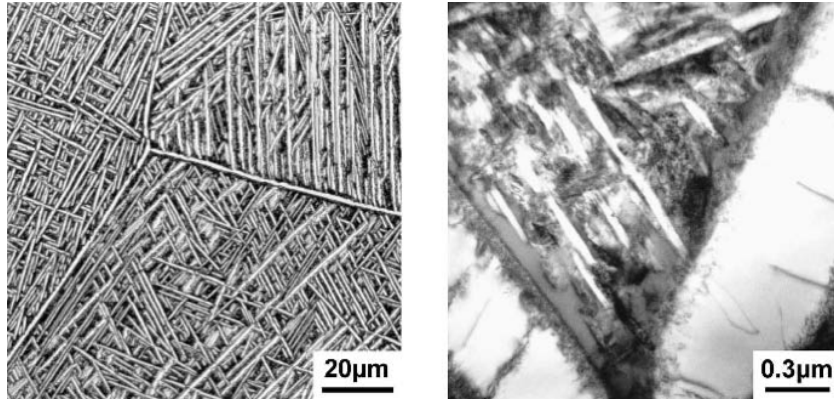


Figure 2.6: An example of a  $\beta$  annealed microstructure,  $\beta$ -CEZ [22]

annealing and ageing within the  $\alpha + \beta$  phase field to allow fine  $\alpha$  laths to form within the coarser  $\alpha$  plates, Figure 2.7. The deformation of the  $\beta$  grains without recrystallisation produces broken up grain boundary  $\alpha$  ('necklacing') which improves the fracture toughness [22]. Detrimental grain boundary  $\alpha$  formed during deformation in the  $\beta$  phase field can be avoided by rapidly cooling from the  $\beta$  phase field. If this cannot be achieved, for example in large forging cross sections, subsequent forging in the  $\alpha + \beta$  phase field can break up the grain boundary  $\alpha$  [21].

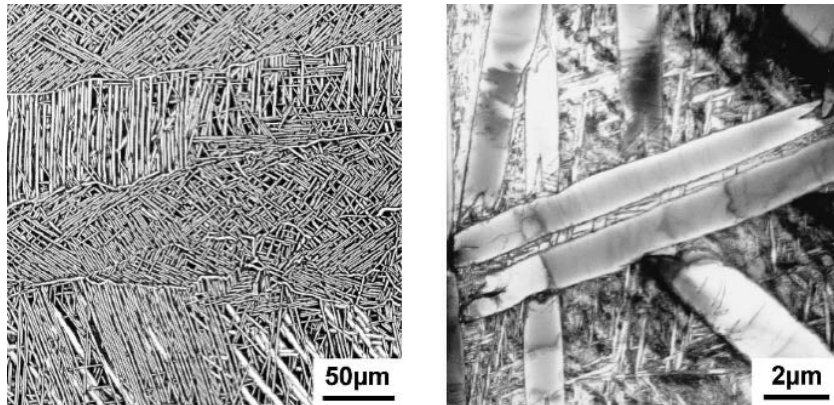


Figure 2.7: An example of a  $\beta$  processed microstructure, Ti-6246 [22]

The bi-modal condition involves deformation in the  $\alpha + \beta$  phase field to break up the  $\alpha$  at  $\beta$  grain boundaries. This broken up  $\alpha$  forms globular primary  $\alpha$  grains upon annealing in the  $\alpha + \beta$  phase field, and subsequent ageing allows fine acicular  $\alpha$  laths to precipitate between the primary  $\alpha$  grains, Figure 2.8. This microstructure provides a good balance between strength, ductility, fracture toughness, and fatigue resistance [22]. The preferred microstructure for aerospace  $\beta$  alloy applications has controlled amounts of elongated primary  $\alpha$  in an aged  $\beta$  matrix with extremely fine secondary  $\alpha$  laths, due to this optimal mix of mechanical properties [30].

To produce a bi-modal microstructure, the most important factor is the transformed  $\beta$  matrix, as a high cooling rate ( $>10^\circ\text{C}/\text{min}$ ) from the annealing temperature and a lower ageing

temperature results in high yield strength irrespective of the volume fraction of globular  $\alpha$ . This is due to thinner  $\alpha$  laths forming in the transformed  $\beta$  region upon fast cooling and a lower ageing temperature ( $\sim 500^\circ\text{C}$ ) favouring secondary  $\alpha$  lath formation, both of which increase strength [31].

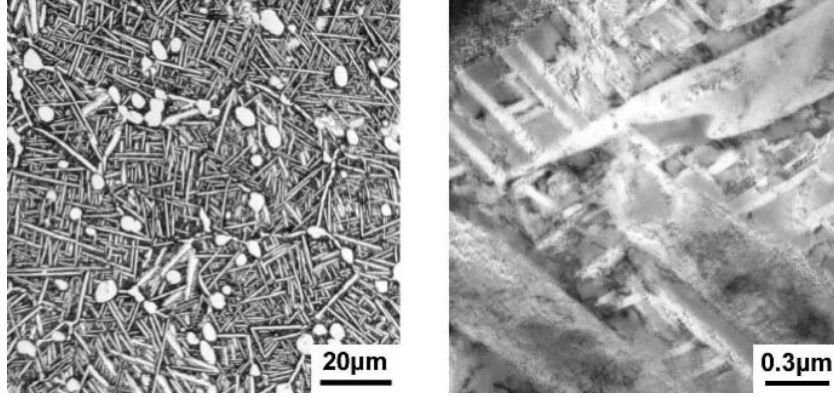


Figure 2.8: An example of a bi-modal microstructure,  $\beta$ -CEZ [22]

### 2.3.2 Thermomechanical processing of Ti-5553

The  $\beta$  transus temperature of Ti-5553 is usually between  $845\text{--}850^\circ\text{C}$ , although it depends on the exact chemistry of the material [26, 31, 33].

In general, Ti-5553 is forged in the  $\beta$  phase field to break up the large  $\beta$  grains in the ingot structure, and subsequently forged in the  $\alpha + \beta$  phase field to break-up the  $\alpha$  phase [78].

During forging, dislocations form in the  $\beta$  phase matrix surrounding the  $\alpha$  particles, due to local strain incompatibility (if the  $\alpha$  phase particles are much harder than the  $\beta$  matrix) [81]. This has been shown to occur in  $\beta$  titanium alloys, as the much higher hardness of the  $\alpha$  phase in titanium compared to the  $\beta$  phase leads to reduced deformation, and therefore to strain concentration build-up in the  $\beta$  phase surrounding the  $\alpha$  particles [76]. This causes high misorientation sub-grains to form in the  $\beta$  matrix phase surrounding the  $\alpha$  particles.

However, for higher strains or for  $\alpha$  phase particles with a higher aspect ratio (acicular  $\alpha$ ), strain build-up leads to sub-boundary formation in the  $\alpha$  phase because of increased dislocation pile-up at the  $\alpha/\beta$  interfaces [76, 78]. The  $\beta$  phase penetrates along the  $\alpha/\alpha$  sub-boundaries, breaking up the acicular  $\alpha$  into more equiaxed grains, which is known as globularisation [82].

As a result, a high peak flow stress is reached initially at low strain during deformation, followed by a reduction in flow stress with increasing strain, due to the break-up and globularisation of the  $\alpha$  particles (as they no longer impede dislocations). This is known as flow softening and results in the characteristic flow softening curve shapes shown in Figures 2.9 and 2.10 for Ti-5553 [26, 37, 78].



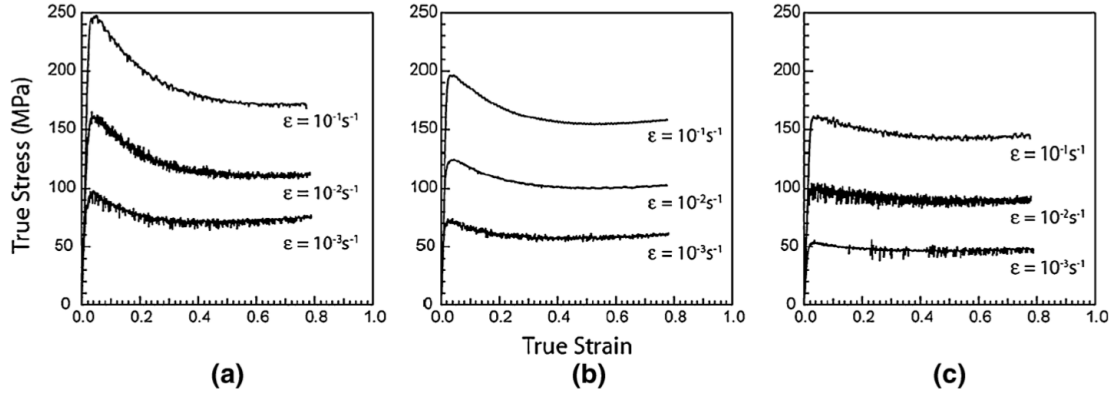


Figure 2.9: Flow curves for Ti-5553 in the  $\beta$  forged condition, forged at strain rates of 0.001, 0.01, and 0.1  $\text{s}^{-1}$  and temperatures of (a) 785°C, (b) 810°C, and (c) 835°C [37]

Sub-grain boundaries are made up of dislocations: during deformation, free dislocations are produced by increased strain and are annihilated by their interaction with dislocations of the opposite sign in the sub-grain boundary (through cross-slip and climb). This process of dynamic recovery limits the accumulation of dislocations, so that the flow stress remains at a constant value despite an increase in strain (known as the steady state stress) [83]. The flow behaviour is controlled by the predominant  $\beta$  phase at this steady state stress, which is shown in Figures 2.9 and 2.10 for strains of  $\sim 0.4$  [78].

Following forging, the usual heat treatment regime for Ti-5553 is either solution heat treatment and ageing (STA) or  $\beta$  annealing, slow cooling, and ageing (BASCA). STA involves heat treating the material at 20–60°C below the  $\beta$  transus for 1 h and subsequently air cooling, then ageing at 550–650°C for a minimum of 8 h. This heat treatment produces a microstructure with 10 to 20 vol% globular primary  $\alpha$  in a matrix of fine secondary  $\alpha$  laths, which provides high strength and good fatigue behaviour. BASCA involves solution treating the material at 20–60°C above the  $\beta$  transus for a minimum of 1 h, cooling at a controlled rate to 650–800°C

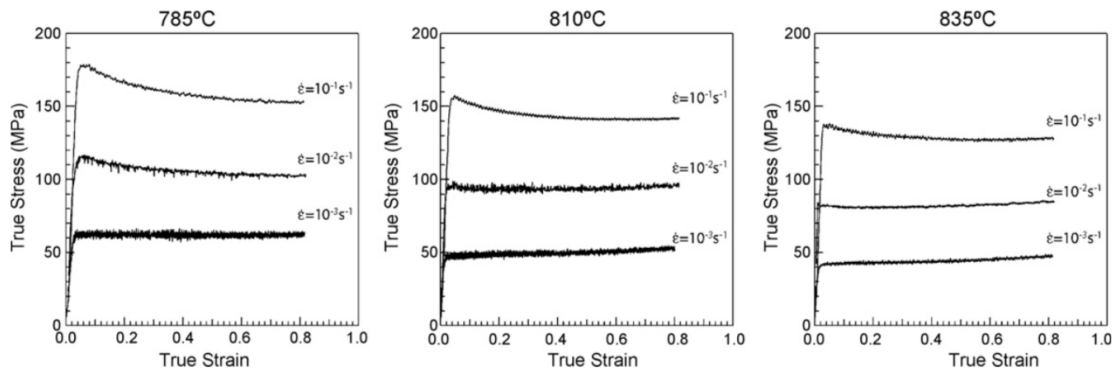


Figure 2.10: Flow curves for Ti-5553 in the  $\alpha + \beta$  condition, forged at strain rates of 0.001, 0.01, and 0.1  $\text{s}^{-1}$  and temperatures of 785°C, 810°C, and 835°C [26]

and holding at temperature for a minimum of 1 h, before air cooling to room temperature. This heat treatment produces a microstructure with a high volume fraction of lamellar  $\alpha$ , which results from the controlled cooling from the  $\beta$  phase, and provides double the fracture toughness of STA material along with intermediate strength [1, 23].

Producing a microstructure with very fine  $\alpha$  laths greatly increases the strength by creating a large number of  $\alpha/\beta$  phase boundaries that act as barriers to dislocations [35]. However, a microstructure with solely fine  $\alpha$  laths has reduced ductility; therefore the inclusion of larger primary  $\alpha$  grains is imperative to provide ductility without greatly reducing the strength. This is the reason that the bi-modal microstructure is preferred over the lamellar  $\alpha$  microstructure for landing gear applications [22, 36].

#### *2.3.2.1 Effect of $\omega$ phase on thermomechanical processing of Ti-5553*

$\omega$  phase is predominantly found in  $\beta$  alloys, including Ti-5553. The athermal  $\omega$  phase can form upon quenching from solution heat treatment in the  $\beta$  phase field. Isothermal  $\omega$  phase can be produced at certain ageing temperatures, depending on the solute content of the alloy, and the process requires diffusion (as opposed to athermal  $\omega$ ) [32, 33].

In heavily stabilised  $\beta$  alloys,  $\omega$  has a trigonal symmetry, whereas in metastable  $\beta$  alloys it has a hexagonal symmetry, Figure 2.2 [13]. They are both variations on the bcc  $\beta$  crystal structure, which is the reason why  $\omega$  is more prevalent in  $\beta$  titanium alloys [32].

$\omega$  has been found to have a detrimental effect on the fracture toughness and leads to embrittlement in  $\beta$  alloys [34]. However, it is theorised that the metastable ( $\omega + \beta$ ) phases transform to ( $\alpha + \beta$ ) phases during ageing and this facilitates very fine  $\alpha$  phase precipitation in a highly homogeneously distributed arrangement, which leads to an improvement in mechanical properties [32, 33, 35].

Athermal  $\omega$  phase has been observed in  $\beta$  solution heat treated and quenched Ti-5553. In Ti-5553 specimens subsequently aged at 350°C for 2 h,  $\omega$  phase was found to coexist with  $\alpha$  phase which had nucleated near  $\beta/\omega$  boundaries [33].

## 2.4 Novel processing route - FAST-*forge* process

As described in Chapter 1, the novel processing route consists of using FAST to consolidate powder, then forging and heat treating the consolidated material to the final microstructure, Figure 1.2. This FAST-*forge* process has been investigated in this thesis, and would be considered a low-cost titanium manufacturing route if low-cost powder, such as that produced by the Metalysis (FFC) process, were to be used as the feedstock.

### 2.4.1 Field-assisted sintering technology (FAST)

Field-assisted sintering technology (FAST), also known as spark plasma sintering (SPS) or pulsed electric current sintering (PECS), was developed in the 1960s and first commercially applied in the 1990s [38].

FAST is a rapid sintering technique which applies a uniaxial force and a pulsed direct current (DC) through a punch-die-powder assembly to consolidate the powder, as shown in Figure 2.11. The graphite punches and die evenly distribute the current around the powder, and allow for homogeneous heating. FAST is performed under low atmospheric pressure or in an inert gas atmosphere to ensure elemental pick-up from air is prevented. Cooling from the sintering temperature is provided by the water-cooled vacuum chamber [39–41].

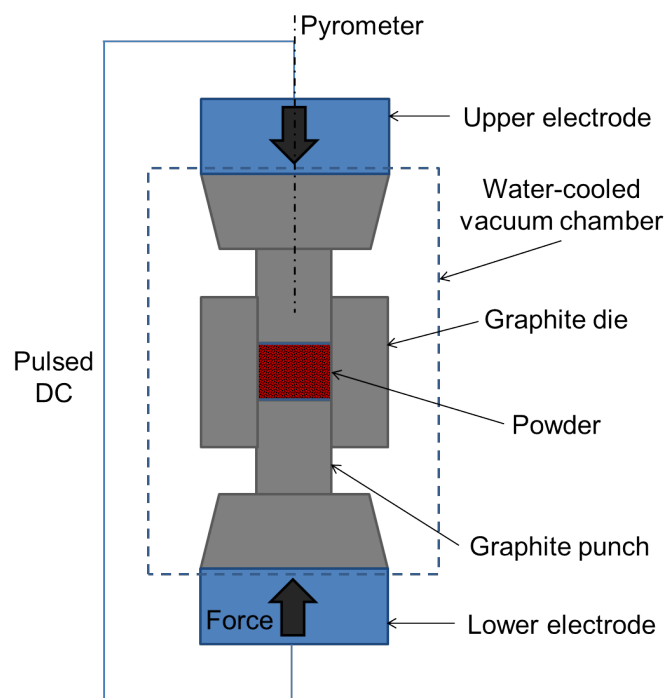


Figure 2.11: Experimental set-up of the FAST process

### 2.4.1.1 Mechanism of FAST process

The mechanism behind the FAST process is widely disputed; some authors attribute it to so-called ‘spark plasma’ and ‘electrical discharge’ between powder particles [42]. Other authors claim no plasma or ‘electrical discharge’ is generated, but cannot offer an alternative explanation for the formation of necks between the powder particles [43,44]. Therefore, an overview of the ‘spark plasma’ and ‘electric discharge’ theories will be given here for evaluation.

It is theorised that during FAST the pulsed DC creates an electric spark discharge, of high energy and low voltage, which momentarily generates spark plasma at very high localised temperatures, from several to tens of thousands of degrees, and high pressures between the powder particle surfaces [39–41].

Oxides and other surface contaminants are said to be vapourised from the particle surfaces, which cleans them [38,39]. Immediately behind the area of vapourisation the particle surface melts and the liquidised areas are drawn together to create necks between the particles [38,40,41]. Plastic deformation of the powder due to uniaxial applied force assists neck formation and aids consolidation [38]. A diagram demonstrating the mechanism behind the FAST process is shown in Figure 2.12.

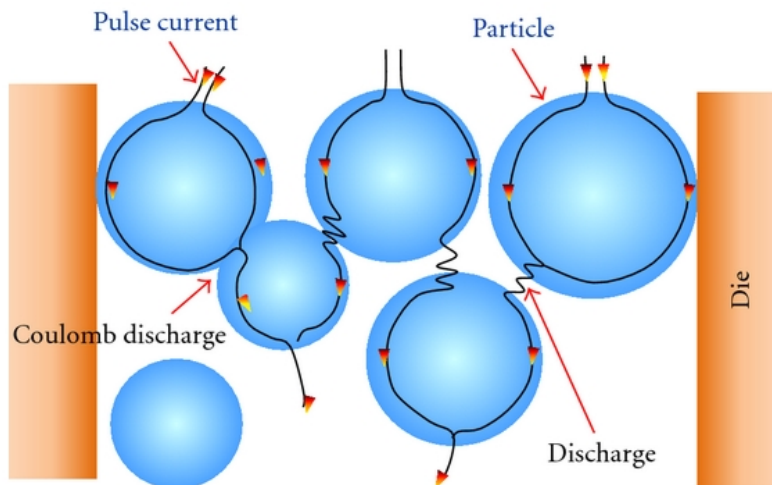


Figure 2.12: Theorised mechanism of the FAST process, where coulomb discharge is equivalent to joule heating [45]

What can be said for certain is that some mechanism, be it ‘spark plasma’ and ‘electrical discharge’ or otherwise, operates to create necks between individual powder particles. This then allows the electric current to pass between particles and internally heat the powder by joule heating, which is the heating effect generated due to electrical resistance in a material when a current is passed through it [38–40,43]. Ongoing applied pressure and joule heating allows

plastic deformation of the powder particles and leads to consolidation of the powder [38].

#### *2.4.1.2 Advantages of FAST*

There are multiple advantages of the FAST process over other powder consolidation methods, such as hot isostatic pressing (HIP) and conventional sintering.

The first of these is that the process is very rapid, taking only 5–20 min for the whole process, compared to HIP which can take hours [39, 41, 46]. Part of the reason the process is so fast is that very high heating rates can be generated ( $>300^{\circ}\text{C}/\text{min}$ ) [39, 40]. These high heating rates can be generated due to direct heating of the die-mould-powder assembly, which allows the powder to be heated internally as well as externally. Processes such as HIP only heat externally, where the powder is heated slowly by radiation and convection in a furnace [39]. The electric field used in FAST is also said to affect the heating rates as it accelerates diffusion, and thereby produces rapid heating rates, due to high speed migration of ions [39].

Another advantage of the direct internal heating of the FAST process is that the centre and the surface of the powder receive the same amount of current, and therefore the same amount of heating, which ensures that a specimen with high homogeneity is produced [38]. This has the added benefit that very little internal stress is generated within the specimen, as the heating is simultaneously consistent at the centre and the surface of the powder [38]. The higher heating rates and faster processing also allows lower dwell temperatures, 200–500°C lower than in conventional sintering, to be used to consolidate powder [41].

FAST has the ability to produce material to a controlled density, by adjusting the force applied and the sintering temperature, and to produce material with full density if required [38, 46]. Due to oxides and contaminants being vapourised from the particle surfaces during sintering, leaving pure molten powder material behind, the bonding produced between particles is very strong and free from impurities, even for material produced at a controlled density [38].

Particle growth of the starting powder material is limited, as the heating is concentrated at the points of contact between powder particle surfaces during FAST, and the high heating rates promote diffusion mechanisms rather than grain growth-promoting diffusion mechanisms (e.g. surface diffusion) [39, 41, 43]. Therefore, grain growth is limited during the process, and nanostructured powder materials can be sintered with minimal change in the original grain size, which is generally not possible in conventional sintering [39, 40, 46].

The advantage of FAST over conventional sintering is that cold pressing before sintering is not necessary, as the powder is contained within the mould during the process [40]. For this reason, binders which are used in conventional sintering to hold the powder together are not

necessary, and therefore the expensive binder removal process is also unnecessary [38].

FAST is an efficient process compared to the alternatives as it has the ability to: produce near-net shapes direct from powder to finished part in one-step; produce parts quickly and with minimal grain growth; produce homogeneous microstructure due to homogeneous heating; and produce parts with high density [38, 46]. These advantages over other powder consolidation methods are the reason FAST is being investigated as a viable method for powder consolidation in this novel low cost titanium processing route.

#### *2.4.1.3 Uses of FAST*

FAST is mainly used for ceramic applications, especially for ceramics that have high melting points and for hard-to-sinter materials, which can be rapidly sintered to full density [39, 43, 47, 48]. This includes hard cutting tool materials such as TiN, and zirconia which is hard to sinter by conventional sintering methods [39].

Although FAST is mainly used for ceramics, there are a number of other applications for which the process is advantageous. It has been used to produce materials for armour, biomedical, magnetic, electric (dielectric, electroceramics and ferroelectrics), functionally graded materials (FGMs), nanostructures, porous materials, superconductors, shape memory alloys, ceramics (machinable, superplastic and hard), laminates, composites, catalysts, and intermetallics [43, 47].

It is used for biomedical applications as decomposition of chemicals such as hydroxyapatite (HA) or other biomaterials can be avoided, due to the short processing time [39].

FAST is used for magnetic materials as it has been shown to improve magnetic properties and permittivity in ferroelectrics [43].

FAST is favoured for FGMs and multilayer intermetallics as the process allows for adjustment of temperature gradients during densification and the current aids reactivity and diffusion, which enables fabrication of functionally graded or layered material structures with differing properties [40, 44].

Nanostructured, intermetallic, and composite materials can be simultaneously synthesised and densified, resulting in retained grain size and high density which would not be possible by conventional sintering [48].

Although there are fewer examples of metallic materials being used in FAST, there are some papers which have focussed on the advantages of using FAST to produce these materials. One such paper used FAST to produce porous stainless steel which had higher compressive strength than that of HIP-produced material [48]. Other papers focus on the use of this process to

produce titanium, and are detailed in the following section.

#### *2.4.1.4 Titanium produced by FAST*

The use of FAST for titanium and titanium alloy powders has primarily been restricted to biomaterials applications. Some studies focused on producing porous titanium or Ti-64 for use as an implant material, and demonstrated that the porosity can be controlled by FAST [42, 49, 50]. Others focused on: ultra-fine grained (UFG) cp-Ti, which had better biocompatibility than coarse-grained titanium [51]; titanium composites, TiSi and TiC, which improved the strength, hardness, and wear resistance of commercially pure titanium by using ultra-fine grained powder and high strength Ti/Si dispersoids [52, 53]; Ti/HA FGM [54]; titanium-based bulk metallic glasses [55]; TiC/Ti and TiC/Ti-15Mo cermets for joints [56]; TiAl powders [57]; as-sintered Ti-64 from nanostructured powder [58]; commercially pure titanium [42, 59]; nano-structured commercially pure titanium [60]; and titanium-titanium di-boride composites for armour applications [61].

However, there are only a few studies in which forging of a titanium alloy produced by FAST has been investigated. These include those conducted by Vicente Jr et al. [62] and Menapace et al. [63], which have shown that compression testing of Ti-64 produced by FAST produces microstructure and flow stress curves similar to that of conventionally produced Ti-64, and that of Weston and Jackson [4] which has found the same results for upset forging of shaped Ti-64 cones produced by FAST (via the FAST-*forg*e process).

A  $\beta$  titanium alloy has only been produced by FAST by Weston et al. [64]. It was found that the hold temperature and pressure were the most significant FAST process parameters to produce full density in Ti-5553. High temperatures and high pressures were found to produce very high densities, and it was recommended that titanium alloy powders should be heated above their  $\beta$  transus temperature to take full advantage of the improved diffusion rates in the  $\beta$  phase. The heating rate was found to have minimal effect on the density, and was found to slightly increase the grain size. However, it was recommended that as high a heating rate as possible should be used to take full advantage of the speed of the process. The dwell time was also found to have minimal effect on the density, although an increase in dwell time was found to slightly increase the  $\beta$  grain size.

## Chapter 3

# Experimental Procedure

This chapter contains experimental procedures which are common across all chapters. Experimental procedures specific to a chapter are included at the start of that chapter, where necessary.

### 3.1 Powder production

Ti-5553 powder was produced by gas atomising small pieces of a landing gear forging, provided by Safran Landing Systems. Gas atomisation was performed by TLS Technik Spezialpulver, and the particle size distributions (PSD) and chemical analyses of the gas atomised (GA) powder are shown in Tables 3.1 and 3.2. Chemical analysis was performed using inductively coupled plasma optical emission spectrometry (ICP-OES) and PSD was measured using a Malvern Mastersizer 3000 laser particle size analyser using the dry dispersion method.

Two batches of powder were produced this way: the first, Batch 1, was solely used for the small-scale FAST testing (Chapter 4); and the second, Batch 2, was used for all large-scale FAST testing and for the Ti-5553–TiFeMo composite work (Chapters 5, 6, and 7). Oxygen and nitrogen levels were determined by inert gas fusion infrared and thermal conductivity detection, for Batch 2 only.

Table 3.1: Particle size distributions (PSD) of Ti-5553 gas atomised powder

PSD [ $\mu\text{m}$ ]	Batch 1	Batch 2
Dx10	23	24
Dx50	69	60
Dx90	142	95

Light microscopy was performed on each of the batches of GA powder (as described in



Table 3.2: Chemical analyses of Ti-5Al-5Mo-5V-3Cr gas atomised powder

Element [wt%]	Batch 1	Batch 2
Al	4.85	5.09
Cr	2.72	2.71
Fe	0.38	0.40
Mo	5.18	5.12
Ni	0.11	0.01
V	5.24	5.24
Other	1.33	0.27
Ti	80.19	80.87
O		0.29
N		0.02

Section 3.5.3) to determine the particle morphology, level of internal porosity, and the microstructure prior to FAST, as shown in Figure 3.1 for each powder batch.

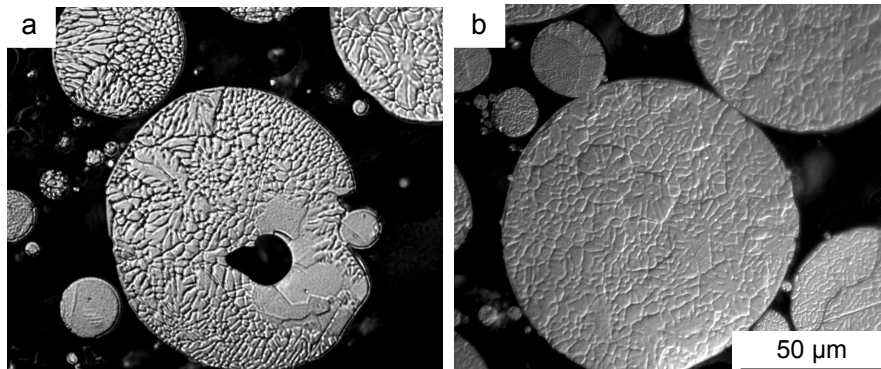


Figure 3.1: Light micrographs of (a) Batch 1 and (b) Batch 2 of gas atomised Ti-5553 powder

### 3.2 Field-assisted sintering technology

Field-assisted sintering technology (FAST) was performed at both the small- and large-scale using similar methodologies.

Small-scale FAST testing was performed using an FCT Systeme GmbH Spark Plasma Sintering furnace type HP D 25 at The University of Sheffield.

Large-scale FAST testing was performed using an FCT Systeme GmbH Spark Plasma Sintering furnace type H-HP D 250 at Kennametal Manufacturing UK Ltd, Figure 3.2a.

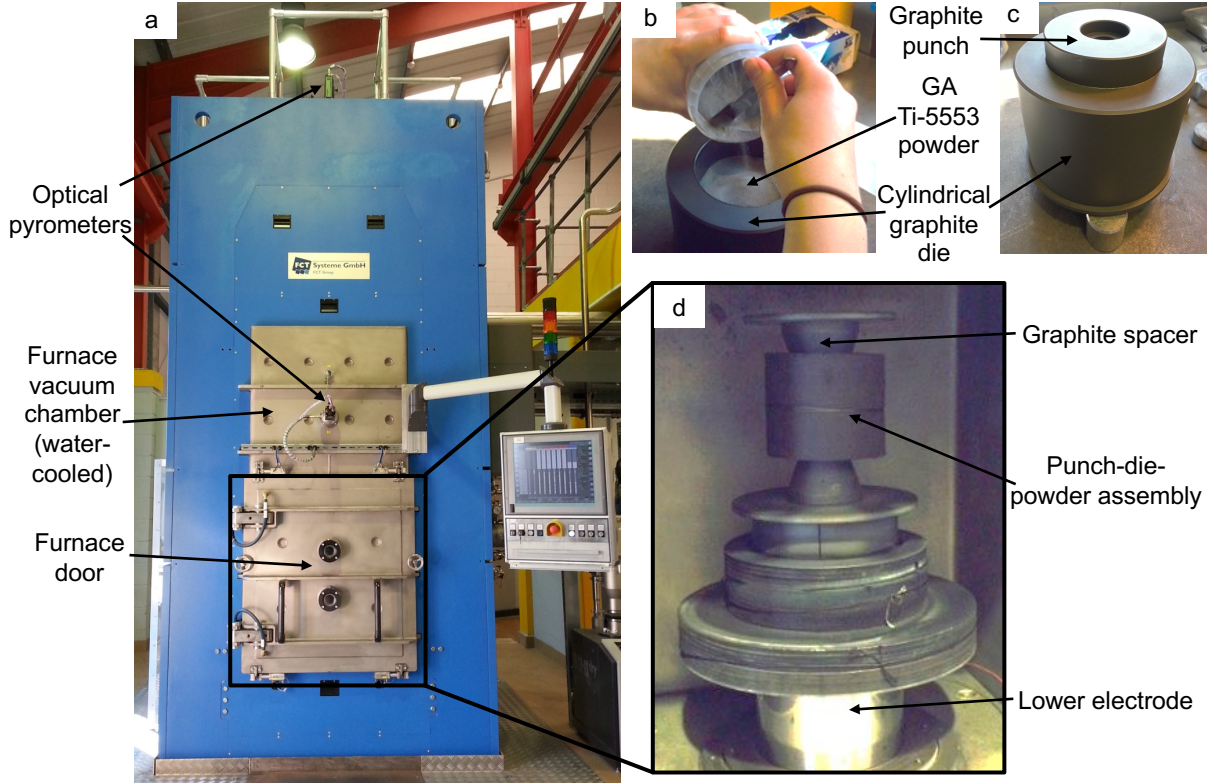


Figure 3.2: Annotated photographs of: (a) the FAST machine at Kennametal Manufacturing UK Ltd which was used to produce large-scale FAST specimens; (b) gas atomised Ti-5553 powder being poured into the cylindrical graphite die; (c) the punch-die-powder assembly ready to be placed into the FAST machine; and (d) a punch-die-powder assembly being raised into the furnace

The mass of powder,  $m$ , required to produce each specimen was calculated using Equation 3.1, where  $V$  is the volume,  $r$  is the radius,  $h$  is the height, and  $\rho$  is the density, which was assumed to be  $4.65 \text{ g/cm}^3$  [65]. All small-scale specimens were produced with a diameter of 20 mm, and all large-scale specimens were produced with a diameter of 100 mm.

$$m = \rho V = \rho \pi r^2 h \quad (3.1)$$

The powder was placed into a cylindrical graphite die and between two graphite punches to make up a punch-die-powder assembly. Graphite foil lined the inside of the die, and between the punches and the powder to aid with removal of the sintered specimen, and to protect the die and punches from mechanical damage. Sacrificial graphite wear pads, which reduce wear on the punches, and carbon fibre composite (CFC) discs, which control thermal expansion and increase resistance to provide additional heating, were placed between the powder and the punches for only the large-scale FAST testing.

Examples of an assembly being prepared for processing are shown for the large-scale testing, Figure 3.2b and c.

The assembly was cold pressed before FAST to ensure that the powder particles were tightly packed. Once prepared, the assembly was surrounded by a CFC ring and rayon weave for the large-scale testing and a graphite felt sleeve for the small-scale testing; in order to reduce heat loss during FAST.

The assembly was placed between copper electrodes, which allowed a direct current to flow through the assembly, thereby consolidating the powder. The mobile electrode/s hydraulically maintain a constant pressure during FAST to aid consolidation. In the case of large-scale testing, the assembly was raised into the furnace vacuum chamber, as shown in Figure 3.2d, to make contact with the upper hydraulic electrode.

The FAST cycle was programmed prior to testing and certain parameters such as dwell temperature, time at dwell temperature (dwell time), heating rate, and force were specified.

The temperature of the specimens was controlled using an optical pyrometer which measured from the top of the furnace, and additionally from the front for large-scale testing. Temperature profiles are shown in Figure 3.3 for above 450°C as the pyrometer cannot record below that temperature. Initial pressures of 16 MPa (5 kN) and 6 MPa (50 kN) were applied to ensure contact between the assembly and the electrodes during FAST, for all small- and large-scale testing respectively. Pressure during testing was increased to 35 MPa (11 kN) and 50 MPa (395 kN), respectively, to aid consolidation. The heating rate was 200°C/min for all small-scale testing, but due to the risk of thermal shock in the graphite die this was reduced to 100°C/min for all large-scale testing.

At the start of the FAST cycle, the chamber was evacuated using a vacuum pump to approximately  $2 \times 10^{-3}$  bar and, for small-scale testing only, was subsequently purged with argon (to avoid oxidation during FAST). Pulsed direct current (DC) was then applied through the electrodes to begin heating, with a repeating pattern of 15 ms on and 5 ms off.

The pressure was steadily increased along with the temperature to the dwell values input,

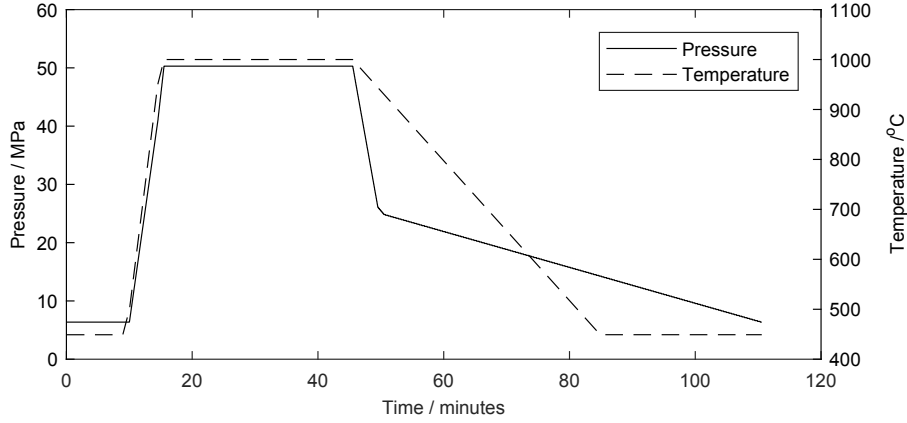


Figure 3.3: Typical pressure and temperature profiles for large-scale FAST testing

and held for the input dwell time, before the current was removed and the specimens were cooled by the water-cooled vacuum chamber at approximately  $250^{\circ}\text{C}/\text{min}$  and  $14^{\circ}\text{C}/\text{min}$ , for small- and large-scale testing respectively.

Following cooling, the consolidated specimens were removed from the die by a press and grit-blasted to remove the graphite foil.

### 3.2.1 Small-scale FAST specimens

Small-scale FAST specimens were produced using 14.7 g of powder, with heights of approximately 10 mm and diameter 20 mm, at temperatures of 800, 850, 900, 930, 970, 1000, and  $1200^{\circ}\text{C}$  for dwell times of 3, 10, 30, and 60 min.

### 3.2.2 Large-scale FAST specimens

Large-scale FAST specimens were produced using 1100 g of powder, with heights of approximately 30 mm and diameter 100 mm, at temperatures of 850, 930, and  $1000^{\circ}\text{C}$  for a dwell time of 30 min. Two specimens were produced at  $1000^{\circ}\text{C}$ ; one for subsequent compression testing and one for the subsequent large-scale forging study (Chapter 5).

### 3.3 Compression testing

Compression testing was performed using a Servotest ThermoMechanical Compression (TMC) machine at The University of Sheffield to simulate upset forging, Figure 3.4d.

For all tests, the specimens were held in the robot gripper arms, transferred through the Fast Thermal Treatment Unit (FTTU), and placed between the axisymmetric compression tools to be forged, Figure 3.4c. All tests were true strain rate controlled, with a constant true strain rate maintained throughout testing.

Uniaxial compression specimens (cylinders) and small double truncated cones were compressed, with dimensions as shown in Figure 3.4a and b. Two sizes of cylinders were used for testing, both with a height to diameter ratio of 1.5:1 (15 mm height with 10 mm diameter, and 9 mm height with 6 mm diameter). Double truncated cones were used to provide a large variation of strain within a single specimen, although this results in a different strain rate and strain path throughout the specimen. The dimensions of the double truncated cones were based on previous work [66].

Measurements were taken for the initial heights and widths, and final heights and widths of all specimens using a micrometer. Four heights and widths were measured for each specimen to produce average height and width values.

Specimens were coated with boron nitride release agent to prevent adhesion between the specimen and the compression tools. Load, displacement, and temperature data was produced for each test and converted to true stress and true strain as described in Section 3.5.11.

#### 3.3.1 High temperature compression testing

The large-scale FAST specimens produced at 850, 930, and 1000°C were each machined to produce 12 uniaxial cylindrical specimens and 4 double truncated cone specimens for high temperature compression testing.

1.1 mm thermocouple holes were drilled into the mid-height of the specimens to fit a 1 mm diameter N-type thermocouple to measure the instantaneous temperature. The specimens were induction heated at 4°C/s to the compression temperature using a Fast Thermal Treatment Unit (FTTU), and held for 20 s and 30 s (for cylinders and double truncated cones, respectively) to enable thermal equilibrium within the specimen. They were then transferred into the furnace, which was held at the compression temperature, to be compressed.

Cooling was performed using a water jet, which quenched the specimens and preserved the compressed microstructure. A test matrix of 785, 810, and 835°C at 0.01, 0.1, 1, and 5 s<sup>-1</sup> was

performed for cylinders, while the double truncated cones were all compressed at  $785^{\circ}\text{C}$  and  $0.1\text{ s}^{-1}$ . Cylindrical and double truncated cone specimens were compressed to a final strain of  $\sim 0.6$  and  $1.2$ , respectively.

All post-compressed microstructures were observed under SEM after sectioning the compressed specimen in half, as described in Sections 3.5.2 and 3.5.4.

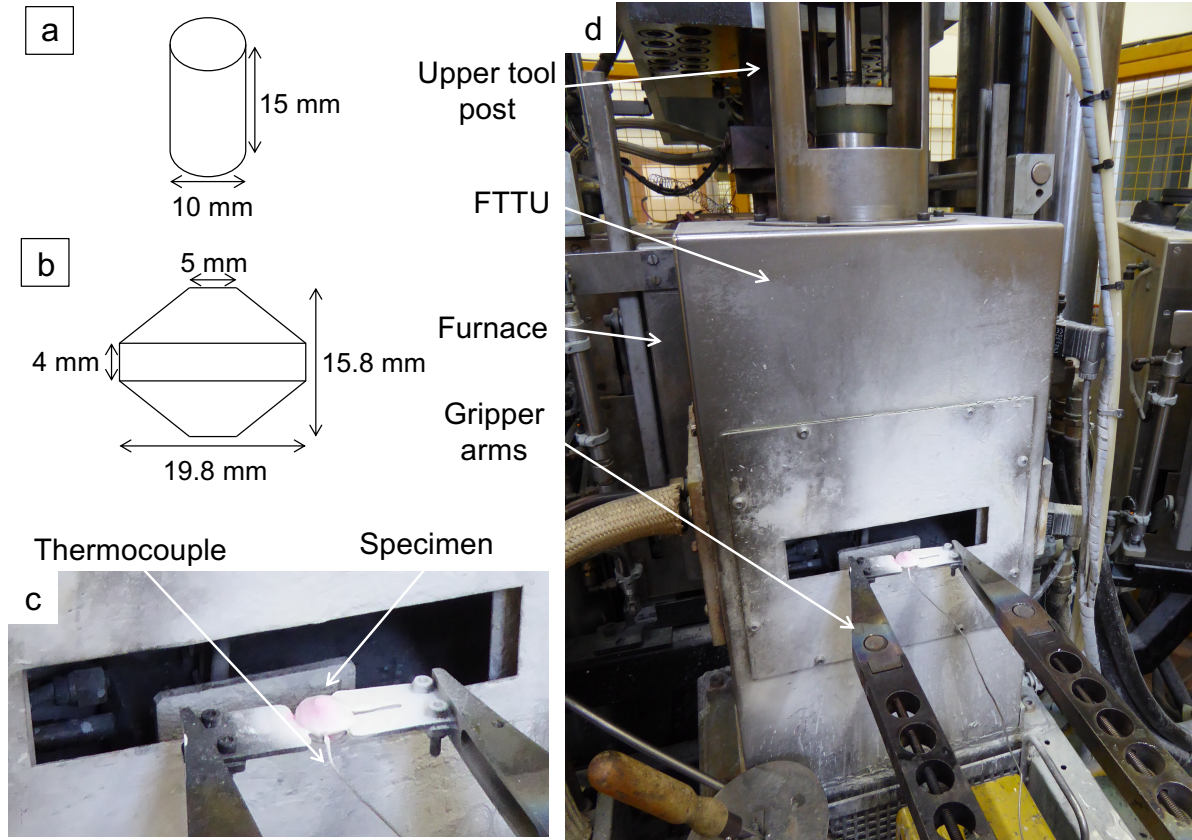


Figure 3.4: Thermomechanical compression testing: (a) dimensions of cylindrical specimens, (b) dimensions of double truncated cone specimens, (d) annotated photograph of the thermomechanical compression machine, with (c) close-up of a specimen in the gripper arms

### 3.4 Solution heat treatment and ageing

Solution heat treatment and ageing were performed in an Elite tube furnace under vacuum. All solution heat treated specimens were held at 785°C for 2 h. The heating rate was approximately 26°C/min and the specimens were allowed to furnace cool to room temperature at a rate of approximately 4°C/min.

Ageing was performed using a programme which heated at 4°C/min to the ageing temperature, held for the number of hours specified, then furnace cooled to room temperature at a rate of approximately 4°C/min. Temperatures of 400–600°C and times of 2–8 h were used.

## 3.5 Analysis techniques

### 3.5.1 $\beta$ transus temperature determination

The  $\beta$  transus temperature was determined by heat treating post-FAST cubes of approximately  $1 \times 1 \times 1.4$  cm. An Elite box furnace was used to heat the cubes at temperatures between 785 and 890°C for 60 min, with a K-type thermocouple used to measure temperature. Specimens were immediately water quenched to preserve the high temperature microstructure.

Imaging software ImageJ [67] was used to measure the volume fraction of primary  $\alpha$ , as described in Section 3.5.8. SEM images produced at high magnification were used, as the microscopic  $\alpha$  particles were too small to be observed under light microscopy.

Figure 3.5 shows the  $\beta$  approach curve, from which a  $\beta$  transus temperature of between 880 and 900°C can be approximated ( $\sim 890^\circ\text{C}$ ). The transus temperature is generally between 845–850°C for Ti-5553 [26, 31, 33], so this value is  $\sim 40^\circ\text{C}$  higher than is typical. This may be due to the oxygen content, 0.29 wt% (Table 3.2), which is quite high when compared to Ti-5553 from a similar source (0.135 wt%) [26]. As oxygen is an  $\alpha$ -stabilising element, an increased oxygen content will increase the temperature at which the  $\alpha$  phase transforms to the  $\beta$  phase, i.e. the  $\beta$  transus temperature [9].

The powder used was that of Batch 2, described in Table 3.1 and 3.2, so the  $\beta$  approach curve and  $\beta$  transus temperature will be slightly different for the Batch 1 powder due to differing chemistries.

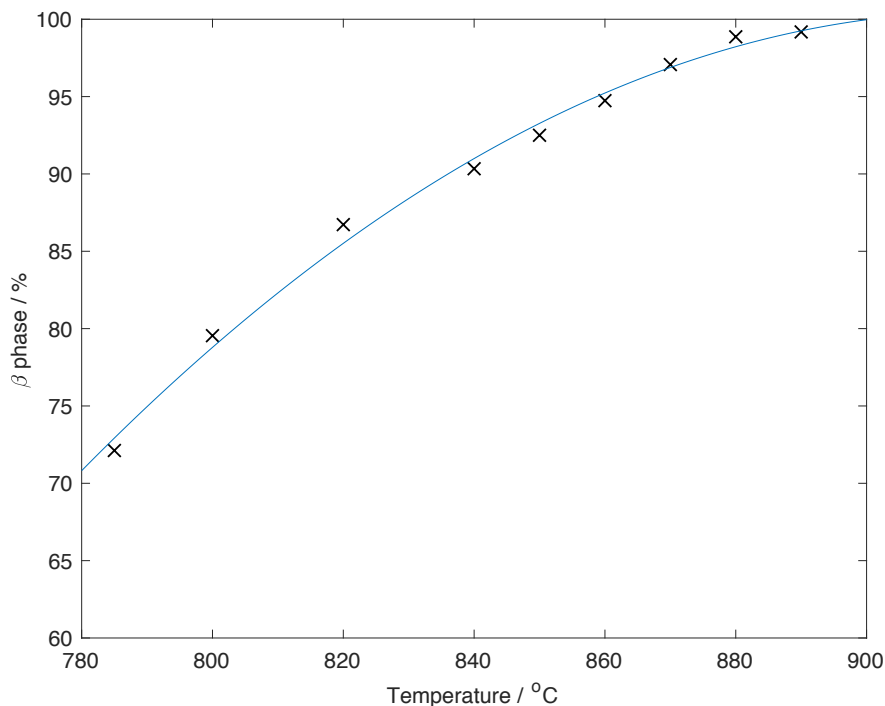
### 3.5.2 Sample preparation

All specimens were sectioned using a Buehler AbrasiMet 250 abrasive cutter with a 1 mm thick disc, a Struers Minitom with a 0.5 mm thick disc, or a Buehler Isomet with a 0.8 mm disc. Unless stated otherwise, all specimens were sectioned in half perpendicular to the FAST, compression, or forging direction.

Specimens were then hot mounted in Bakelite or conductive Bakelite in a Buehler SimpliMet mounting press, in order for the surface to be ground and polished ready for light or scanning electron microscopy (SEM).

Powder specimens were cold mounted in epoxy resin, and ground and polished as with specimens hot mounted in Bakelite. Grinding was performed using water-lubricated abrasive silicon carbide papers with successively smaller abrasive particles (P800 - P2500) on an EcoMet 250 Pro automatic grinding and polishing machine, followed by a grinding disc with 9  $\mu\text{m}$  diamond suspension. A force of 27 N was used, as well as 150 rpm platen speed, 40 rpm head



Figure 3.5:  $\beta$  transus temperature approach curve

speed, and complementary rotation of the head and platen.

Polishing was performed using a mixture consisting of 0.06  $\mu\text{m}$  colloidal silica, water, and hydrogen peroxide (30 % in water) on a soft polishing cloth in the ratio of 8:1:1. This produced a mirror finish for microscopy, and the hydrogen peroxide provided some chemical etching in order to reveal the microstructure. The polished specimen surfaces were examined using either light or scanning electron microscopy.

### 3.5.3 Light microscopy

All light microscopy was performed using a Nikon Eclipse LV150 light microscope, under polarised light.

### 3.5.4 Scanning electron microscopy

All scanning electron microscopy (SEM) was performed using an FEI Inspect F or F50 scanning electron microscope in the backscatter electron imaging (BSEI) mode, using 10 kV accelerating voltage and working distance of  $\sim 10$  mm.

### 3.5.5 Transmission electron microscopy

Transmission electron microscopy (TEM) was used to examine fine microstructural features beyond the ability of SEM.

To prepare TEM lamellas from specimens, an FEI Quanta 200 3D with focussed ion beam (FIB) was used to mill out a 25  $\mu\text{m}$  length of material from the specimen surface. The TEM lamella was extracted using an Omniprobe, attached to a copper TEM grid, and then thinned to thickness  $\sim 100$  nm.

TEM was performed on a Philips EM420 transmission electron microscope in the bright field mode.

### 3.5.6 Microhardness testing

Microhardness testing was performed using a Struers Durascan-70 G5 with a Vickers indenter and 4.905 N load (held for 15 s). All hardness testing was performed on flat polished specimen surfaces to reduce error in the measurements. A 95 % confidence interval was used to determine the error from the mean, Equation 3.2.

The layout and number of the indents used depended on the shape and size of the specimens once mounted in Bakelite and ground and polished, although it was ensured that the indents were far enough apart that they did not affect each other.

#### 3.5.6.1 *Post-FAST specimens*

Three rows with 20 indents each were placed horizontally along the length of each FAST specimen to get an average value for the entire specimen. Indents were 0.75 mm apart horizontally along the length of the specimen and 4 mm apart vertically along the FAST direction.

#### 3.5.6.2 *Post-compressed, solution heat treated, and aged cone specimens*

Three rows with 10 indents each were placed horizontally along the length of the specimen to get an average value for the entire specimen. Indents were 1 mm apart horizontally along the length of the specimen and 1.5 mm apart vertically along the compression direction.

#### 3.5.6.3 *Forged and heat treated specimens*

Three rows with 50 indents each were placed horizontally along the length of the specimen, from centre to edge, to get an average value for each distance from the centre. Indents were 0.58 mm apart horizontally along the length of the specimen (from centre to edge) and 0.2 mm apart vertically along the forging direction.

### 3.5.7 Density measurements

Dark field light microscopy was used to calculate the level of porosity in the post-FAST specimens.

Buehler Omnimet and ImageJ image analysis software [67, 68] were used to differentiate between white (porosity) and black (solid material) areas in a dark field light micrograph, and calculated the area fraction of white compared to black.

This porosity percentage was measured three times for each image and the mean porosity percentage was calculated. The mean density percentage was calculated by subtracting the mean porosity percentage from 100. The error was measured as described in Section 3.5.9.

### 3.5.8 $\alpha$ volume fraction measurements

ImageJ image analysis software [67] was used to measure the primary  $\alpha$  volume fraction of the FAST specimens produced around and below the  $\beta$  transus in Chapter 4, and the volume fraction for the  $\beta$  transus determination specimens, from BSEI SEM micrographs.

The software was used to automatically detect and measure the area fraction of  $\alpha$ , as defined in ASTM E1245. A ‘threshold color’ was set on the image, and was manually adjusted so that the lighter  $\beta$  phase was highlighted and the darker  $\alpha$  phase was not. The ‘measure’ function was used to analyse the area fraction automatically. Two SEM images were taken for each specimen, and for each image three measurements were taken and the mean value calculated. The mean values for the two images were averaged to give a mean value for the specimen as a whole. The percentage error was calculated as in Equation 3.5.

It should be noted that these measurements are technically area fractions, rather than volume fractions, so there will be additional error caused by any directionality within the microstructure.

### 3.5.9 Error

The error in the density measurements is given by the relative accuracy % ( $RA\%$ ), which is calculated using the 95 % confidence interval (95 % *c.i.*). All other error measurements are given by the 95 % *c.i.*, unless otherwise stated.

The 95 % *c.i.* is calculated as shown in Equation 3.2, where  $s$  is the standard deviation,  $n$  is the number of measurements, and  $t$  is the value of Student’s  $t$  distribution (for  $p = 0.025$  and  $n - 1$  degrees of freedom).  $RA\%$  is calculated as shown in Equation 3.3, where  $\bar{x}$  is the mean value.

$$95 \% c.i. = \frac{s}{\sqrt{n}} \times t \quad (3.2)$$

$$RA \% = \frac{95 \% c.i.}{\bar{x}} \times 100 \quad (3.3)$$

### 3.5.10 $\beta$ grain size measurements

The linear intercept method was used to approximate the  $\beta$  grain size for the specimens produced by FAST. Horizontal lines were superimposed onto low magnification BSEI SEM images using ImageJ image analysis software [67]. It was ensured that the lines were roughly equidistant and did not intercept the same grain twice; the number of lines per image varied between 5 and 9.

Points were placed where the lines intercepted grain boundaries and were counted for each line. The length of each line, in  $\mu\text{m}$ , was divided by the number of interception points along it to give the average grain size for that line,  $x_i$ .

The mean of the average grain sizes,  $\bar{x}$ , was then calculated to give the approximate grain size for the specimen, as shown in Equation 3.4 (where  $n$  is the number of horizontal lines on the image).

According to ASTM E112-13, which illustrates the standard test methods for determining average grain size, a 95 % confidence interval should be calculated to determine the relative accuracy of the mean grain size value. However, the spread of the average grain size data from the mean is too large for this relative accuracy to be valid. This spread is most likely due to the natural variation in grain size within each image and specimen (as illustrated in Figure 4.2).

An alternative method was therefore used to work out the error. Firstly the absolute values of the average grain size value,  $x_i$ , subtracted from the mean value,  $\bar{x}$ , were calculated. The maximum of these absolute values for each image was divided by the mean value and multiplied by 100 to give the percentage error, as shown in Equation 3.5.

Although the percentage errors for each specimen were quite large, the main objective of grain size measurement was to determine qualitatively how the grain size varied when the dwell temperature and the dwell time varied, rather than to produce precise quantitative data.

$$\bar{x} = \frac{\sum x_i}{n} \quad (3.4)$$

$$\text{Percentage error} = \left( \frac{|\bar{x} - x_i|}{\bar{x}} \right) \times 100 \quad (3.5)$$

### 3.5.11 Flow stress analysis

Load, displacement and temperature data were extracted from the TMC machine to calculate the true flow stress and true strain values for each test. Initial and final heights and widths were measured for each compressed specimen. The stiffness of the machine, compliance, was already corrected for in the data.

For high temperature compression testing, thermal expansion caused the dimensions of the specimens to increase slightly. To account for this expansion, the ‘hot’ heights were calculated for the initial and final dimensions using Equation 3.6, where  $\alpha$ ,  $8.4 \times 10^{-6}$  [69], is the thermal expansion coefficient,  $h_{hot}$  is the hot height,  $h_{cold}$  is the height measured at room temperature,  $T_{test}$  is the average test temperature in K, and  $T_{room}$  is room temperature in K.

$$h_{hot} = h_{cold} + (\alpha h_{cold}(T_{test} - T_{room})) \quad (3.6)$$

For room temperature compression testing, all following calculations are performed with room temperature dimensions substituted for hot dimensions.

To correct any error in the measurement of the load, an average of the constant load values (from before the test started) was subtracted from the instantaneous load.

The displacement value produced by the machine is the distance between the tools rather than the distance the top tool has travelled, so this displacement was subtracted from the initial hot height to give the ‘die displacement’.

The corrected load was plotted against the die displacement, and a line of best fit was applied to the linear region at the start of the test. The y intercept of the line was divided by the gradient, with this value added to the die displacement to give the ‘zero-corrected displacement’.

The final correction to the displacement allows for the discrepancy between the physical measured heights of the specimen (initial and final) and the machine measured height (start to end of the test). The initial hot height over the final hot height was divided by the maximum die displacement, and then multiplied by the zero corrected die displacement, to give the ‘corrected die displacement’.

The volume,  $V$ , of the initial compression specimen was calculated using Equation 3.7, where  $r_{hot}$  is the initial hot radius and  $h_{hot}$  is the initial hot height.

$$V = \pi r_{hot}^2 h_{hot} \quad (3.7)$$

The initial hot height was subtracted by the corrected die displacement to give the ‘corrected

die height' in order to calculate the true strain,  $\varepsilon$ . The equation for true strain is shown in Equation 3.8, where  $h_{inst}$  is the instantaneous corrected die height and  $h_{hot}$  is the initial hot height.

$$\varepsilon = -\ln\left(\frac{h_{inst}}{h_{hot}}\right) \quad (3.8)$$

The instantaneous area,  $A_{inst}$ , was calculated by dividing the volume by the instantaneous corrected die height,  $h_{inst}$ , as shown in Equation 3.9.

$$A_{inst} = \frac{V}{h_{inst}} \quad (3.9)$$

The true stress,  $\sigma$ , was calculated by dividing the corrected load,  $F$ , by the instantaneous area,  $A_{inst}$  as shown in Equation 3.10.

$$\sigma = \frac{F}{A_{inst}} \quad (3.10)$$

#### 3.5.11.1 Isothermal correction

For high temperature compression testing, an isothermal correction was necessary to allow for the variation between the actual and expected test temperatures, as well as to correct for deformation heating within the compression specimens [70].

The isothermal correction is shown in Equation 3.11, where  $\sigma_{iso}$  is the isothermally corrected stress,  $\sigma$  is the true stress,  $Q_{def}$  is the activation energy of deformation,  $R$  is the ideal gas constant,  $\beta$  is a constant,  $T_{test}$  is the test temperature in K, and  $T_{inst}$  is the instantaneous test temperature in K.

$$\sigma_{iso} = \sigma + \frac{Q_{def}}{\beta R} \left( \frac{1}{T_{test}} - \frac{1}{T_{inst}} \right) \quad (3.11)$$

To calculate  $Q_{def}$ , which varies depending on the material, the Zener-Hollomon parameter,  $Z$ , which is shown in Equation 3.12 was rearranged to give Equation 3.13, where  $\dot{\varepsilon}$  is the strain rate and  $T$  is the average temperature during compression.

$$Z = \dot{\varepsilon} \exp\left(\frac{Q_{def}}{RT}\right) \quad (3.12)$$

$$\ln \dot{\varepsilon} = -\frac{Q_{def}}{R} \left( \frac{1}{T} \right) + \ln Z \quad (3.13)$$

Stress was plotted against temperature in K for each strain rate to get the temperatures

relating to specific stress values (i.e. for 60–300 MPa).

The natural log of the strain rate,  $\ln \dot{\epsilon}$ , was then plotted against  $\left(\frac{1}{T}\right)$  at each stress value to give gradients of  $\left(-\frac{Q_{def}}{R}\right)$ . Each gradient was multiplied by  $-R$  to give the  $Q_{def}$  value, and the  $Q_{def}$  values were averaged for all stress values to give one value.

Different strain values produce different values for  $Q_{def}$ , so this methodology was initially done for strains of 0.1–0.6. However, the  $Q_{def}$  values were very high and over-corrected for the deformation heating in the flow stress. Consequently, only the value for steady stress, i.e. at strain of 0.6, was used.

To calculate  $\beta$ , Equation 3.14 was rearranged to give Equation 3.15, and  $\ln Z$  was plotted against  $\sigma$ .

$$Z = A_2 \exp(\beta\sigma) \quad (3.14)$$

$$\ln Z = \beta\sigma + \ln A_2 \quad (3.15)$$

Table 3.3 shows the  $Q_{def}$  values calculated for all three FAST conditions, for a strain of 0.6 (i.e. at steady state stress).

Table 3.3:  $Q_{def}$ , activation energy for deformation, values for all FAST conditions: 850, 930, and 1000°C

	850°C	930°C	1000°C
$Q_{def}$ [Jmol <sup>-1</sup> ]	189163	248817	227907

### 3.5.11.2 Friction correction

Due to friction effects during compression, a friction correction was required following the isothermal correction. This correction is shown in Equation 3.16, where  $\sigma_{fr}$  is the friction corrected stress,  $m$  is the friction factor, and  $d$  is the instantaneous diameter (calculated using the instantaneous area) [71].

$$\sigma_{fr} = \frac{\sigma_{iso}}{1 + \left(\frac{md}{3\sqrt{3}h_{inst}}\right)} \quad (3.16)$$

In order to get a good approximation for the shear friction factor,  $m$ , simulations of one of the compression tests modelled using finite element modelling (FEM) software were run for multiple  $m$  values (0.1 to 0.5). The load displacement data generated by FEM was compared

to the experimental data, and an  $m$  value of 0.1 was found to be closest to the experimental data.

### 3.5.12 Finite element modelling (FEM)

In order to prepare a material model for finite element modelling software, DEFORM<sup>TM</sup> [72], friction corrected flow stress data was interpolated and values were taken at specific true strain values between 0 and 0.6 (so that they were the same for each test). Only the plastic sections of the flow stress curves were used, as the material response was assumed to be fully plastic. Material models were produced for 850, 930, and 1000°C FAST conditions.

All simulations were performed with heat transfer activated, to simulate the real compression as closely as possible. Poisson's ratio of 0.31 and a thermal conductivity as a function of temperature were also used for all simulations (8–18 W/m/K from 0–700°C) [73].

#### 3.5.12.1 Compression of cylindrical specimens

The material models were input into DEFORM<sup>TM</sup> and a simple isothermal axisymmetric compression of a cylinder was performed for each temperature, strain rate, and starting FAST condition. The mesh size was set at 1000 elements. A value of 0.1 was used for the shear friction factor,  $m$ , for all simulations. All simulations were performed in 2D for one half of the compressed cylinder, due to the vertical symmetry.

An example is shown in Figure 5.6 which demonstrates the distribution of strain in a compressed specimen.

#### 3.5.12.2 Compression of double truncated cones

A simulation of an isothermal axisymmetric compression of a double truncated cone was performed for each FAST condition (850, 930, and 1000°C) at a compression temperature of 785°C and a strain rate of 0.1 s<sup>-1</sup>. The mesh size was set at 1000 elements. A value of 0.1 was used for the shear friction factor,  $m$ , for all simulations. All simulations were performed in 2D for one half of the compressed double truncated cone, due to the vertical symmetry.

An example is shown in Figure 5.8 which demonstrates the distribution of strain in a compressed specimen.

#### 3.5.12.3 Large-scale forging of double truncated cones

Non-isothermal simulations of the large-scale forging of double truncated cones were performed at forging temperatures of 785, 810, and 835°C and a strain rate of 3 s<sup>-1</sup>, using the 1000°C



FAST material model generated in Section 3.5.12.1.

The forging platens had temperatures of 250 and 230°C at the top and bottom, respectively, and the environment temperature was 20°C. A value of 0.3 was chosen for the constant shear friction factor,  $m$ , between the specimen and the dies, as suggested by DEFORM<sup>TM</sup> [74] and Grote and Antonsson [75] for hot forging of metals. The mesh size was set at 1000 elements.

All simulations were performed in 2D for one half of the forged double truncated cone, due to the vertical symmetry.

An example is shown in Figure 5.10 which demonstrates the distribution of strain in a forged specimen.

#### *3.5.12.4 Complex ‘eye bolt’ forging*

A complex multi-blow drop hammer forging of an ‘eye bolt’ was simulated using the 1000°C FAST material model generated in Section 3.5.12.1. The energy of the hammer was fixed at  $1.1 \times 10^7$  Nmm. The mass was unknown and different masses were tried until the simulation dimensions matched those of the physical specimen, which was at 800 kg.

The mesh size was set at 64000 elements to ensure that high strain regions were calculated accurately. The top and bottom dies were gas heated at  $\sim 75^\circ\text{C}$ , and the environment temperature was 30°C. A value of 0.3 was chosen for the constant shear friction factor,  $m$ .

Six different stages were used to model the multi-blow forging: (1) heat transfer through air for the transfer of the forging from the furnace to the forge (5 s) with starting temperature of 797°C; (2) rest on die for the time taken to correctly place the forging on the starter bottom die before forging (2 s); (3) first multi-blow forging on the starter die for five blows; (4) heat transfer through air for the transfer of the forging from the starter die to the finisher die (1 s); (5) rest on die for the time taken to correctly place the forging on the finisher bottom die before forging (1 s); (6) second multi-blow forging on finisher die for six blows.

The simulation was performed in 3D for the whole forged specimen, to ensure an accurate simulation was produced.

## Chapter 4

# Small-scale FAST of Ti-5553

### 4.1 Outline

This chapter presents the initial determination of the ability of FAST to produce consolidated Ti-5553 pre-forged billets, examining the effects of varying dwell temperature and dwell time on the  $\beta$  grain size,  $\alpha$  volume fraction, and density. FAST specimens were produced from Batch 1 powder at dwell temperatures of 800, 850, 900, 930, 970, 1000, and 1200°C and at dwell times of 3, 10, 30, and 60 min, as described in Chapter 3. Specimens were prepared metallographically and examined under SEM, and from this the  $\alpha$  volume fraction,  $\beta$  grain size, and density were determined, as described in Chapter 3.

## 4.2 Results

### 4.2.1 Microstructural examination

#### 4.2.1.1 Below $\beta$ transus temperature

The microstructures of the Ti-5553 FAST specimens produced at dwell temperatures of 800 and 850°C, below the  $\beta$  transus temperature ( $\sim 890^\circ\text{C}$ ), are shown in Figure 4.1 for dwell times of 3–60 min. The cooling rate was  $\sim 250^\circ\text{C}/\text{min}$  for all specimens, in order to retain the microstructure. Dark primary  $\alpha$  grains can be observed in all microstructures, regardless of FAST dwell temperature and time. These primary  $\alpha$  grains appear to grow as the dwell time increases at 800°C, Figure 4.1a, whereas at 850°C they appear to reduce in number, Figure 4.1b.

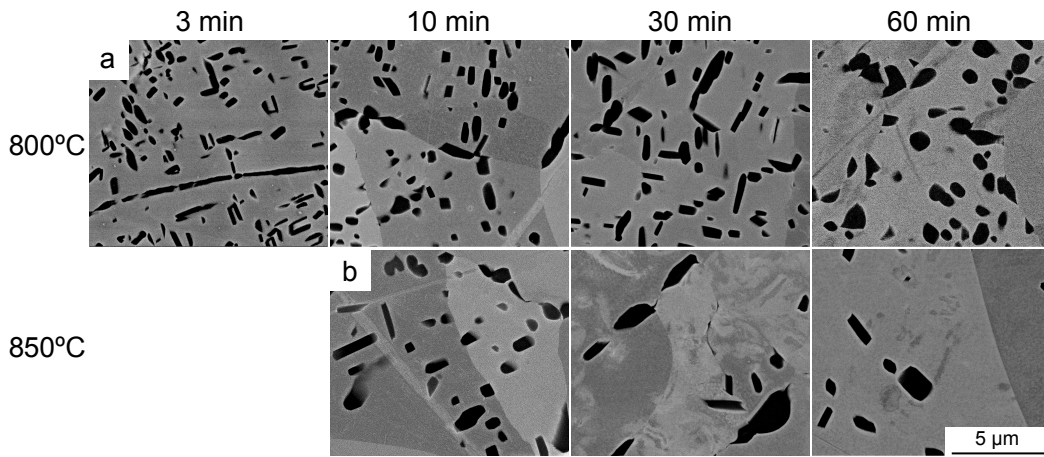


Figure 4.1: BSEI micrographs of FAST specimens produced at 3, 10, 30, and 60 min dwell times for temperatures of (a) 800°C, and (b) 850°C

#### 4.2.1.2 Above $\beta$ transus temperature

The microstructures of the Ti-5553 FAST specimens produced at dwell temperatures above the  $\beta$  transus transus temperature, 900–1200°C, are shown in Figures 4.2 and 4.3 for dwell times of 3–60 min. The cooling rate was  $\sim 250^\circ\text{C}/\text{min}$  for all specimens, in order to retain the microstructure.

At all dwell temperatures and dwell times there are equiaxed  $\beta$  grains. There is no evidence of primary  $\alpha$  grains, and minimal evidence of grain boundary (g.b.)  $\alpha$  in the microstructures.

As the temperature increases, from Figure 4.2a to Figure 4.3b, the  $\beta$  grain size increases, with the largest grain sizes at 1200°C. However, the effect of the dwell time on the  $\beta$  grain size is less obvious.

At some temperatures, 900, 930, and 970°C (Figure 4.2a, b, and c), there is  $\beta$  grain growth

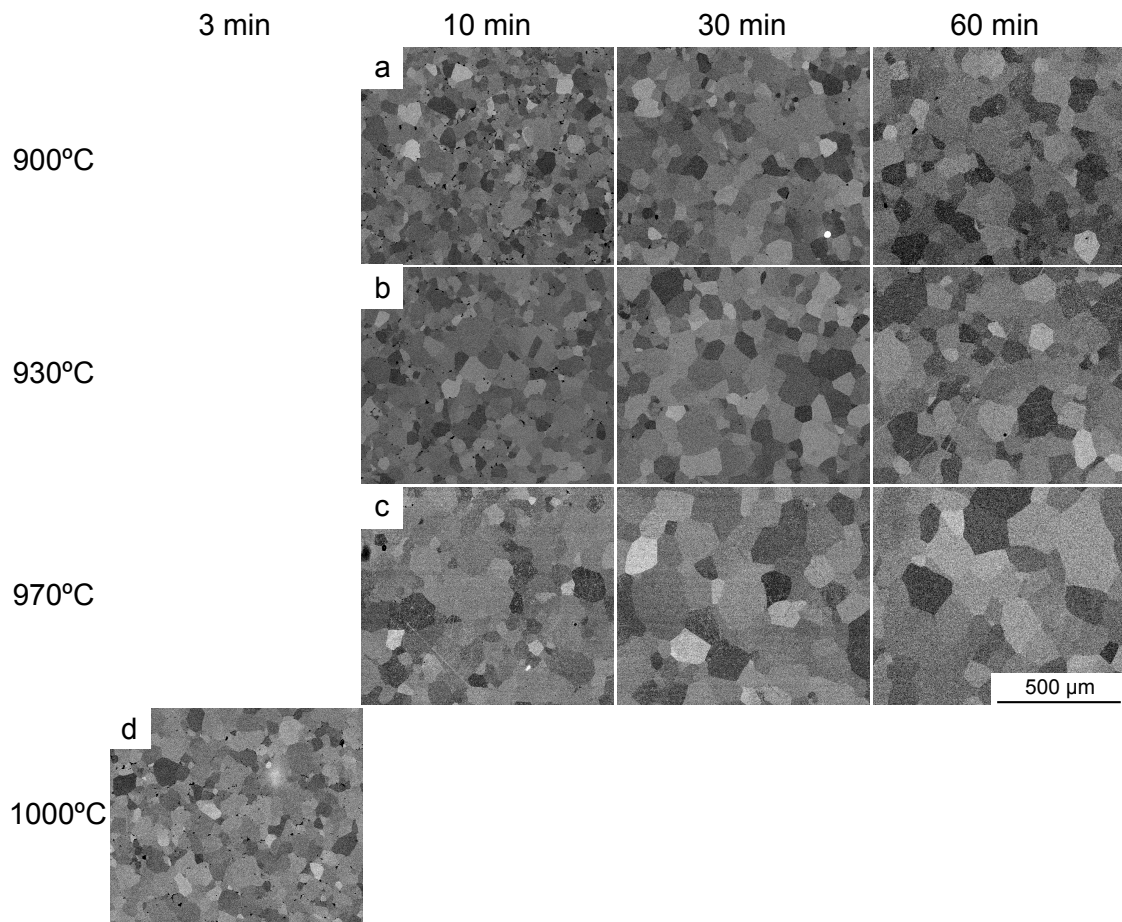


Figure 4.2: BSEI micrographs of FAST specimens produced at 3, 10, 30, and 60 min dwell times for temperatures of (a) 900°C, (b) 930°C, (c) 970°C, and at a 3 min dwell time only for (d) 1000°C

between dwell times of 10 and 30 min, but minimal growth between 30 and 60 min. There is also more porosity for a dwell time of 10 min compared to 30 and 60 min, for all three temperatures.

The specimen produced at 1000°C and a dwell time of 3 min is also shown in Figure 4.2d because the scale in Figure 4.3 does not show the details of the microstructure. The  $\beta$  grain size and level of porosity are similar to that of the specimen produced at 930°C and a dwell time of 10 min.

Figure 4.3 shows that there is  $\beta$  grain growth between 3 and 10 min, and some between 30 and 60 min for both 1000 and 1200°C. Both temperatures show minimal grain growth between 10 and 30 min. However, this effect is more pronounced at 1000°C than 1200°C.

#### 4.2.2 $\alpha$ volume fraction measurements

The  $\alpha$  volume fraction was measured for all the specimens produced below the  $\beta$  transus, 800 and 850°C, Figure 4.4a.

As the dwell time increases, the  $\alpha$  volume fraction increases for the 800°C specimen and

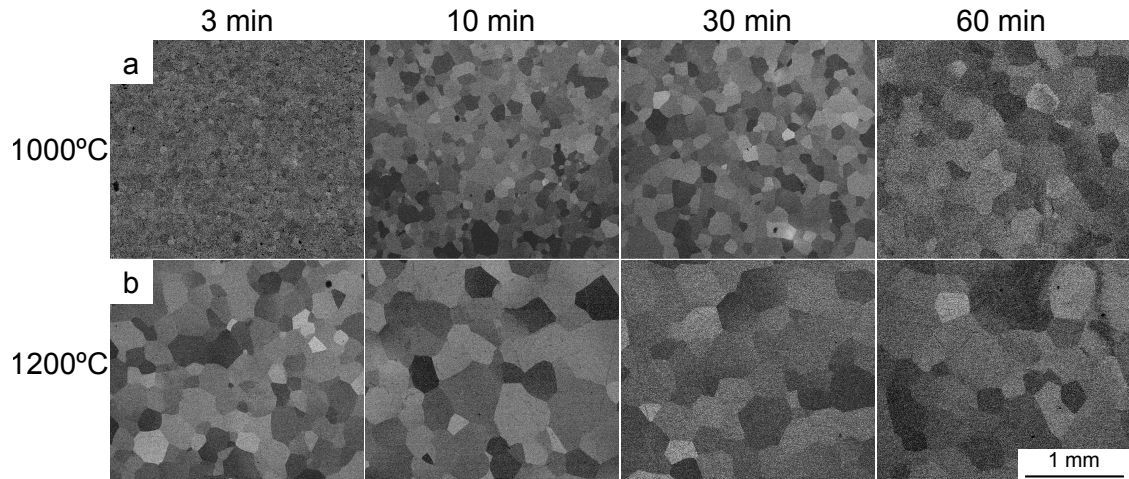


Figure 4.3: BSEI micrographs of FAST specimens produced at 3, 10, 30, and 60 min dwell times for temperatures of (a) 1000°C, and (b) 1200°C

decreases for the 850°C specimen, due to the proximity of 850°C to the  $\beta$  transus temperature.

There is a discrepancy between the volume fraction of  $\alpha$  in Figure 4.4a and in Figure 3.5 due to the different chemistries of the Ti-5553 powders in Batch 1 and Batch 2, respectively (Table 3.2). The chemistry does not differ substantially, however it will be sufficient to have an effect on the formation of  $\alpha$  at certain temperatures.

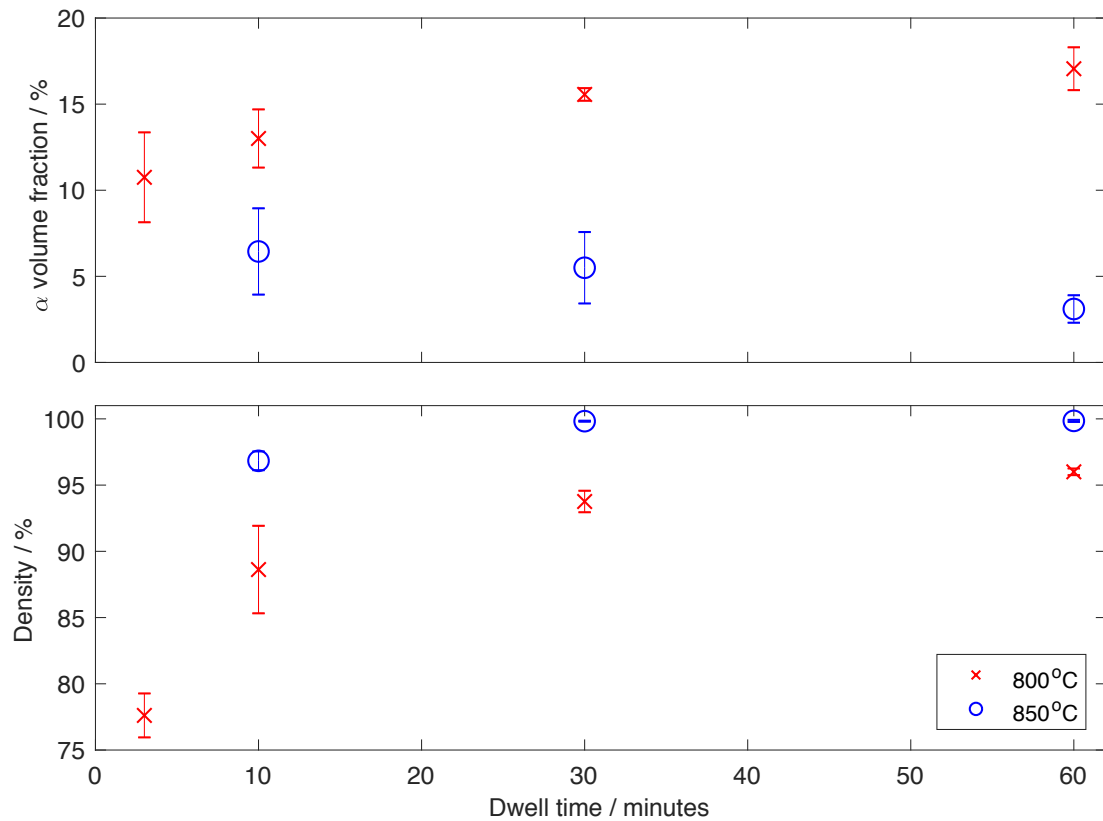


Figure 4.4: FAST specimens produced at 800 and 850°C: effect of dwell time on (a)  $\alpha$  volume fraction and (b) density

### 4.2.3 $\beta$ grain size measurements

$\beta$  grain size measurements were performed for all specimens produced above the  $\beta$  transus, in order to examine the effect of dwell temperature and time on the mean  $\beta$  grain size, Figures 4.5 and 4.6.

Both figures show that there is generally an increase in  $\beta$  grain size with increasing temperature for all dwell times. From Figure 4.5, it appears that the increase in grain size is roughly exponential from 900–1000°C for all dwell times. However, between 1000 and 1200°C the increase in grain size is linear, and does not continue the exponential trend, due to the reduction in driving force.

The  $\beta$  grain size at 1200°C was far higher than the other temperatures for all dwell times, with the grain size at a dwell time of 3 min being approximately the same as the grain size of the specimen produced at 1000°C and 60 min, Figure 4.5.

The effect of dwell time on the grain size is more complicated than that of dwell temperature. At 900 and 930°C the dwell time has minimal effect on the grain size, Figure 4.5. The grain size values are also very similar for 900 and 930°C at all dwell times, Figure 4.6. The grain size shows more dependence on dwell time at a dwell temperature of 970°C, Figure 4.5. For dwell temperatures of 1000 and 1200°C there is a large increase in grain size between dwell times 3–10 min, minimal grain growth between dwell times 10–30 min, and another large increase in grain size between dwell times 30–60 min, Figure 4.6.

In general, the dwell temperature appears to have more effect than the dwell time on the  $\beta$  grain size.

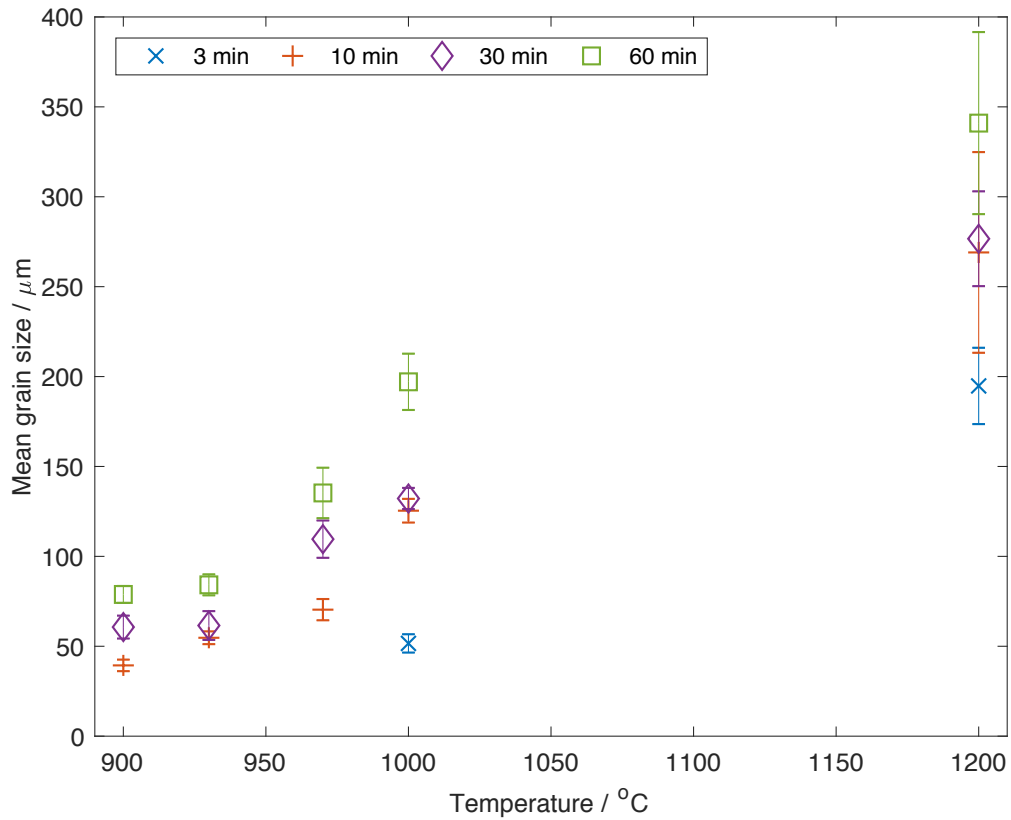
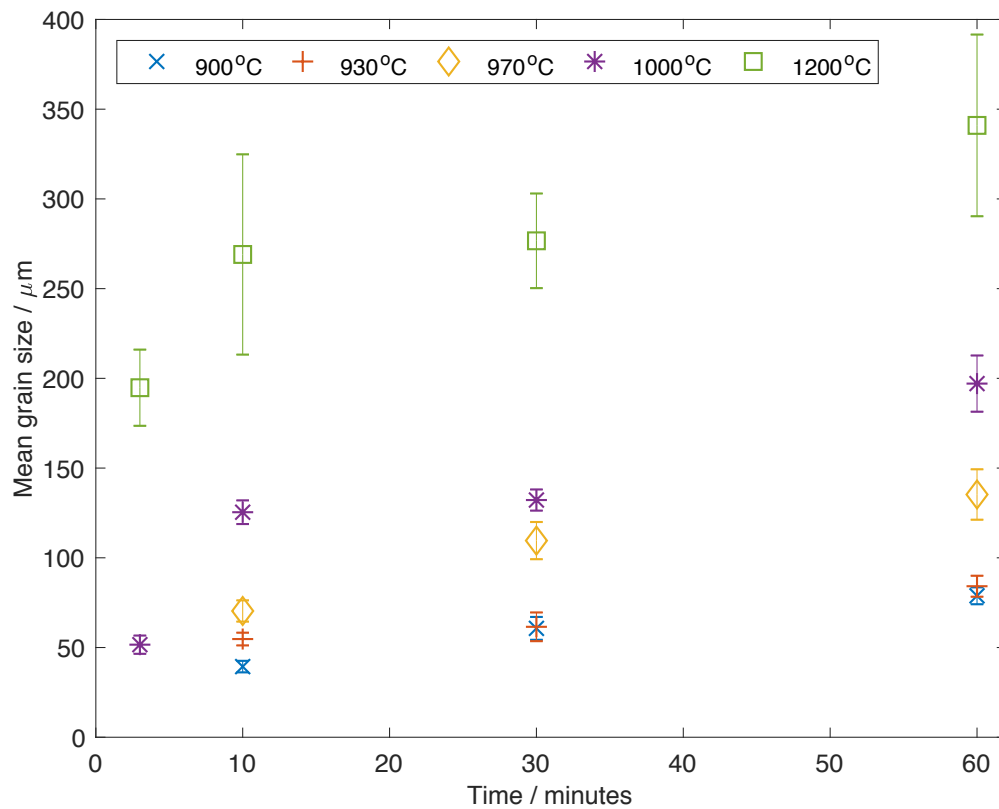
### 4.2.4 Density calculations

Density measurements were produced for all FAST specimens, Figures 4.4 and 4.7.

In Figure 4.4 there is a large difference between the densities of specimens produced below, and just below, the  $\beta$  transus, 800°C and 850°C, respectively. The density at 850°C was between 95 and 100 % for dwell times 10–60 min, whereas the densities of the 800°C specimens were lower, and varied from ~77 % to just over 95 % from 3–60 min.

In Figure 4.7 the density is between 99.5 and 100 % for all dwell times at a dwell temperature of 1200°C. However, at 1000°C there is a significant increase in the density between dwell times of 3 and 10 min.

Dwell temperatures of 850, 900, and 930°C produced densities below that of the higher dwell temperatures at a dwell time of 10 min, although by a dwell time of 30 min the density is greater than 99.5 % for all temperatures (850–1200°C).

Figure 4.5: Mean  $\beta$  grain size against dwell temperature for various FAST dwell timesFigure 4.6: Mean  $\beta$  grain size against dwell time for various FAST dwell temperatures

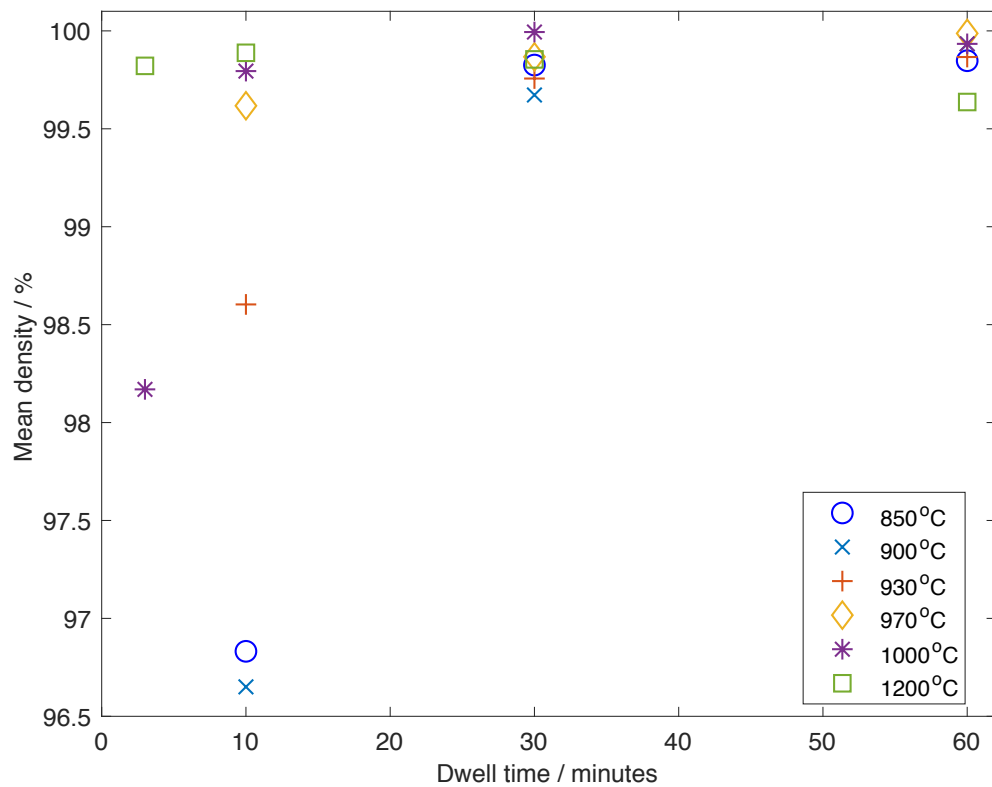


Figure 4.7: Mean density against dwell time for dwell temperatures 850–1200°C. Errorbars were not plotted to ensure that the mean densities could be easily interpreted. However, the relative accuracy of the mean density was calculated to be 1.57 %



## 4.3 Discussion

### 4.3.1 Analysis of specimens produced below the $\beta$ transus

Specimens produced at 800 and 850°C (below the  $\beta$  transus of  $\sim 890^\circ\text{C}$ ) contained primary  $\alpha$  grains within a  $\beta$  matrix, Figure 4.1.

These primary  $\alpha$  grains were shown to grow in the specimens produced at 800°C as the dwell time increased, Figure 4.1a. Increased time at temperature caused some of the  $\alpha$  grains to dissolve, and others to grow preferentially due to extended diffusion. The  $\alpha$  volume fraction was found to increase with dwell time overall in Figure 4.4. This is likely due to the dwell temperature of 800°C being significantly below the  $\beta$  transus temperature.

However, at 850°C the volume fraction of  $\alpha$  was seen to reduce as the dwell time increased, Figures 4.1b and 4.4. Increased time at temperature caused some of the  $\alpha$  grains to dissolve, due to the proximity to the  $\beta$  transus temperature.

Figure 4.4 also shows the densities for the specimens produced at 800 and 850°C. The densities of specimens produced at 850°C were between 95 and 100 % for dwell times 10–60 min, whereas the densities of the 800°C specimens were between  $\sim 77$  % and 95 % from 3–60 min. This may be in part due to the higher volume fraction of  $\alpha$  phase at 800°C compared to 850°C, as the rate of diffusion is slower in the  $\alpha$  phase than in the  $\beta$  phase [13]. There will also be more diffusion due to the 50°C difference in temperature, and therefore more closure of porosity in the 850°C specimens.

### 4.3.2 Analysis of specimens produced above the $\beta$ transus

Specimens heated to above the  $\beta$  transus, 900–1200°C, show very little sign of grain boundary  $\alpha$ , Figures 4.2 and 4.3, due to the very fast cooling rate ( $\sim 250^\circ\text{C}/\text{min}$ ). This is an advantage as grain boundary  $\alpha$  detrimentally affects ductility [22].

This has been seen in previous work, which found that water quenched and air cooled Ti-5553 produced microstructures devoid of grain boundary  $\alpha$  [26]. It has also been shown that it is possible to retain 100 % metastable  $\beta$  upon cooling from the  $\beta$  phase field at rates as slow as  $0.25^\circ\text{C}/\text{s}$ , which would suggest that the microstructure seen in Figure 4.2 is retained metastable  $\beta$  [23]. A possible explanation for the lack of  $\alpha$  phase is that  $\omega$  phase, too fine to be seen under scanning electron microscopy, has formed during cooling from the  $\beta$  phase field. This has been suggested in other literature as a reason for a lack of  $\alpha$  phase in their microstructures [23].

The  $\beta$  grain size varied greatly in the specimens produced above the  $\beta$  transus temperature, depending on the dwell temperature and time, Figures 4.2 and 4.3.

Higher temperatures were shown to produce an increase in the  $\beta$  grain size, especially at 1200°C in Figures 4.2, 4.3, 4.5, and 4.6. An increase of 300°C, from 900–1200°C, at a dwell time of 60 min produced a  $\beta$  grain size which was more than four times larger, which shows that the temperature has a large effect on grain size. This increase in grain size with increasing time at temperature is as described for most materials, and in addition, externally applied forces can induce grain boundary migration and therefore provide an additional driving force for grain growth [15].

However, very similar grain sizes were observed for 900 and 930°C specimens in Figure 4.2a and b, and Figures 4.5 and 4.6. Between 900 and 1000°C, the grain size increased exponentially with an increase in temperature for all dwell times, Figure 4.5. This may be due to the driving force for grain growth being suppressed at lower temperatures, as any porosity present at lower temperatures will act as solute or second-phase particles, pin grain boundaries, and thereby prevent grain growth [15]. However, between 1000 and 1200°C the increase in grain size is linear, and does not continue the exponential trend due to a reduction in the driving force.

It is also interesting to note that the grain size for the specimen produced by FAST at 930°C dwell temperature and 30 min dwell time has a grain size of approximately 62  $\mu\text{m}$ , whereas in literature, a specimen solution heat treated at 925°C for 30 min produced a grain size of 700  $\mu\text{m}$  [35]. This implies that the FAST process has the ability to control the  $\beta$  grain size during processing and produce small  $\beta$  grains, which is highly advantageous [12].

The dependence of the  $\beta$  grain size on dwell time is less consistent than for the dwell temperature, Figures 4.6, 4.2, and 4.3. For some temperatures, 900, 930, and 970°C, the grain size increases between dwell times 10–30 min, but remains relatively constant between 30–60 min. However, at 1000 and 1200°C there is a significant increase in grain size between dwell times 3–10 min, minimal grain growth between dwell times 10–30 min, and another increase in grain size between dwell times 30–60 min.

One explanation for the increase in grain size between 3–10 min at 1000°C, and between 10–30 min at 900, 930, and 970°C is the reduced porosity, Figures 4.2 and 4.7. The porosity may pin the grains and prevent grain growth, until it is removed at a higher dwell time and grain growth increases extensively.

However, it is unclear why there is a difference between the grain size relationships between 10–30 min and 30–60 min dwell times for 1000 and 1200°C, as the porosity is relatively constant, and it would be expected that the increase in grain size would be relatively linear with increasing dwell time.

The only explanations would be that there is a reduction in the driving force for grain growth

between 10–30 min dwell time, which is then removed between 30–60 min, or that there is an increase in the driving force for grain growth between 30–60 min by some unknown mechanism.

The FAST process is more complicated than conventional sintering, as it uses an electric current to directly heat the powder particles (by joule heating), which may have an unknown effect on the mechanisms behind grain growth, and could explain these unusual results.

Overall, though, the  $\beta$  grain growth is less influenced by the dwell time than the dwell temperature. This agrees with previous findings which showed that there was minimal grain growth when the dwell time was increased from 10–30 min for Ti-5553 [64].

Figure 4.7 shows that the porosity generally decreased as the dwell time increased. This is due to the extended time for diffusion to occur, which allowed more porosity to be removed. It also shows that although there is variation in porosity at the lower temperatures and lower dwell times, the density is greater than 99.5 % for all temperatures for dwell times of 30 min or more. It is possible that any remaining porosity will be removed during subsequent thermomechanical processing, i.e. forging, to produce a fully dense material.

## 4.4 Conclusions

1. It has been shown that field-assisted sintering technology (FAST) or spark plasma sintering (SPS) has the capability to produce an equiaxed  $\beta$  grain microstructure for temperatures above the  $\beta$  transus, and allows the  $\beta$  grain size to be controlled effectively by adjusting the dwell temperature and dwell time. This level of control is not possible in most conventional processing methods, and is therefore a major advantage of the process.
2. The  $\beta$  grain size was found to largely increase with the dwell temperature, whereas the relationship between the grain size and the dwell time was more complicated. An exponential increase in the grain size was found between 900–1000°C for all dwell times, although this rate reduce between 1000–1200°C. At 900, 930, and 970°C there was some grain growth between 10–30 min and minimal between 30–60 min. There were large increases in the grain size between 3–10 min and 30–60 min dwell times for 1000 and 1200°C, with a minimal increase in grain size between 10–30 min, perhaps due to an unknown effect of the FAST process on the mechanisms behind grain growth. The increase in grain size between 3–10 min at 1000°C, and between 10–30 min at 900, 930, and 970°C may be due to the reduced porosity, which could pin the grains and prevent grain growth. However, overall, the dwell time had less effect on the grain size than the dwell temperature.
3. Specimens produced below the  $\beta$  transus were found to contain primary  $\alpha$  grains. At 800°C the  $\alpha$  volume fraction increased with increasing dwell time, whereas at 850°C the  $\alpha$  volume fraction decreased. This led to an increased density in the 850°C specimens compared to the 800°C specimens.
4. The density of specimens produced by FAST varied depending on the dwell temperature and dwell time. Below the  $\beta$  transus the density was reasonably low, but around and above the  $\beta$  transus this rose to between 96.5 and 100 %. Densities of between 99.5 and 100 % were possible for all dwell temperatures at dwell times of 30 min or above, and any residual porosity may be removed during subsequent thermomechanical processing i.e. forging.

## Chapter 5

# Large-scale FAST of Ti-5553

### 5.1 Outline

This chapter presents the ability of FAST to produce consolidated Ti-5553 pre-forged billets on a large-scale, as well as the subsequent forging behaviour and heat treat-ability, at both the small-scale using compression testing and the large-scale using industrial upset forging.

The majority of the experimental procedures used for this chapter can be found in more detail in Chapter 3.

## 5.2 Experimental procedure

### 5.2.1 Large-scale forging study

One of the FAST specimens produced at 1000°C, Figure 5.1a, was machined to produce three double truncated cones, as shown in Figure 5.1b, to be forged at AFRC (Advanced Forming Research Centre, The University of Strathclyde). Double truncated cones were used to provide a large variation of strain within a single specimen. The dimensions of the double truncated cones were based on previous work [66], and were limited by the height of the FAST specimen.

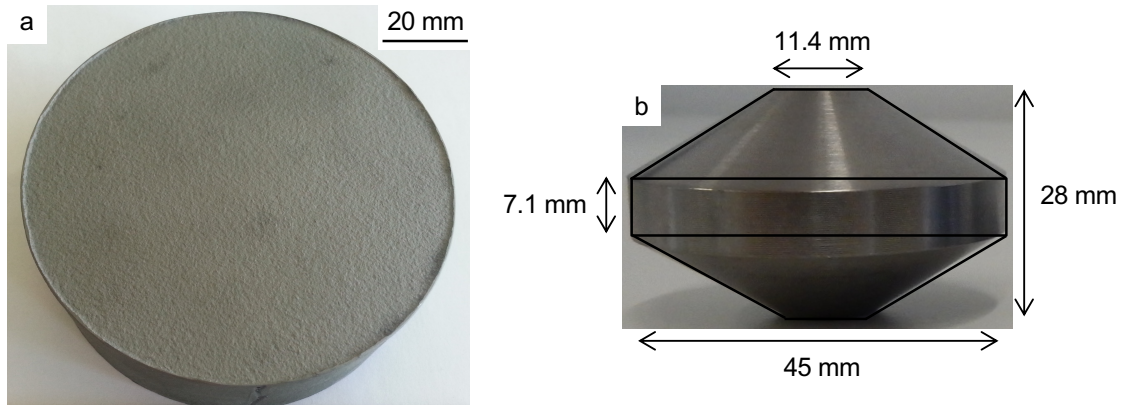


Figure 5.1: Examples of (a) a specimen produced by FAST, and (b) a double truncated cone machined from the FAST billet for forging

The double truncated cones were coated in Deltaglaze glass lubricant and boron nitride to prevent adhesion, and then pre-heated in a furnace at 785, 810 and 835°C for 20 min before being forged. Forging was performed using a 21,000 kN (2100 t) screw press, as shown in Figure 5.2c. The upper platen was heated to 250°C and the lower platen to 230°C, with graphite spray used to lubricate the platens for forging. The double truncated cones were forged to 1.2 strain, with the energy set at 5 %. Following analysis of the forging data, the strain rate was found to be approximately  $3 \text{ s}^{-1}$ . The forged cones were water quenched to preserve the forged microstructure.

The forged cones were sectioned into two halves: one half to be observed using SEM and the other half to be heat treated (solution treated and aged) at Safran Landing Systems in Gloucester using an industrial furnace. Solution treatment was performed for 4 h at a proprietary temperature between 750 and 850°C, and ageing for 8 h at a proprietary temperature below 650°C in an inert atmosphere, before air cooling to room temperature. The forged and heat treated sections observed under microscopy are shown in Figure 5.3.



Figure 5.2: Photographs of large-scale forging of the double truncated cones (a) before forging and (b) after forging, and (c) the 2100 t screw press at the Advanced Forming Research Centre (AFRC) which was used for the large-scale forging

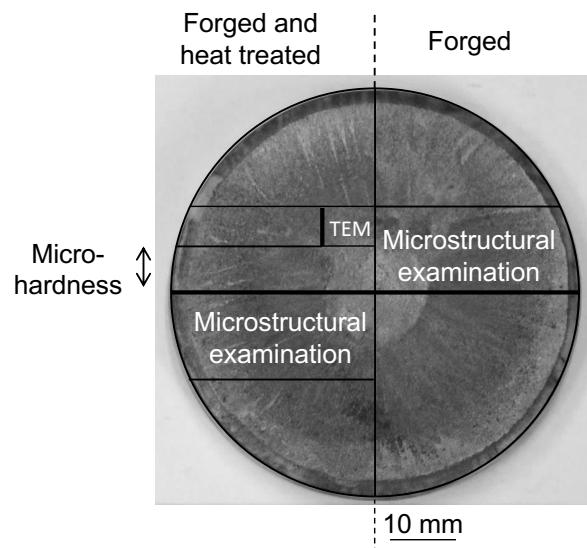


Figure 5.3: Diagram indicating where the specimens for microstructural examination, microhardness, and transmission electron microscopy (TEM) were taken from in the forged and heat treated halves of the forged cones (the thick black line indicates the faces observed under microscopy and used for microhardness testing)

## 5.3 Results

### 5.3.1 Analysis of post-FAST billets

Four large-scale FAST specimens were produced as described in Chapter 3: one at 850°C, one at 930°C, and two at 1000°C, all with a 30 min dwell time. Density measurements, microhardness, SEM, and TEM were performed on the post-FAST material.

#### 5.3.1.1 Density

Density measurements of the Ti-5553 post-FAST microstructures were very close to full consolidation:  $99.98 \pm 0.01$  % at 850°C;  $99.97 \pm 0.02$  % at 930°C;  $99.96 \pm 0.01$  % at 1000°C (large-scale forging study); and  $99.98 \pm 0.01$  % at 1000°C (compression testing). Any residual porosity was expected to be closed up by subsequent hot forging or compression.

#### 5.3.1.2 Microstructural evolution

The light micrograph, Figure 5.4a, shows that the initial powder has equiaxed  $\beta$  grains of approximately 10  $\mu\text{m}$ . The BSEI micrograph of the material produced by FAST at a temperature of 850°C of the same scale, Figure 5.4c, has relatively similar  $\beta$  grain sizes, which is due to primary  $\alpha$  grains formed during FAST processing pinning them and preventing grain growth [24]. The microstructure is a mixture of blocky platelet  $\alpha$ , formed because of FAST processing high in the  $\alpha + \beta$  phase field, and retained  $\beta$  phase [13]. However, above the  $\beta$  transus temperature, at 930 and 1000°C, the primary  $\alpha$  has fully transformed to the  $\beta$  phase, due to FAST processing above the  $\beta$  transus temperature ( $\sim 890^\circ\text{C}$ ). At this temperature the lack of primary  $\alpha$  grains enabled significant  $\beta$  grain growth to approximately five times the initial powder grain size. As the cooling rate was relatively slow, secondary  $\alpha$  has formed along the grain boundaries and very fine secondary  $\alpha$  laths have precipitated within the grain upon cooling, Figure 5.4d [24]. The grain boundary  $\alpha$  is approximately 0.1  $\mu\text{m}$  thick, and the much finer secondary  $\alpha$  has grown from the grain boundary towards the centre of the prior  $\beta$  grain.

Microstructures for both 1000°C post-FAST specimens have been included to show the starting microstructures for the compression testing study and the large-scale forging study. There is minimal difference in  $\beta$  grain size and secondary  $\alpha$  morphology between the two specimens.

#### 5.3.1.3 Microhardness

Microhardness values of the post-FAST specimens were measured at:  $375 \pm 5$  HV at 850°C;  $436 \pm 3$  HV at 930°C;  $446 \pm 2$  HV at 1000°C (large-scale forging study); and  $439 \pm 2$  HV at



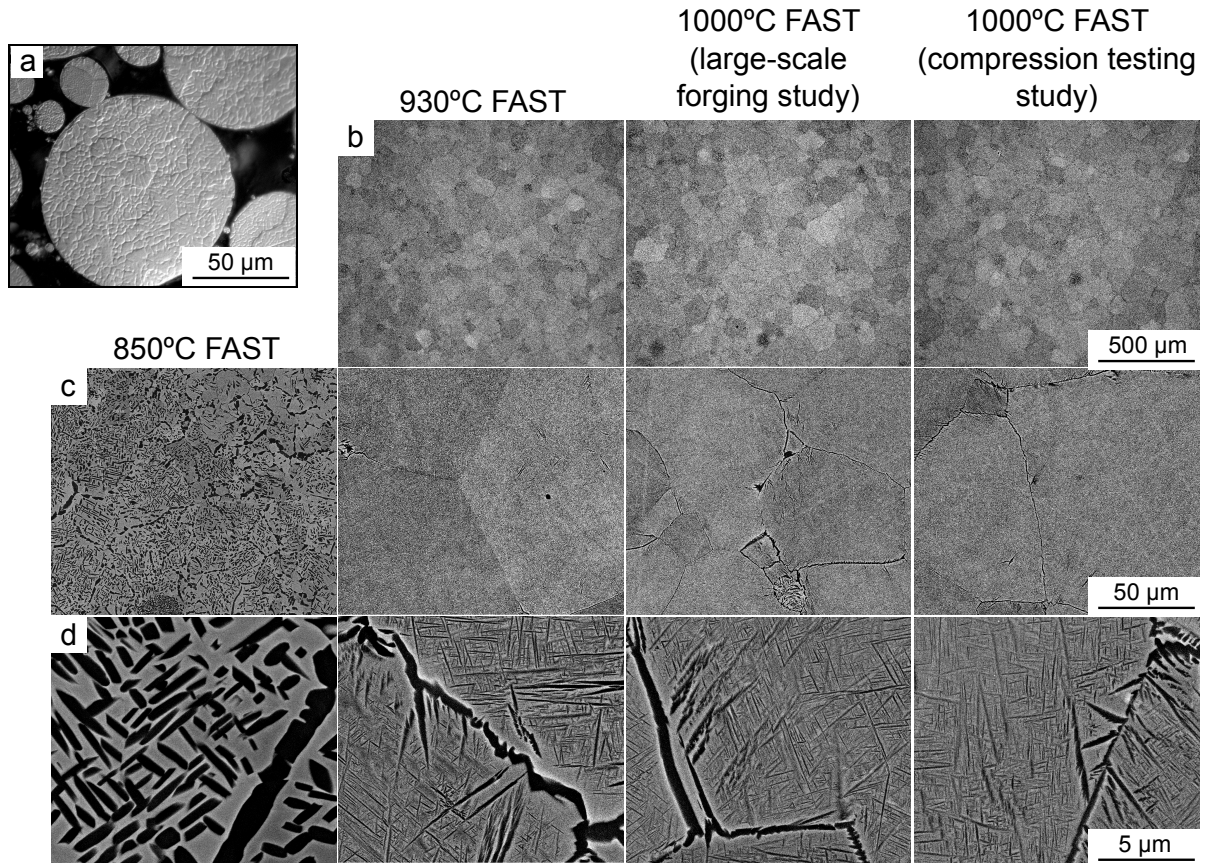


Figure 5.4: Comparison between (a) a light micrograph of Ti-5553 gas atomised powder, and BSEI micrographs of FAST specimens produced at 850, 930, and 1000°C for (b) low, (c) medium, and (d) high resolution

1000°C (compression testing study).

#### 5.3.1.4 Transmission electron micrographs

Transmission electron microscopy (TEM) was used to determine if there were differences between specimens produced by FAST at 930 and 1000°C at resolutions higher than could be achieved by SEM, Figure 5.5. The  $\alpha$  precipitates appear to be coarser at 1000°C when compared to 930°C at all magnifications.

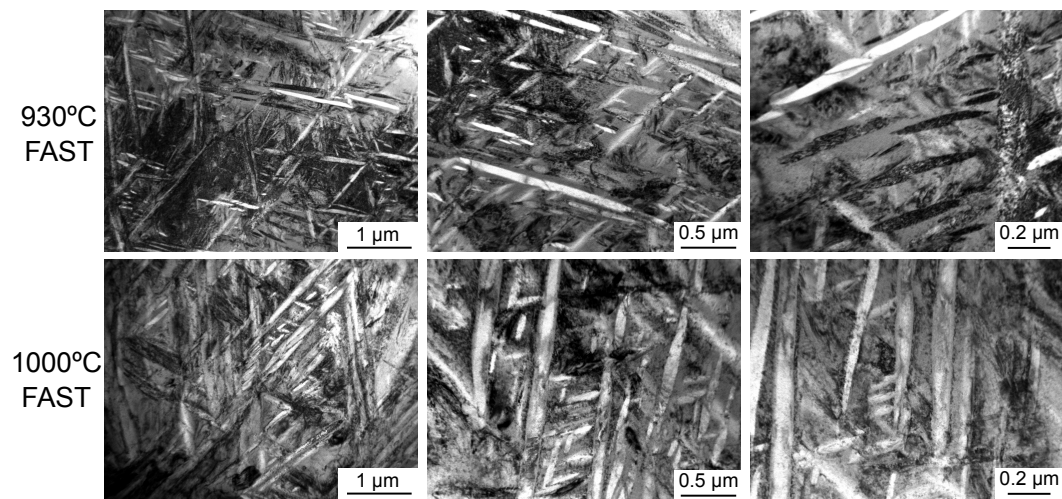


Figure 5.5: Transmission electron micrographs of FAST specimens produced at 930 and 1000°C (bright field)

### 5.3.2 Analysis of compressed Ti-5553 cylinders

Twelve cylindrical compression specimens were machined from three of the FAST specimens: 850, 930, and 1000°C. A test matrix of temperatures 785, 810, 835°C and strain rates 0.01, 0.1, 1, 5 s<sup>-1</sup> was used for compression testing of the cylinders, in order to generate flow curves. Analysis of the cylinders includes SEM, flow stress analysis, and FEM.

#### 5.3.2.1 Microstructural evolution and FEM modelling

The high (centre) and low (side edge) strain microstructures of the specimens compressed at 1 s<sup>-1</sup> are shown in Figure 5.6 for each FAST condition and compression temperature, with the corresponding effective strain values generated by FEM simulations. An example of an FEM simulation, for the specimen produced by FAST at 1000°C and compressed at 785°C and 1 s<sup>-1</sup>, is shown to illustrate the distribution of strain during compression testing.

An increase in the compression temperature slightly coarsens the secondary  $\alpha$  in the microstructures of the 930 and 1000°C post-FAST specimens, owing to increased diffusion at higher temperatures. There is also a lower primary and secondary  $\alpha$  volume fraction for all FAST conditions at a compression temperature of 835°C compared to 785 and 810°C.

A comparison between the high and low strain microstructures shows that the volume fraction of primary  $\alpha$  in the 850°C post-FAST specimen is largely unaffected by increasing strain. The only change to the primary  $\alpha$  is the deformation of the  $\alpha$  grains perpendicular to the forging direction at high strain, as described for  $\beta$  alloys and as found previously for Ti-5553 [26, 76].

The microstructure of the 930 and 1000°C post-FAST specimens, however, shows more dependence on the amount of strain. The acicular secondary  $\alpha$  laths present in the low strain micrographs become broken up and spherodised at high strain.

It can also be seen that the  $\alpha$  phase volume fraction is slightly lower at high strain than at low strain for 930°C, and much lower at 1000°C, due to partial dissolution of the  $\alpha$  phase during compression.

There is some indication of  $\beta$  sub-grains in the high strain microstructures in Figure 5.6, especially in the specimens with higher strain values.

#### 5.3.2.2 Flow curves

Figure 5.7 shows the dependence of the flow stress on true strain for the 850, 930, and 1000°C post-FAST specimens, for all compression temperatures and strain rates (785, 810, and 835°C, and 0.01, 0.1, 1, and 5 s<sup>-1</sup>, respectively).

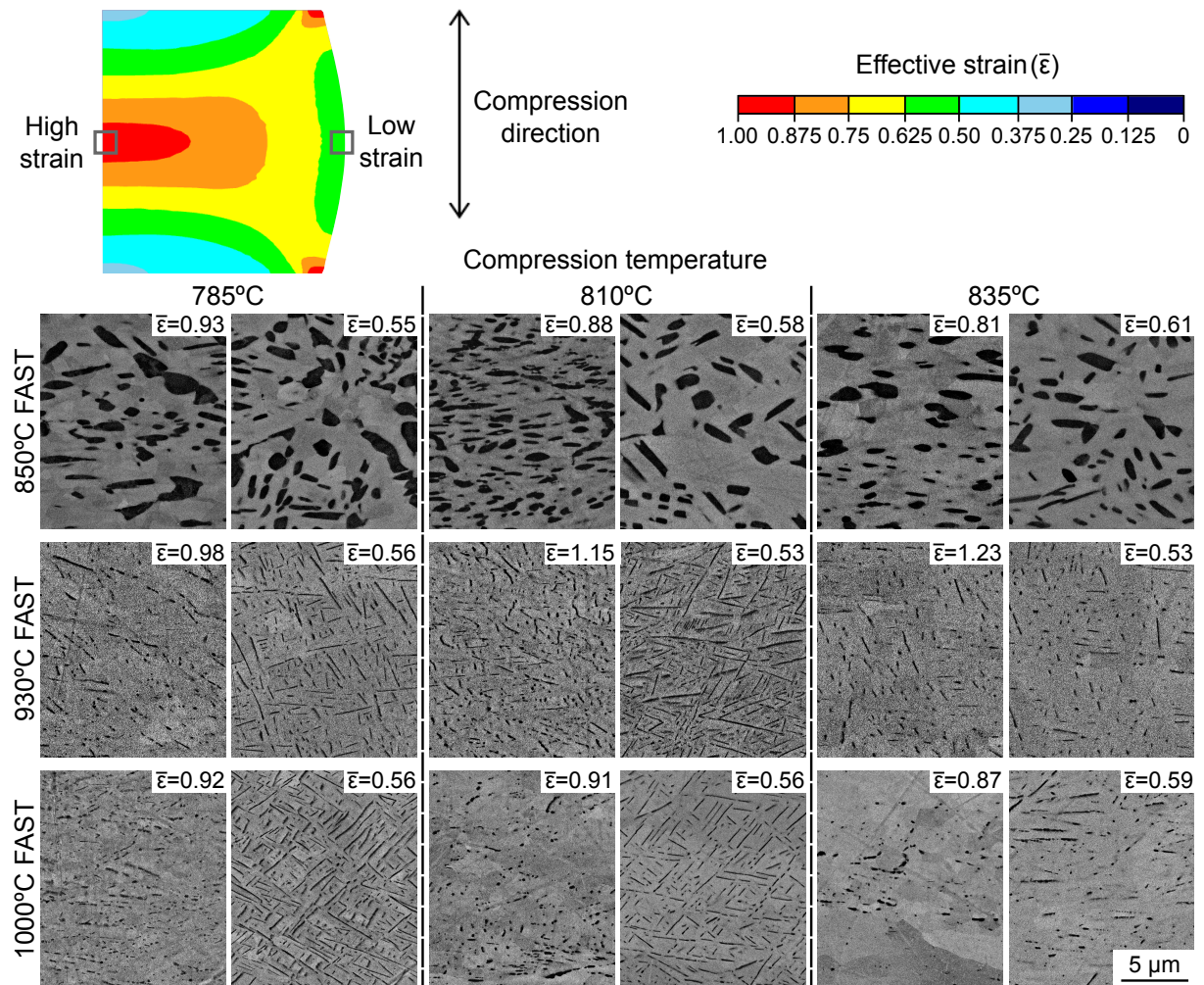


Figure 5.6: BSEI micrographs of the specimens compressed at  $1 \text{ s}^{-1}$  at high strain (centre) and low strain (edge), for all FAST conditions. An example of an FEM simulation, of the specimen produced by FAST at a dwell temperature of  $1000^\circ\text{C}$  and compressed at  $785^\circ\text{C}$  and  $1 \text{ s}^{-1}$ , indicates where the high and low effective strain values were taken from. The compression direction is in line with the page

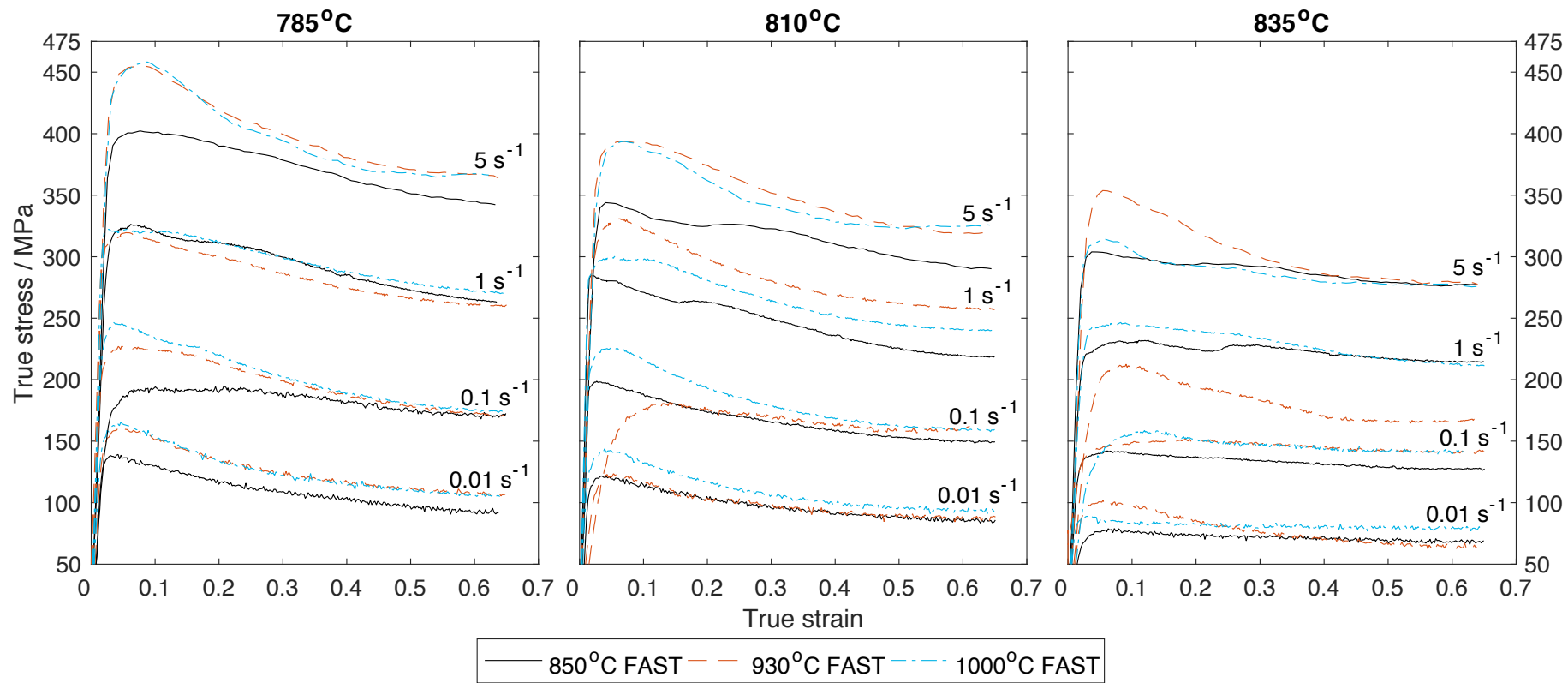


Figure 5.7: Flow curves of FAST specimens produced at 850, 930, and 1000°C, and compressed at temperatures 785, 810, and 835°C and strain rates of 0.01, 0.1, 1, and 5 s<sup>-1</sup>

All FAST conditions produce typical flow stress curve trends: lower forging temperatures and higher strain rates led to an increase in the stress [77].

In general, the amount of flow softening increases as the strain rate increases and the temperature decreases, which is as observed for other  $\beta$  titanium alloys and as found previously for Ti-5553 [76,78]. The flow stress has been corrected for deformation heating, so the flow softening shown in Figure 5.7 is purely as a result of microstructural changes during deformation [79].

However, some of the 930 and 1000°C post-FAST compression specimens were found to have over- or under-heated by more than a few degrees during testing, and as such subsequent isothermal corrections did not fully correct the degree of flow softening: over-heated specimens showed less flow softening and under-heated specimens showed more flow softening, Figure 5.7. The deviation from the test temperature may be due to the thermocouple coming out of the specimen during testing, leading to a loss of contact with the specimen and therefore loss of temperature control.

The 930°C post-FAST specimen compressed at 810°C and  $0.1 \text{ s}^{-1}$ , and the 1000°C post-FAST specimens compressed at 835°C and strain rates 0.01, 0.1, and  $5 \text{ s}^{-1}$  over-heated by 25–65°C, which explains why they show reduced flow softening and low flow stresses at low strains (due to over-heating at the start of the compression test). The 930°C post-FAST specimens compressed at 835°C and strain rates 0.01 and  $1 \text{ s}^{-1}$  under-heated by 30–40°C, which accounts for the increase in flow softening and the higher volume fraction of  $\alpha$  in Figure 5.6 compared to 1000°C (for the  $1 \text{ s}^{-1}$  specimen).

Taking these issues with over- and under-heating into consideration, it can be seen that the flow stress is generally higher for 930 and 1000°C than 850°C post-FAST specimens, and there is generally more flow softening for 930 and 1000°C specimens than 850°C specimens. However, at all temperatures and strain rates there is minimal difference between the flow stress curves of the 930 and 1000°C post-FAST specimens, especially at 785°C where no specimens over- or under-heated.

Following flow softening, the flow stress reaches a constant stress value which remains constant regardless of an increase in strain, and is known as the steady state stress.

There is substantial flow softening at 785 and 810°C for all FAST conditions before the steady state stress is reached, whereas there is very little flow softening or work hardening at 835°C, with the steady state stress reached at low strains. However, at  $\sim 0.6$  strain the steady state flow stress values are very similar for all forging temperatures. The strain rate, therefore, has more of an effect on the steady state stress than the forging temperature.

Overall, there appears to be minimal difference between the flow stress values generated

from material with different FAST conditions. Although the flow stresses at 930 and 1000°C are consistently slightly higher than at 850°C, at forging temperatures of 785 and 810°C the difference in flow stress between 850°C, and 930 and 1000°C reduces as the strain increases to a steady state flow stress ( $\sim 0.6$  strain).

### 5.3.3 Analysis of compressed and heat treated Ti-5553 cone specimens

Four double truncated cones were machined from each of the three FAST specimens: 850, 930, and 1000°C. They were all compressed at 785°C and  $0.1 \text{ s}^{-1}$  and subsequently solution heat treated at 750°C for 2 h. Each was sectioned into two halves and given different ageing temperatures and times: 400°C for 8 h, 500°C for 2 h, 500°C for 4 h, 500°C for 8 h, 600°C for 2 h, and 600°C for 8 h, in order to optimise the heat treatment and thereby the microstructure of Ti-5553 produced by FAST. The cones were analysed using SEM and microhardness.

#### 5.3.3.1 Microstructural evolution and FEM modelling

Figure 5.8 shows the high strain (centre) microstructures of the post-compression specimens (a), and the specimens subsequently solution treated at 785°C for 2 h (b), and aged at 500°C for 4 h (c), for all FAST conditions. Figure 5.8d shows the low strain (edge) microstructures of the specimens aged at 500°C for 4 h, with the corresponding effective strain values generated by FEM simulations. An example of an FEM simulation, for the double truncated cone produced by FAST at 1000°C, is shown to illustrate the distribution of strain during compression testing.

Primary  $\alpha$  grains, which have been deformed perpendicular to the compression direction, can be seen in the microstructure of the 850°C post-FAST and compression specimen, Figure 5.8a. The 930 and 1000°C post-FAST and compression specimens both show broken up and spherodised  $\alpha$  laths. Sub-grains can be observed in Figure 5.8a for all FAST conditions.

Figure 5.8b shows the microstructures of the compressed and solution heat treated specimens, for the 930 and 1000°C FAST conditions. They both contain a high primary  $\alpha$  volume fraction, although it is finer for 1000°C than 930°C.

The microstructures of only one aged condition are shown in Figure 5.8c and d, at high and low strain respectively, due to the similarities between the microstructures of the different ageing conditions. For both the 930 and 1000°C FAST conditions, minimal secondary  $\alpha$  laths were able to precipitate out during ageing, resulting in very similar microstructures for all the solution heat treated and aged specimens. The aged microstructures for the 850°C FAST condition showed slightly more variation than the 930 and 1000°C FAST conditions. However, most contained primary and grain boundary  $\alpha$  interspersed with finer secondary  $\alpha$  laths, as shown in Figure 5.8c and d, demonstrating the more typical bi-modal microstructure desired from the solution heat treatment and ageing of Ti-5553 [22].

When the high and low strain microstructures in Figure 5.8c and d are compared, it can be seen that similar microstructures were produced for the 850°C FAST condition, only on a smaller scale for high strain. For the 930 and 1000°C FAST conditions, the  $\alpha$  is more spherodised



and broken up at high strain, whereas it is still very lath-like at low strain.

#### *5.3.3.2 Microhardness*

Figure 5.9 shows the microhardness of the post-FAST, post-compression, post-solution heat treatment (ST), and post-aged conditions, for FAST temperatures of 850, 930, and 1000°C.

The 930 and 1000°C specimens in post-FAST and post-compression conditions are very similar; however, slight variations between them are found following solution heat treatment and ageing. The 850°C specimens have microhardness values consistently lower than those of the 930 and 1000°C specimens at all conditions.

For all FAST conditions, the microhardness reduces upon compression, then increases upon solution treatment, and increases further still upon ageing.

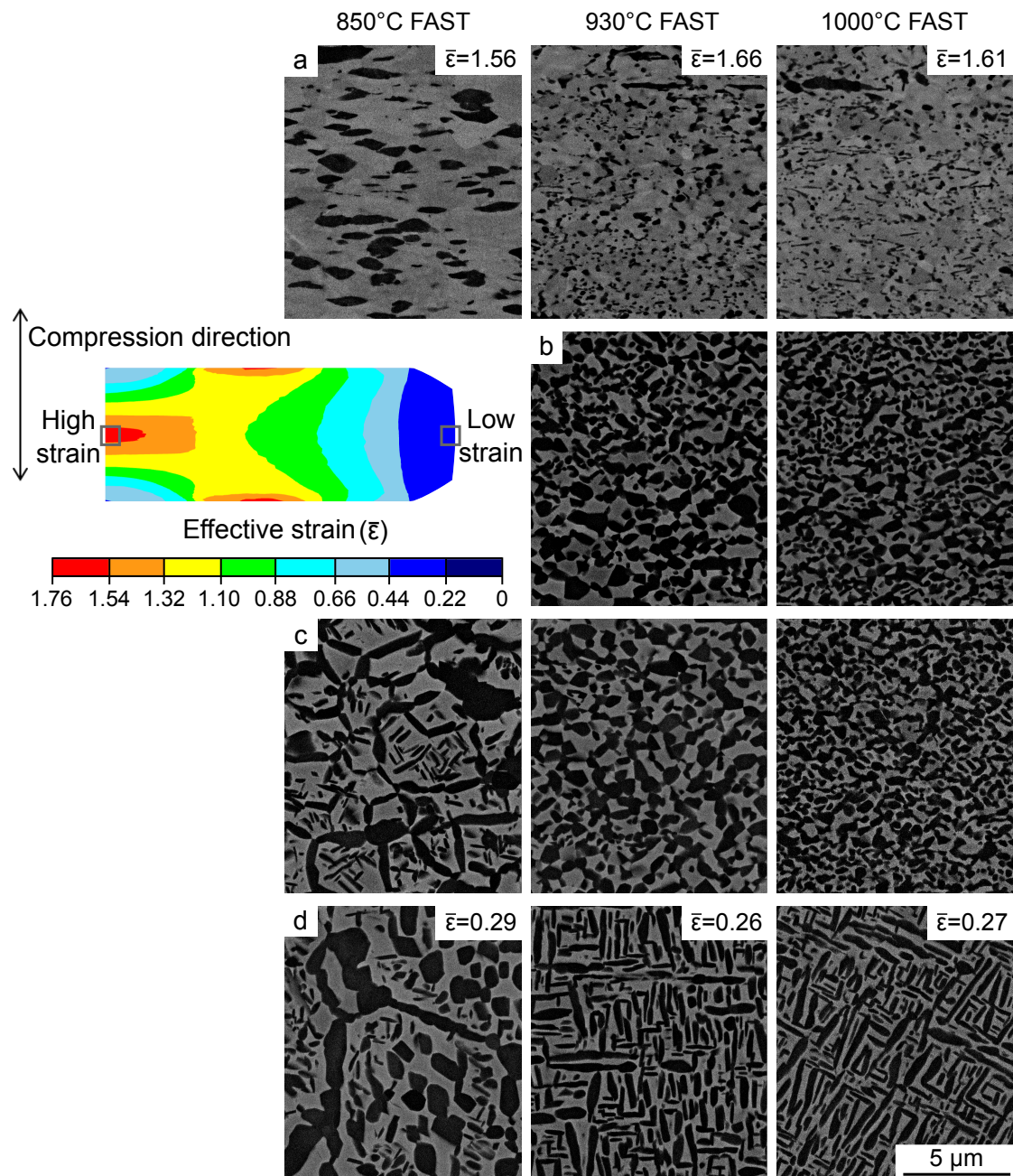


Figure 5.8: Selected BSEI micrographs of the double truncated cones which have been (a) compressed at 785°C and  $0.1 \text{ s}^{-1}$  at high strain (centre), (b) subsequently solution heat treated, and (c) and (d) aged at 500°C for 4 h at high strain (centre) and low strain (edge), respectively, for all FAST conditions. An example of an FEM simulation, of the specimen produced by FAST at a dwell temperature of 1000°C, indicates where the high and low effective strain values were taken from. The compression direction is in line with the page

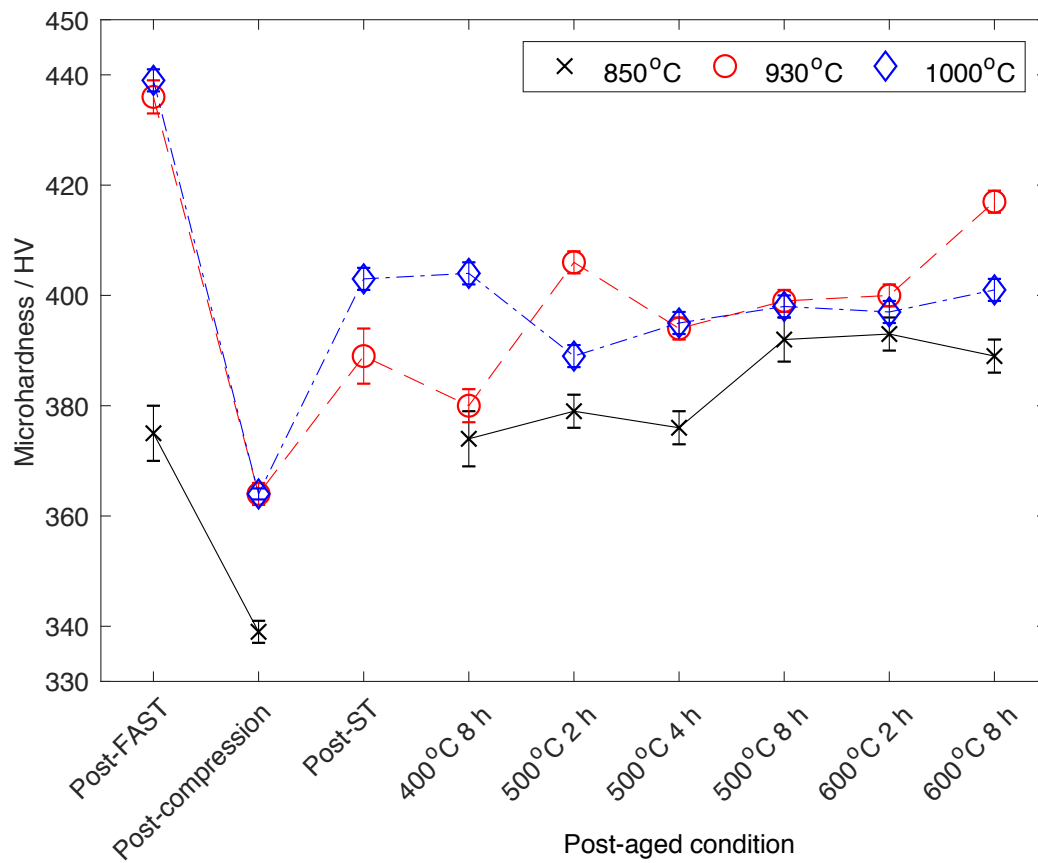


Figure 5.9: Microhardness of Ti-5553 in the post-FAST, post-compression, post-solution heat treatment (ST), and post-aged conditions. All heat treatment conditions were performed following compression of the post-FAST cones (at 785°C and 0.1 s<sup>-1</sup>), and all ageing conditions were performed following the same solution heat treatment (785°C for 2 h)

### 5.3.4 Analysis of large-scale forged and heat treated Ti-5553 specimens

The fourth FAST specimen, produced at 1000°C, was machined to produce three double truncated cones which were forged at 785, 810, and 835°C at  $\sim 3 \text{ s}^{-1}$ . Half of each forged specimen was solution heat treated at a proprietary temperature between 750 and 850°C for 4 h, and aged for 8 h at a propriety temperature below 650°C, in order to replicate the conventional industrial processing of Ti-5553. Analysis on the forged and heat treated specimens includes SEM, microhardness, TEM, and FEM.

#### 5.3.4.1 Microstructural evolution and FEM modelling

Figure 5.10 shows the microstructure produced by industrial forging at 785°C of a 1000°C post-FAST double truncated cone from high (1) to low (7) strain, and subsequent industrial heat treatment. Flow data generated in Section 5.3.2 was used to produce an FEM simulation of the 785°C forged specimen, shown in Figure 5.10, to illustrate the distribution of strain during forging.

The forged micrographs in Figure 5.10 (1–7) indicate that the acicular secondary  $\alpha$  laths present have been broken up and spherodised at high strain (centre), but are relatively undeformed at lower strain (edge). It can also be seen that the volume fraction of  $\alpha$  phase present is lower at higher strain (2) than at lower strain (7), due to partial dissolution of the  $\alpha$  phase during forging by localised deformation heating.

Conversely, there is minimal microstructural dependency on the amount of strain in the heat treated microstructures, with the only difference being the directionality of the primary  $\alpha$  grains which are perpendicular to the direction of forging at high strain. Very different microstructures at the centre and the edge of the forged cone are very similar following heat treatment.



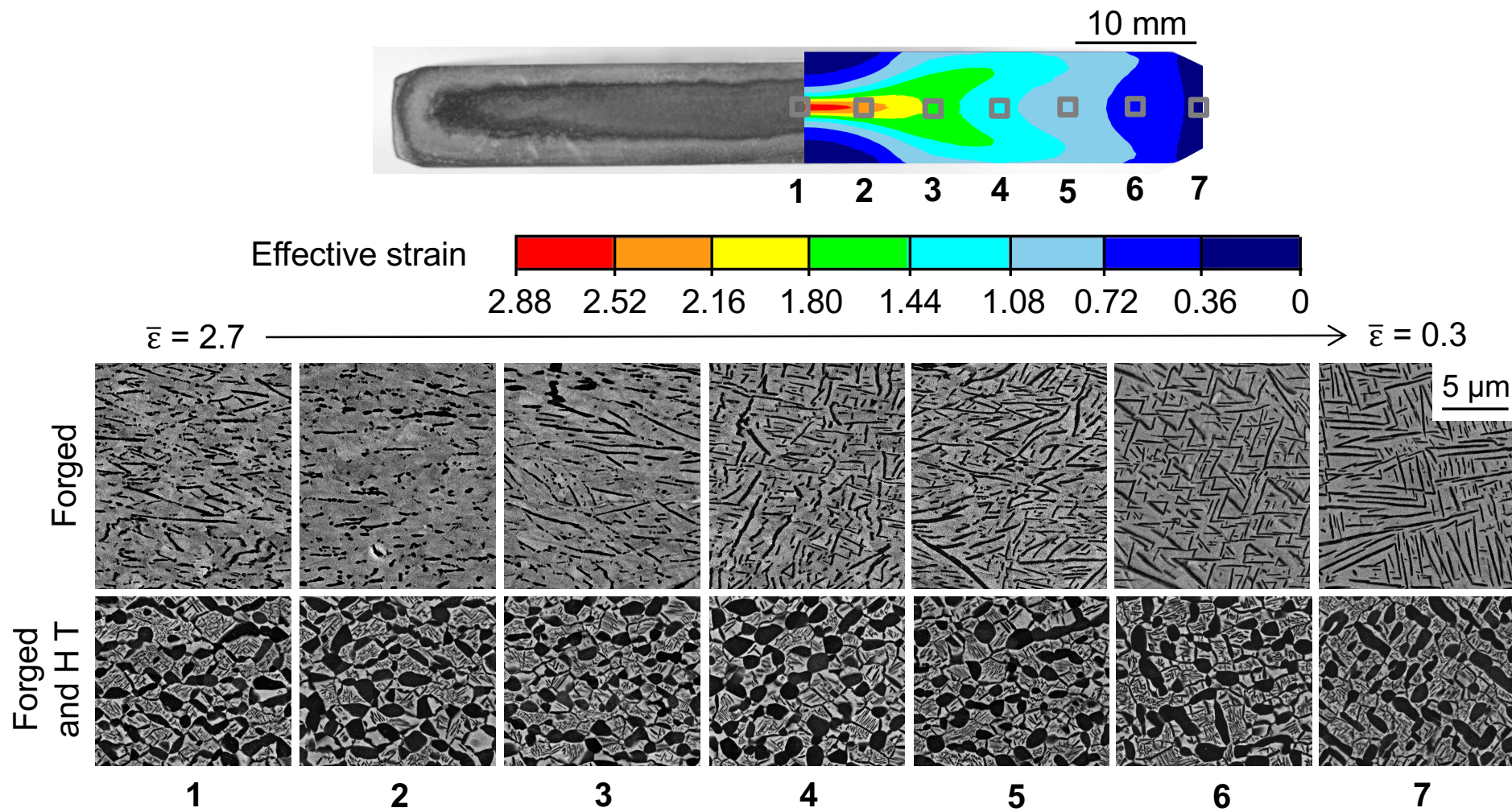


Figure 5.10: BSEI micrographs of the double truncated cone forged at 785°C, and heat treated between 750 and 850°C for 4 h and below 650°C for 8 h (HT). Micrographs were taken from the centre (high strain) to the edge (low strain) of the forged and heat treated specimens. The FEM simulation indicates the strain distribution within the forged specimen. The forging direction is in line with the page

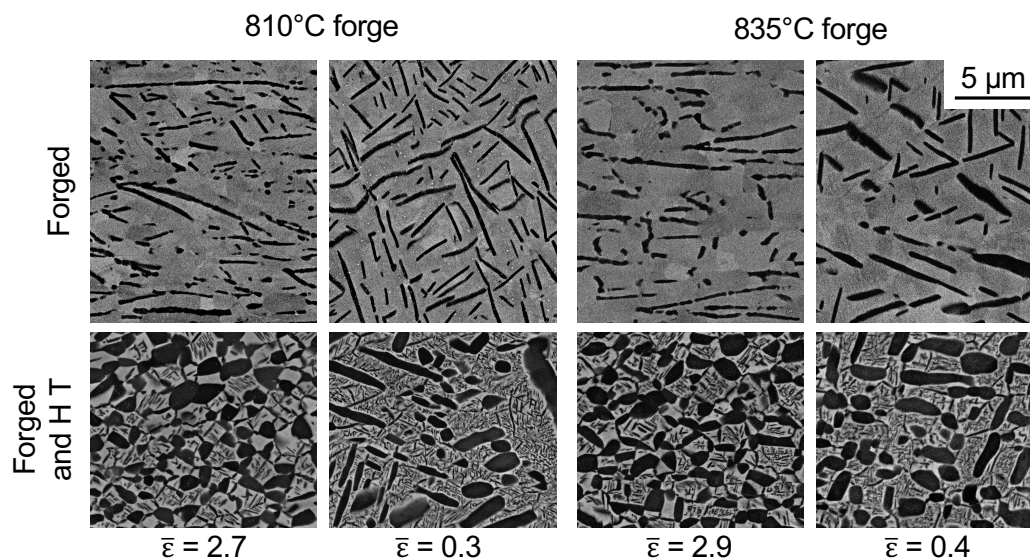


Figure 5.11: BSEI micrographs of double truncated cones forged at 810 and 835°C, and heat treated between 750 and 850°C for 4 h and below 650°C for 8 h (HT). Micrographs were taken from the centre (high strain) and the edge (low strain) only. The forging direction is in line with the page

Figure 5.11 shows the microstructures of the double truncated cones forged at 810 and 835°C and heat treated, at high and low strain only. The microstructure at the high strain regions of the forged specimens shows the break-up and spheroidisation of  $\alpha$  laths, whereas there is minimal break-up in the low strain regions. The volume fraction of  $\alpha$  phase is lower at high strain than at low strain for both forging temperatures.

An increase in the forging temperature is shown to coarsen the secondary  $\alpha$  in the forged microstructures, due to increased diffusion at higher temperatures allowing preferential growth of some of the secondary  $\alpha$  laths.

There is also clear indication in Figure 5.10 and 5.11 of the presence of  $\beta$  sub-grains, especially in the high strain forged microstructures.

For all forging temperatures, the heat treated microstructures show minimal microstructural dependency on the forging temperature, and only some dependence on the strain.

#### 5.3.4.2 Microhardness of solution heat treated and aged specimens

Figure 5.12 shows the microhardness variation from centre to edge of the heat treated specimens forged at 785, 810, and 835°C.

There is minimal variation in microhardness from centre to edge for all three specimens, which indicates that strain has minimal effect on the microhardness.

The average microhardness values were 416 HV for the specimen forged at 785°C, 410 HV for 810°C, and 417 HV for 835°C, indicated by the blue horizontal lines. This illustrates that different forging temperatures also have minimal effect on the microhardness values.

#### 5.3.4.3 Transmission electron micrographs

A comparison between the high and low strain microstructures of the heat treated specimen forged at 810°C was made to determine if there were differences at a higher resolution than could be achieved by SEM, Figure 5.13.

Figure 5.13a and b are micrographs taken from similar regions using transmission and scanning electron microscopy, respectively.

There is minimal difference in the microstructures at high and low strain in Figure 5.13a and b: both show primary  $\alpha$  grains surrounded by a  $\beta$  matrix, which contains secondary  $\alpha$  laths. However, in Figure 5.13b the primary  $\alpha$  grains are slightly more aligned to the perpendicular of the forging direction at high strain than low strain. Some sub-boundaries in the  $\alpha$  phase can be seen in Figure 5.13a for high strain, which is indicative of the globularisation process which occurs with increased deformation [76].

Figure 5.13c captures the high and low strain microstructures at higher resolution than in Figure 5.13a, in order to show the secondary  $\alpha$  morphology. At high strain the  $\alpha$  appears coarser than at low strain, which is corroborated by Figure 5.13b.

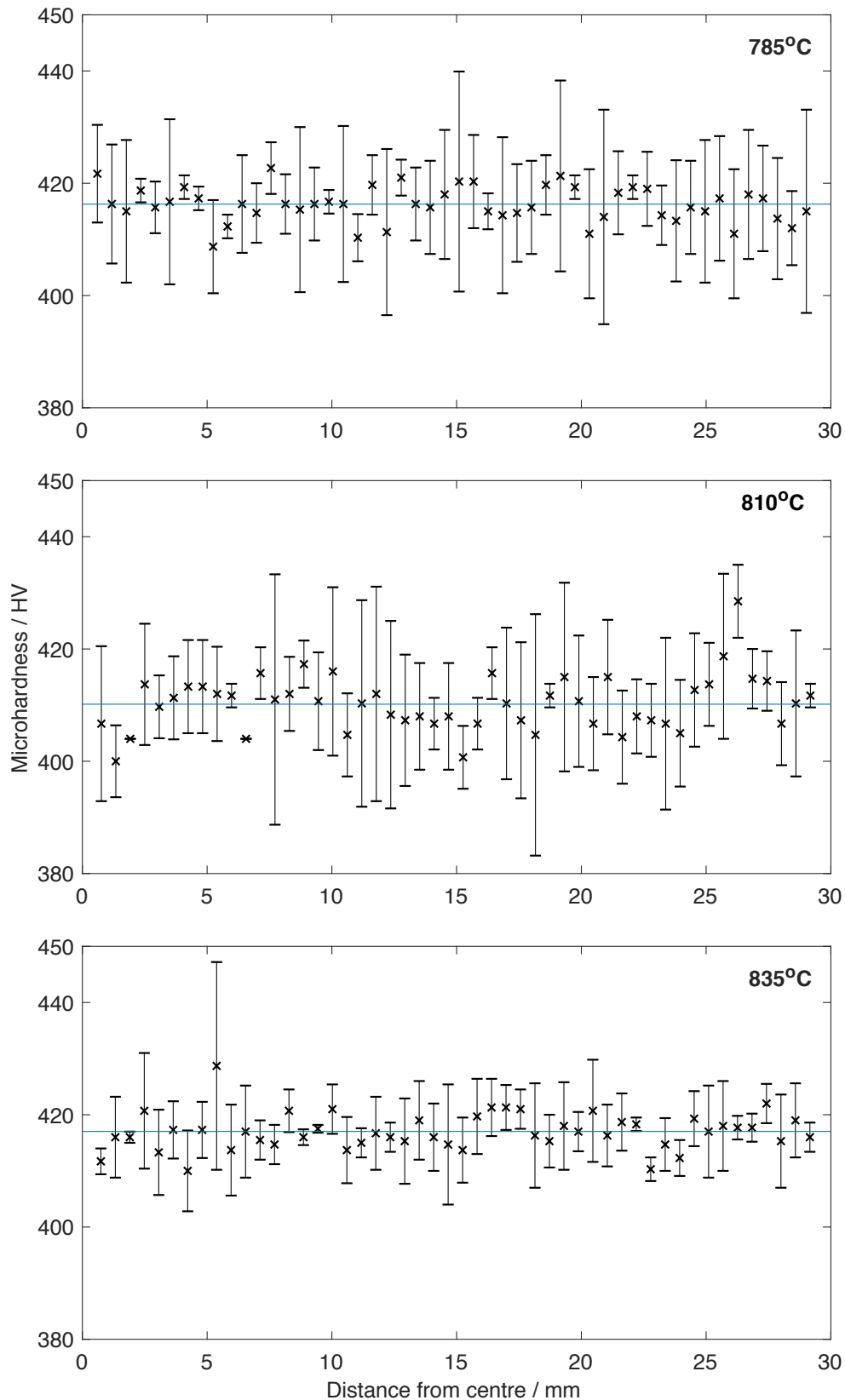


Figure 5.12: Microhardness variation from the centre (0 mm) to the edge (30 mm) of the heat treated specimens forged at 785, 810, and 835°C, with the average of all the microhardness values indicated by the horizontal lines. The microstructure corresponding to the microhardness values is shown in Figures 5.10 and 5.11. A vickers indenter with 4.905 N load was used



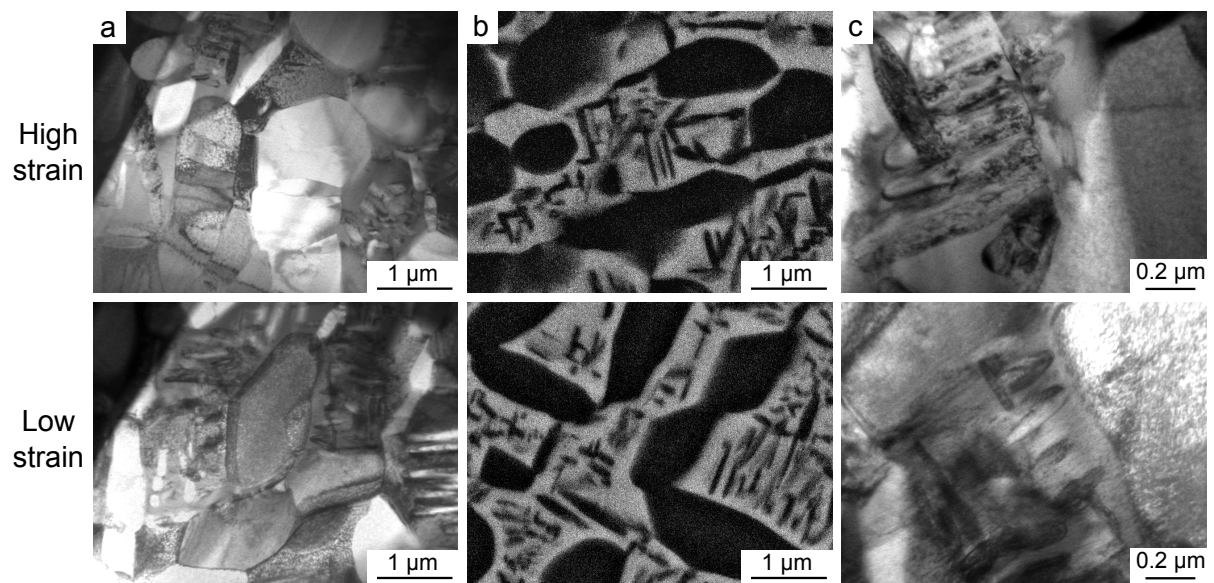


Figure 5.13: High and low strain microstructures of the heat treated specimen forged at 810°C when imaged by: (a) and (c) transmission electron microscopy (bright field), and (b) BSEI. The forging direction is in line with the page for (b) only

## 5.4 Discussion

### 5.4.1 Comparison between post-FAST, post-compression, and forged microstructures

In Figure 5.4, the comparison of the post-FAST material to the initial powder shows that minimal  $\beta$  grain growth has occurred during the 30 min dwell time at temperature. This ability to maintain fine grain size is one of the reasons FAST was preferred to conventional sintering methods for consolidation of Ti-5553. The  $\beta$  grain size produced by FAST is less than 200  $\mu\text{m}$  at a dwell temperature of 1000°C. However, conventionally produced Ti-5553 solution heat treated at 925°C produced a much larger grain size of approximately 700  $\mu\text{m}$  [35].

Both 1000°C post-FAST specimens were included in Figure 5.4 to illustrate the ability of the FAST process to produce consistent, controlled microstructures. The microstructures were also similar for 930 and 1000°C, although slight differences could be observed at higher resolution in the transmission electron micrographs in Figure 5.5. Increased diffusion at the higher FAST temperature led to coarser  $\alpha$  laths at 1000°C than at 930°C. The similarities between the 930°C and both 1000°C post-FAST microstructures are corroborated by the microhardness results, which were very similar for all conditions, Figure 5.9.

The acicular secondary  $\alpha$  morphology shown in Figure 5.4 at 1000°C was very similar to that of conventionally processed Ti-5553 which has been furnace cooled from above the  $\beta$  transus temperature [26]. It is also very similar to that of  $\beta$  forged material, which Jones et al. characterise as having a continuous  $\alpha$  layer at the prior  $\beta$  grain boundary and fine Widmanstätten secondary  $\alpha$  in the centre of the  $\beta$  grains [80]. Such conventional material would have gone through more than thirty heating and forging steps to obtain this microstructure.

The post-compression microstructures shown in Figure 5.6 can be compared to the post-FAST microstructures in Figure 5.4 (of the same scale). The 850°C post-compressed material shows break-up of the grain boundary  $\alpha$ , an increase in the primary  $\alpha$  size, and some spheroidisation of the  $\alpha$  grains, although some  $\alpha$  has dissolved due to time spent at the compression temperature. The 930 and 1000°C post-FAST material also shows break-up of the grain boundary  $\alpha$ , and growth of the secondary  $\alpha$  laths. These changes are because of both the deformation and the time spent at temperature during compression.

The forged microstructures shown in Figure 5.10 can also be compared to the microstructures of the 1000°C post-FAST material in Figure 5.4 (of the same scale). As with compression testing, large-scale forging has broken up the grain boundary  $\alpha$  which was present post-FAST, and has allowed the secondary  $\alpha$  laths to grow.

### 5.4.2 Cylindrical compression testing study

The flow curves in Figure 5.7, generated for material produced by FAST, can be compared to those of conventionally produced Ti-5553 in Figures 2.9 and 2.10 in the  $\beta$  forged and  $\alpha + \beta$  conditions, respectively [26, 37].

The peak stress values, steady state values, and the degree of flow softening of material produced by FAST at 930 and 1000°C are very similar to those of the  $\beta$  forged condition, which has a comparable microstructure prior to compression (Figure 2.9).

The peak stress values of material produced by FAST at 850°C are consistently higher than those of the  $\alpha + \beta$  condition, which has similar microstructures prior to and following compression (Figure 2.10) [26]. There is also more flow softening in the 850°C FAST material than in the  $\alpha + \beta$  conventional material, although they reach similar steady state values at  $\sim 0.6$  strain, indicating that they behave in the same way once the  $\alpha$  phase has been deformed. The differences in flow behaviour between the 850°C FAST and  $\alpha + \beta$  material may be caused by differences between their starting microstructures. At 850°C, the post-FAST material has primary  $\alpha$  grains as well as grain boundary  $\alpha$  at the prior powder particle boundaries, Figure 5.4a, whereas the  $\alpha + \beta$  material only has primary  $\alpha$  grains [26]. This will cause the 850°C FAST material to have higher peak stress values and greater flow softening as the grain boundary  $\alpha$  is broken up.

The comparable flow curves of the material produced by FAST at 930 and 1000°C and the  $\beta$  forged conventionally produced Ti-5553 is highly significant, as it indicates that material processed in two steps by the FAST-*forge* process behaves in a similar manner to Ti-5553 which has been through the Kroll extraction method, VAR, and multiple thermomechanical processes.

The flow curves shown in Figure 5.7 for the compression testing study can be linked to the microstructures produced, shown in Figure 5.6. It should be noted that the flow stress curves have been corrected for deformation heating, whereas the microstructures have not. They therefore show both the effect of the microstructural changes and deformation heating. The microstructural changes shown in Figure 5.6, between the low and high strain microstructures, occur primarily in the  $\alpha$  phase. Material produced by FAST at 850°C has globularised primary  $\alpha$  grains prior to compression (as shown in the low strain microstructures), whereas material produced at 930 and 1000°C has fine acicular secondary  $\alpha$  with a high aspect ratio.

Humphreys and Hatherly have described the formation of dislocations in a  $\beta$  phase matrix surrounding  $\alpha$  particles, due to local strain incompatibility (if the  $\alpha$  phase particles are much harder than the  $\beta$  matrix) [81]. Weiss and Semiatin have confirmed the relevance of this phenomenon for  $\beta$  titanium alloys; as the much higher hardness of the  $\alpha$  phase in titanium compared to the  $\beta$  phase leads to reduced deformation, and therefore to strain concentration

build-up in the  $\beta$  phase surrounding the  $\alpha$  particles [76]. This causes high misorientation sub-grains to form in the  $\beta$  matrix phase surrounding  $\alpha$  particles. For the globularised  $\alpha$  present in the material produced by FAST at 850°C, this is the case, as it does not significantly impede dislocation movement. Consequently it is elongated perpendicular to the direction of deformation rather than broken up, as shown in Figures 5.6 and 5.8a, and as described by Weiss and Semiatin [76].

However, for higher strains or for  $\alpha$  phase particles with a higher aspect ratio (acicular  $\alpha$ ) as for 930 and 1000°C, Weiss and Semiatin describe that the strain build-up leads to sub-boundary formation in the  $\alpha$  phase because of increased dislocation pile-up at the  $\alpha/\beta$  interfaces [76]. This is demonstrated in the heat treated microstructure in Figure 5.13a at high strain. The  $\beta$  phase penetrates along the  $\alpha/\alpha$  sub-boundaries, breaking up the acicular  $\alpha$  into more equiaxed grains, which is known as globularisation. This is shown by Hua et al. for conventionally produced Ti-5553, and in Figures 5.6 and 5.8a for the Ti-5553 produced by FAST at 930 and 1000°C [82].

Jones and Jackson have also discussed the ability of the acicular  $\alpha$  in Ti-5553 to impede dislocation movement, and cause dislocation pile up at the  $\alpha/\beta$  interfaces [78]. As a result, a high peak flow stress is reached initially at low strain during deformation, followed by a reduction in flow stress with increasing strain, due to the break-up and globularisation of the  $\alpha$  particles (as they no longer impede dislocations). This is known as flow softening and results in the characteristic flow softening curve shape shown in Figure 5.7 for material produced by FAST at 930 and 1000°C, and for conventionally produced Ti-5553 [78].

Verlinden et al. have described the effect of sub-grain formation on the flow stress during hot deformation [83]. Sub-grain boundaries are made up of dislocations: during deformation, free dislocations are produced by increased strain and are annihilated by their interaction with dislocations of the opposite sign in the sub-grain boundary (through cross-slip and climb). This process of dynamic recovery limits the accumulation of dislocations, so that the flow stress remains at a constant value despite an increase in strain (known as the steady state stress). Consequently, the steady state stresses reached in the flow stress curves in Figure 5.7 are due to dynamic recovery within the  $\beta$  phase.

In Figure 5.7, the flow stress is shown to be generally slightly higher for material produced by FAST at 930 and 1000°C than 850°C. However, this difference tends to reduce as strain increases for compression temperatures 785 and 810°C, which suggests that it is because of the increased hardness provided by the acicular  $\alpha$  at 930 and 1000°C at low strain. Due to the break-up of acicular secondary  $\alpha$  at 930 and 1000°C, and deformation of primary  $\alpha$  grains at 850°C during compression, the difference between the stress at 850°C, and 930 and 1000°C

reduces, and the flow stress behaviour is controlled by the predominant  $\beta$  phase at steady state stress for all FAST conditions (as the  $\alpha$  phase volume fraction present for all conditions is relatively low) [78]. There is no clear or consistent difference between the flow stress curves of the material produced by FAST at 930 and 1000°C, which is likely as a result of the very similar post-FAST microstructures, shown in Figure 5.4.

Aside from the flow softening behaviour of the acicular  $\alpha$  phase at 930 and 1000°C, the primary and secondary  $\alpha$  particles merely act like hard inclusions in a soft  $\beta$  matrix [24]. This indicates that there is a large processing window for the FAST process to produce pre-forged Ti-5553 billet, as the flow data is consistent regardless of the post-FAST microstructure.

The flow curves in Figure 5.7 produced at a compression temperature of 835°C reach a steady state stress at a lower strain than the other compression temperatures, and they exhibit minimal flow softening or work hardening. This is due to a lower primary and secondary  $\alpha$  volume fraction present at a compression temperature of 835°C, as shown in the microstructures in Figure 5.6 for a strain rate of 1 s<sup>-1</sup>. During compression the  $\alpha$  phase is partially dissolved owing to deformation heating during compression, which raises the local temperature to close to the  $\beta$  transus ( $\sim$ 890°C).

### 5.4.3 Cone compression testing and heat treatment study

In Figure 5.9 the large difference in microhardness between the specimens produced by FAST at 850°C, and 930 and 1000°C is due to the very fine secondary  $\alpha$  present at 930 and 1000°C, Figure 5.4, which impedes dislocation movement and thereby increases the microhardness (as discussed in Section 5.4.2).

All FAST conditions show a decrease in microhardness following compression testing, Figure 5.9. This is as a result of the change in microstructure from the post-FAST in Figure 5.4d to that of Figure 5.8a following compression. The high strength fine-scale  $\alpha$  laths in the 930 and 1000°C post-FAST specimens have been broken up and spherodised, and have grown owing to diffusion at high temperature. They therefore offer less resistance to deformation and thus reduced microhardness values. The primary  $\alpha$  present in the 850°C post-FAST specimen has also spherodised and has grown due to diffusion at high temperature, although to a lesser extent than for 930 and 1000°C, which resulted in a smaller reduction in microhardness.

Following solution heat treatment, there is a slight difference in microhardness between the material produced by FAST at 930 and at 1000°C. This may be due to the presence of finer individual  $\alpha$  grains along with a larger volume fraction of  $\alpha$  phase in the 1000°C specimen, shown in Figure 5.8b, which is harder than the  $\beta$  phase. In general the differences in microhardness

between the material produced by FAST at 930 and at 1000°C, for the aged conditions, correspond to slight differences in the microstructure: finer primary  $\alpha$  grains and a larger overall  $\alpha$  phase volume fraction produce a small increase in the microhardness.

Minimal secondary  $\alpha$  laths were present following ageing, Figure 5.8c, as would be expected [22], due to the high volume fraction of primary  $\alpha$  produced during solution heat treatment. This may have been caused by the solution heat treatment temperature, duration, or the cooling rate (which was very slow) [22]. As the secondary  $\alpha$  provides a substantial strengthening effect, this implies that the microhardness values could be even higher if the secondary  $\alpha$  could precipitate out, should the solution heat treatment be optimised.

The material produced by FAST at 850°C showed consistently lower microhardness values than those of 930 and 1000°C for all ageing conditions. These small differences may be as a result of the larger  $\alpha$  grains produced at 850°C, Figure 5.8c, which leave adjacent  $\alpha$ -depleted regions of  $\beta$  phase which are softer than the  $\alpha$  phase. This also accounts for the larger degree of error in the measurements for 850°C compared with 930 and 1000°C, Figure 5.9.

#### 5.4.4 Large-scale forging and heat treatment study

As with the compression testing study, the volume fraction of secondary  $\alpha$  at high strain is lower than at low strain, due to partial dissolution of the  $\alpha$  phase during forging. Again, this may be due to deformation heating increasing the local temperature to close to the  $\beta$  transus,  $\sim 890^\circ\text{C}$ , and allowing the  $\alpha$  to dissolve, as the cone was forged at a high strain rate of  $\sim 3\text{ s}^{-1}$ .

As previously described, secondary  $\alpha$  laths form small globularised  $\alpha$  particles when they are broken up during forging, as shown in Figures 5.10 and 5.11 for the high strain microstructures. As with the compression testing study, this behaviour is comparable to that of secondary  $\alpha$  in forged conventionally produced Ti-5553 [78].

High mis-orientation sub-grains are formed within the  $\beta$  phase, which can be seen more easily for the large-scale forging in Figures 5.10 and 5.11 than for the smaller-scale compression in Figure 5.6, due to increased strain at the large-scale. They can also be seen clearly in Figure 5.8a for all FAST conditions, and a comparison between the compressed and heat treated microstructures in Figure 5.8a, b, and c shows that grain boundary  $\alpha$  has formed along the prior  $\beta$  sub-grain boundaries.

In Figures 5.10 and 5.11, an increase in the forging temperature is shown to coarsen the secondary  $\alpha$  in the forged microstructures, due to increased diffusion at higher temperatures allowing preferential growth of some of the secondary  $\alpha$  laths.

Both figures show that there is minimal microstructural dependency on the forging tem-

perature and only some dependency on the strain in the heat treated microstructures, which is a major advantage over conventionally produced Ti-5553. This is confirmed in Figure 5.12 by the microhardness values, as they vary only slightly with differing forging temperatures and amounts of strain. It should be noted, however, that the microhardness indents are  $\sim 1000 \mu\text{m}^2$ , which is much larger than the microstructural features shown in Figures 5.10 and 5.11, and results in an average macroscopic microhardness value that is relatively independent of the microstructural differences seen in the micrographs for low and high strain.

The transmission electron micrographs in Figure 5.13, at higher resolution than in Figure 5.10, show only minimal differences between the high and low strain microstructures. At high strain the  $\alpha$  appears coarser than at low strain, possibly due to increased diffusion caused by deformation heating. There is also evidence of sub-grain formation in the  $\alpha$  phase at high strain, likely owing to increased deformation and dislocation pile up at  $\alpha/\beta$  interfaces [76].

Conventionally produced Ti-5553, which has been heat treated using the same temperatures and durations, and has also been provided by Safran Landing Systems, produced microhardness values of between 385 and 405 HV [84]. These values are lower than those produced by heat treatment of FAST-*forged* material, between 410 and 417 HV, which shows that the FAST-*forge* processing route is capable of producing enhanced mechanical properties compared to the conventional route, in fewer processing steps.

It is interesting to note that the heat treated microhardness values of between 410 and 417 HV are lower than that of the post-FAST material, 446 HV. This is likely to be caused by the very fine secondary  $\alpha$  present in the material produced by FAST (Figure 5.4), which is much coarser once forged and heat treated (Figures 5.10 and 5.11). The very fine secondary  $\alpha$  provides more resistance to deformation, as discussed in Section 5.4.2, and therefore increases the microhardness.

#### 5.4.5 Powder to heat treated Ti-5553 billet in three steps

Figure 5.14 illustrates the production of a heat treated Ti-5553 billet from powder in three steps by the FAST-*forge* process: FAST consolidation of the powder, forging of the machined double truncated cone, and heat treatment of the forged cone.

Inset, top right, in the figure is an example of a heat treated Ti-5553 microstructure produced by the conventional processing route. The heat treated microstructures produced in this study are not ideal when compared with this microstructure; however, they can easily be tailored to be comparable with conventionally produced material once the heat treatment regime has been optimised.

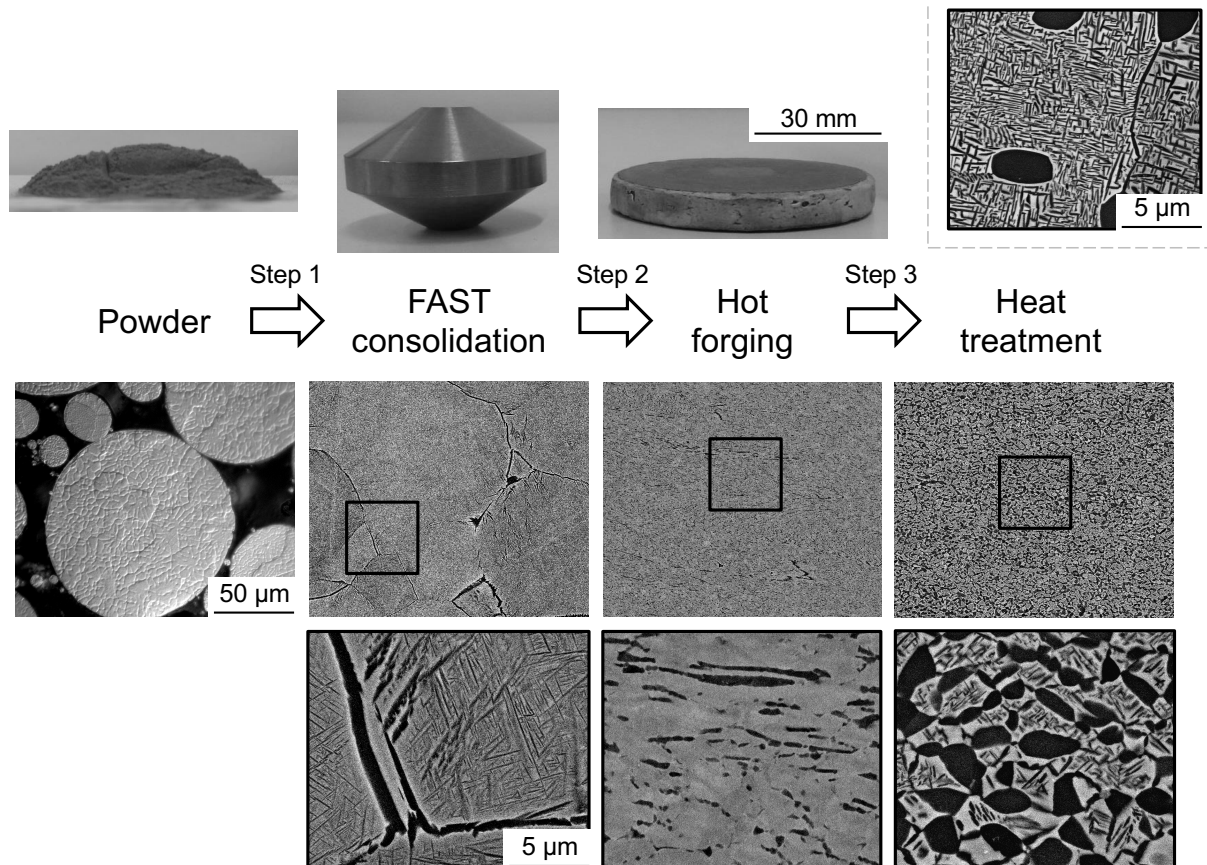


Figure 5.14: Flow chart illustrating the FAST-*forge* process: from powder to heat treated specimen in three steps. BSEI micrographs of post-FAST, forged, and heat treated specimens are shown, with a light micrograph of gas atomised Ti-5553 powder, and photographs of the powder, a machined post-FAST double truncated cone, and a forged cone. FAST and forging directions are in line with the page. A BSEI micrograph of conventionally produced Ti-5553, which has been heat treated using the same temperatures and durations, is shown inside the dashed lines for comparison



This large-scale forging study has proved that the FAST-*forg*e process can be scaled up from the small-scale compression testing study to the industrial scale. The simplicity of the process could eliminate the risk of producing a forging with a variation of properties in different areas, as has been shown to occur for the conventional processing route for Ti-5553, due to preceding processing steps [84].

## 5.5 Conclusions

1. Close to fully dense Ti-5553 billets have been successfully produced by FAST on an industrial-scale. The microstructure produced was very similar to that of conventionally  $\beta$  forged Ti-5553, for material processed above the  $\beta$  transus (930 and 1000°C). This microstructure showed no indication of the prior powder structure once it had been processed by FAST, and has retained the fine  $\beta$  grain size of the powder.
2. The compression testing study of the post-FAST material (930 and 1000°C) has produced flow curves which are very similar to those of conventionally produced  $\beta$  forged Ti-5553. The flow curves are relatively consistent despite different FAST temperatures of 850, 930 and 1000°C. The main difference between the flow curves of 850°C, and 930 and 1000°C post-FAST specimens is the degree of flow softening during compression testing. For 930 and 1000°C specimens, the starting acicular  $\alpha$  microstructure was broken up and spheroidised as strain increased, leading to extensive flow softening, whereas at 850°C the primary  $\alpha$  grains showed only slight deformation perpendicular to the compression direction.
3. Double truncated cones were also compressed at a single temperature and strain rate to conduct a heat treatment study, with the cone providing a large variation in strain from centre to edge. Various temperatures (400–600°C) and durations (2–8 h) were used to determine the effect on the microstructure. However, due to the solution heat treatment producing a large volume fraction of primary  $\alpha$  in the specimens produced by FAST at 930 and 1000°C, minimal secondary  $\alpha$  was able to precipitate out during ageing, leading to very similar microhardness results. The specimen produced by FAST at 850°C was able to precipitate out some secondary  $\alpha$ , which gave rise to a more typical Ti-5553 solution treated and aged microstructure.
4. Large-scale industrial forging and heat treatment of Ti-5553 produced by FAST has produced microstructures similar to those of conventionally produced Ti-5553, despite taking only three processing steps (far fewer than for the conventional process shown in Figure 1.1), as shown in Figure 5.14.
5. The forged microstructures of specimens produced by FAST were shown to vary with forging temperature and level of strain, whereas only slight variations were seen in the heat treated microstructure, even at higher resolution in TEM. Microhardness measurements of the heat treated specimens showed similar results, with different forging temperatures and

levels of strain having minimal effect on the microhardness values: averages of 410–417 HV were found for different forging temperatures. These have been shown to be higher than that of conventionally produced material which has undergone the same heat treatment. It is important to note that there is also no indication in the material flow curves or microhardness data that the heat treated material originated from powder rather than conventional billet.

6. FAST-*forg*e is capable of producing forged and heat treated Ti-5553 microstructures, microhardness values, and flow behaviour similar to that of conventional processing, while significantly reducing the number of processing steps. Scale up of the process has proven that it is applicable on an industrial scale for a high strength metastable  $\beta$  titanium alloy.

## Chapter 6

# Microstructural prediction model and complex Ti-5553 forging

### 6.1 Outline

This chapter presents a microstructural prediction model for the Ti-5553 compressed in Chapter 5, for specimens produced by FAST at 930 and 1000°C (i.e. above the  $\beta$  transus temperature). This microstructural prediction model was used to estimate the temperature and strain rate during drop forging of a complex geometry of Ti-5553 produced by FAST. This component was produced in order to demonstrate the ability of the FAST-*forge* process to produce a complex Ti-5553 forging for, e.g., the aerospace sector.

A literature review and experimental procedure which is specific to the microstructural prediction model and complex forging is included. The literature review should be used in conjunction with the literature review in Chapter 2.

## 6.2 Literature review

The key factors of flow stress during plastic deformation processes like forging are the temperature and strain rate. These conditions can be grouped together by the temperature-compensated strain rate developed by Zener and Hollomon [85, 86]. The Zener-Hollomon parameter,  $Z$ , is shown in Eq. 6.1 where  $\dot{\epsilon}$  is the strain rate,  $Q_{def}$  is the activation energy of deformation,  $R$  is the ideal gas constant, and  $T$  is the temperature in K.

$$Z = \dot{\epsilon} \exp \left( \frac{Q_{def}}{RT} \right) \quad (6.1)$$

Various constitutive equations for hot working have been developed to relate the Zener-Hollomon parameter to the flow stress, with the equation developed by Sellars and Tegart being the most commonly used of these, as it is valid for a wide range of stresses, strain rates, and temperatures [86]. The Sellars-Tegart equation, Eq. 6.2, allows the stress to be predicted for a given strain at various strain rates and temperatures (where  $A$ ,  $\delta$ , and  $n$  are temperature-independent constants and  $\sigma$  is the stress).

$$Z = \dot{\epsilon} \exp \left( \frac{Q_{def}}{RT} \right) = A [\sinh(\delta\sigma)]^n \quad (6.2)$$

However,  $\beta$  titanium alloys thermomechanically processed below the  $\beta$  transus temperature typically display flow softening, due to break-up of the microstructure during processing, which is not accounted for by Eq. 6.2 [76, 78].

An alternative model which allows for the change in stress due to the changing microstructure in titanium alloys was employed by Jackson [87]. The so-called ‘Bate-Brooks’ method is based on the approach outlined by Bate [88], further developed by Brooks [89], and successfully applied to the Nimonic AP1 nickel alloy by Blackwell et al. [90]. The method involves including a structure-related internal variable,  $\lambda$ , in the flow stress prediction model which can be related to a microstructural parameter.

Brooks described an equation which could be used to predict the instantaneous flow stress,  $\sigma$ , from the Zener-Hollomon parameter  $Z$ , the target (steady state) stress  $\sigma_{ss}$ , and the strain  $\epsilon$ , and from constants  $k$ ,  $m$  (temperature-compensated strain rate sensitivity), and  $\beta$ , Eq. 6.3 [89].

$$\sigma = \sigma_{ss} - kZ^m \exp(-\beta\epsilon) \quad (6.3)$$

Partial differentiation of Eq. 6.3 with respect to the strain gives a relationship between the stress and the steady state stress, valid when dynamic recovery is solely responsible for any flow

softening effects, Eq. 6.4.

When there is also a changing microstructural state, as there is in this Ti-5553 (caused by the break-up of  $\alpha$  laths), a target steady state structural value,  $\lambda_{ss}$ , determined by  $Z$ , also exists. This steady state value is related to the instantaneous value for the structure-related variable,  $\lambda$ , by Eq. 6.5, where  $\alpha$  is a constant. Partial differentiation of Eq. 6.5 gives a relationship between  $\lambda$  and  $\lambda_{ss}$  which is comparable to that of Eq. 6.4 for stress, Eq. 6.6 [89,90].

$$\frac{\partial \sigma}{\partial \varepsilon} = \beta(\sigma_{ss} - \sigma) \quad (6.4)$$

$$\lambda = \lambda_{ss} + (1 - \lambda_{ss}) \exp(-\alpha \varepsilon) \quad (6.5)$$

$$\frac{\partial \lambda}{\partial \varepsilon} = \alpha(\lambda_{ss} - \lambda) \quad (6.6)$$

The target stress,  $\sigma_{ss}$ , which tends to a steady state value beyond approximately 0.6 strain, can be related to  $Z$  and  $\lambda$  by Eq. 6.7 [89,90].

$$\sigma_{ss} = k\lambda Z^m \quad (6.7)$$

The target structural value,  $\lambda_{ss}$ , which also tends to a steady state value beyond approximately 0.6 strain, can be related to  $Z$  by Eq. 6.8 where  $\lambda_0$  and  $q$  are material constants [89,90].

$$\lambda_{ss} = \lambda_0 Z^q \quad (6.8)$$

These equations were used to analyse the flow stress curves for the compression testing performed in Chapter 5, and produce a predictive flow stress model which could be related to an internal structural variable,  $\lambda$ .

## 6.3 Experimental procedure

### 6.3.1 Derivation of Bate-Brooks constant values

To calculate the predicted stress,  $\sigma$ , the Bate-Brooks equations, Eq. 6.3, 6.5, 6.7, and 6.8 were used to find the initial values for the Bate-Brooks constants:  $m$ ,  $\alpha$ ,  $\beta$ ,  $q$ ,  $\lambda_0$ , and  $k$ .

$Z$  was calculated for each test using the average of the temperatures at the initial and steady state stresses, Eq. 6.1. For all tests, the steady state flow stress was assumed to be the stress value at 0.6 strain [89].  $\alpha$  and  $\beta$  were given arbitrary initial values of 5 and 50, respectively.

The natural log of Eq. 6.7 was taken to calculate  $m$ , which was determined by the gradient of the slope when  $\ln \sigma_{ss}$  was plotted against  $\ln Z$ , Eq. 6.9.

$$\ln \sigma_{ss} = m \ln Z + (\ln k + \ln \lambda) \quad (6.9)$$

$\lambda_{ss}$  was initially calculated for each test using Eq. 6.10 to allow rough initial  $q$  and  $\lambda_0$  values to be calculated for the predictive model, with  $\sigma_i$  being the initial stress (i.e. stress at 0 strain, calculated by back extrapolation). The natural log of Eq. 6.8 was taken, Eq. 6.11, and  $\ln \lambda_{ss}$  was plotted against  $\ln Z$  to determine the initial  $q$  and  $\lambda_0$  values, from the gradient and exponential of the y intercept, respectively.  $\lambda_{ss}$  values based on Eq. 6.8 were then calculated for each test using the initial  $q$  and  $\lambda_0$  values.

$$\lambda_{ss} = \frac{\sigma_{ss}}{\sigma_i} \quad (6.10)$$

$$\ln \lambda_{ss} = q \ln Z + \ln \lambda_0 \quad (6.11)$$

To calculate  $k$  for each test, Eq. 6.7 and 6.8 were combined to give Eq. 6.12 (for  $\lambda = \lambda_{ss}$ , which is true at 0.6 strain). An average of the  $k$  values for all tests was used as the initial  $k$  value.

$$k = \frac{\sigma_{ss}}{\lambda_0 Z^{(m+q)}} \quad (6.12)$$

Instantaneous  $\lambda$  was calculated using Eq. 6.5 for each test based on the true strain, and subsequently used to calculate instantaneous  $\sigma$  using a combination of Eq. 6.3 and 6.7, Eq. 6.13.

$$\sigma = k Z^m (\lambda - \exp(-\beta \varepsilon)) \quad (6.13)$$

The error between the experimental friction corrected flow stress data and the predicted stress data was calculated using Equation 6.14, where  $\sigma_{fr}$  is the friction corrected flow stress and  $\sigma$  is the predicted stress.

$$\text{Error} = \sum \left( \frac{\sigma_{fr} - \sigma}{\sigma_{fr}} \right)^2 \quad (6.14)$$

Table 6.1 shows the initial values of the Bate-Brooks constant values calculated by the preceding equations for 930 and 1000°C. The final optimised values shown in Table 6.1 were determined by minimising Eq. 6.14 using the Solver function in Microsoft Excel, which varied the  $m$ ,  $\alpha$ ,  $\beta$ ,  $q$ ,  $\lambda_0$  and  $k$  values.

Some tests were excluded from the sum of the error, Eq. 6.14, due to over-heating or under-heating during compression testing, which resulted in lower or higher flow stresses despite an isothermal correction subsequently being applied (due to heating above the  $\beta$  transus etc.).

$Q_{def}$  would be expected to be greater than that of self-diffusion in the  $\beta$  phase of titanium alloys, 152,818 Jmol<sup>-1</sup>, due to impurities such as alloying additions and the presence of the  $\alpha$  phase which impede deformation [91]. Therefore, it was fixed at the value found at 0.6 strain (i.e. the minimum steady state value), shown in Table 6.1.

Table 6.1: Initial and final Bate-Brooks constant values and parameters for 930 and 1000°C, with the error in %

Constant	930°C		1000°C	
	Initial	Final	Initial	Final
$m$	0.2184	0.2327	0.2297	0.2170
$\alpha$	5	4.642	5	4.5
$\beta$	50	52.69	50	57.37
$q$	-0.02021	0.02032	-0.03167	0.02
$\lambda_0$	1.1571	0.3918	1.388	0.4
$k$	0.6075	0.6767	1.542	1.651
$\frac{Q_{def}}{R}$ [K]	29942	29942	27426	27426
$Q_{def}$ [Jmol <sup>-1</sup> ]	248,817		227,907	
Error [%]	20.66		20.82	



### 6.3.2 Prediction of $\lambda$ from strain

FEM was used to model the compression tests, as described in Chapter 3. The effective strain values taken from the centre and side edge positions of the compressed specimens were used to find the  $\lambda$  values at those positions, which could then be correlated to a microstructural parameter.

The following equations, Eq. 6.15 and 6.16, and the final values in Table 6.1 were used to find  $\lambda$  at specific  $\varepsilon$  values, i.e.  $\lambda_n$  at  $\varepsilon_n$ .  $\lambda_{ss}$  was calculated using Eq. 6.15, a combination of Eq. 6.1 and 6.8.  $\Delta\lambda$  was derived in the Appendix from Eq. 6.6, and was combined with the recurrence relation  $\lambda_n = \lambda_{n-1} + \Delta\lambda$  to give Eq. 6.16. The starting values were  $\lambda_0 = 1$  and  $\varepsilon_0 = 0$ , where  $\varepsilon_n = \varepsilon_{n-1} + \Delta\varepsilon$ , and for all compression tests the strain difference,  $\Delta\varepsilon$ , was set at 0.01.

$$\lambda_{ss} = \lambda_0 \left[ \dot{\varepsilon} \exp \left( \frac{Q_{def}}{RT} \right) \right]^q \quad (6.15)$$

$$\lambda_n = \lambda_{n-1} + [\lambda_{n-1} - \lambda_{ss}] [\exp(-\alpha\Delta\varepsilon) - 1] \quad (6.16)$$

### 6.3.3 Image analysis of $\alpha$ phase

ImageJ image analysis software was used to select individual  $\alpha$  laths in each micrograph and measure a number of microstructural parameters including, among others, the area of each  $\alpha$  lath, and its maximum and minimum feret, Figure 6.1. The feret maximum and minimum are the maximum and minimum distances between any two points along the selection boundary, which correspond to the length and width of the  $\alpha$  lath, respectively.

The mean and median of the feret maximum, feret minimum, aspect ratio (feret maximum / minimum), and  $\alpha$  area were plotted against  $\lambda$  to determine if a relationship with  $\lambda$  existed. The compression tests excluded from the Bate-Brooks constant values' determination due to under or over-heating were also excluded from the image analysis relation to  $\lambda$ , as under or over-heating influences the microstructural parameters of the  $\alpha$  phase.

Microstructures were also imaged at the mid-radius, halfway between the centre and the side edge, of some compression tests to confirm the relationships between the microstructural parameters and  $\lambda$  (930°C: 785°C 1 s<sup>-1</sup> and 810°C 0.01 s<sup>-1</sup>, and 1000°C: 785°C 0.1 s<sup>-1</sup> and 835°C 1 s<sup>-1</sup>).

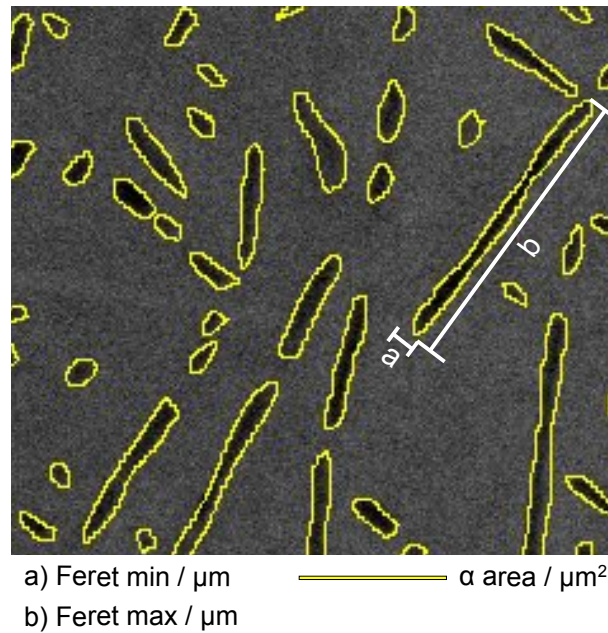


Figure 6.1: An example of  $\alpha$  phase analysis including: (a) feret minimum, (b) feret maximum, and (c)  $\alpha$  area, performed using ImageJ image analysis software [67]

#### 6.3.4 Complex Ti-5553 ‘eye bolt’ forging

Another 1000°C FAST specimen was produced, as described in Chapter 3. A 160 mm long bar with diameter 21 mm was machined from the specimen for forging, Figure 6.2. One edge of the bar cross-section was flat, as the height of the FAST specimen was only 19 mm (due to a limited amount of Ti-5553 powder).

A complex shape called an ‘eye bolt’ was forged using this bar at W.H. Tildesley Ltd to demonstrate the effectiveness of the FAST process to produce forgeable Ti-5553 billet material, and to validate the microstructural prediction model.

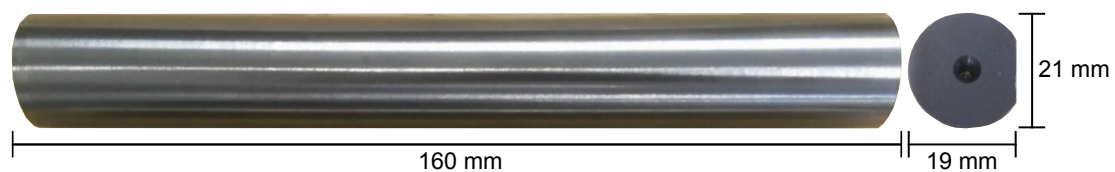


Figure 6.2: Machined Ti-5553 bar produced by FAST at 1000°C, prior to forging

The bar was pre-heated between 794–800°C for 22 min in a gas-fired furnace. A closed-die drop forge, Figure 6.3d, was used to forge the ‘eye bolt’, with two moulds being used to give a rough shape (starter) and a final shape (finisher) for five and six blows, respectively, Figure 6.3a–c. The dies were measured at 75–80°C prior to forging, and a water-soluble oil mix was used as a lubricant. The dies did not fill completely so the flash was left attached to the ‘eye bolt’, and it was water quenched after a delay of  $\sim 20$  s.



Figure 6.3: Closed-die multi-blow forging of the near-net shaped ‘eye bolt’ at W.H. Tildesley Ltd: (a) starter (left) and finisher (right) dies, (b) forged specimen after second blow on the starter die, (c) forged specimen after tenth blow on the finisher die, and (d) closed-die drop forge

FEM was used to model the ‘eye bolt’ forging, as described in Chapter 3. The effective strain values were taken from seven positions across a cross-section, from low to high strain, shown in Figure 6.10 with corresponding microstructure.

Initially, the  $\lambda$  values were to be predicted from the strain as described in Section 6.3.2. However, due to the nature of the drop forge process and the gas-fired furnace, the strain rate and temperature during forging were indeterminable, and subsequent FEM gave nonsensical values (i.e. temperatures close to the melting point of Ti-5553).

Instead, the microstructural relationships with  $\lambda$  for 1000°C in Figure 6.6 and 6.7 were used to calculate  $\lambda$  from the microstructural features, to then predict the temperature and strain rate at each position in the cross-section.

## 6.4 Results

### 6.4.1 Predicted flow stress

Figures 6.4 and 6.5 show the flow stresses predicted by the Bate-Brooks microstructural prediction models developed for Ti-5553 produced by FAST at 930 and 1000°C, respectively, compared with the experimental flow stresses.

There is good agreement between the experimental flow stresses and the stresses predicted by the Bate-Brooks model in Figure 6.4 and 6.5, once certain tests are excluded due to under or over-heating during compression testing. The predicted stresses demonstrate the same flow softening effect with increasing strain, and result in similar steady state stresses, i.e. the stress at 0.6 strain.

There is an assumption in the model that all the microstructural changes are due to deformation during hot compression testing. However, temperature alone will have some effect on the microstructure, which may explain why there are some discrepancies between the predicted and experimental stress values.

Overall though, the models work reasonably well to predict the flow stresses for various compression temperatures and strain rates.

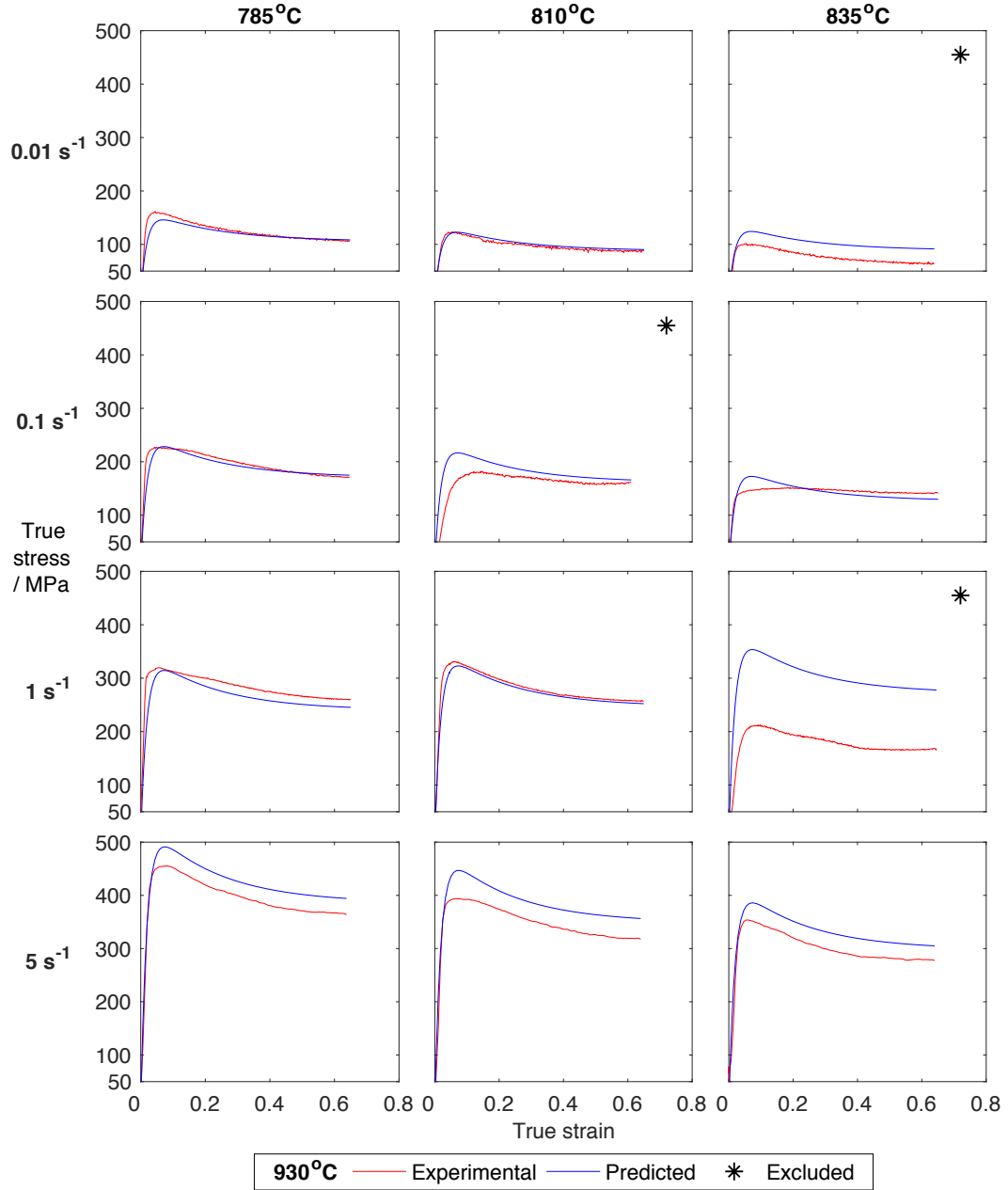


Figure 6.4: Stresses predicted by the Bate-Brooks model compared to the experimental stresses for Ti-5553 produced by FAST at 930°C. The Bate-Brooks constant values derived from the model, Table 6.1, were used. Some tests were excluded due to under or over-heating during compression testing. The error was 20.66 %

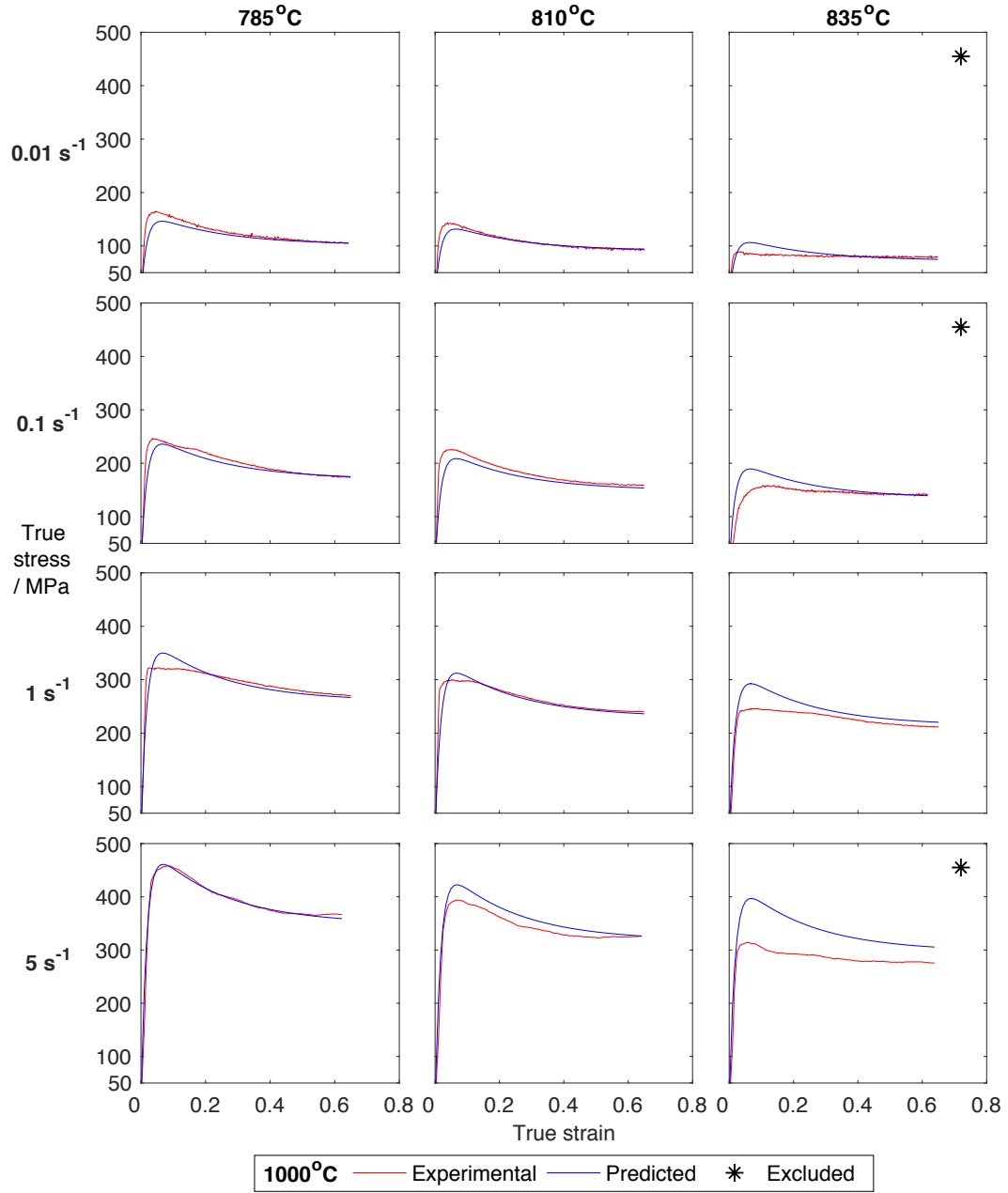


Figure 6.5: Stresses predicted by the Bate-Brooks model compared to the experimental stresses for Ti-5553 produced by FAST at 1000°C. The Bate-Brooks constant values derived from the model, Table 6.1, were used. Some tests were excluded due to under or over-heating during compression testing. The error was 20.82 %

### 6.4.2 Relationship between $\lambda$ and $\alpha$ phase microstructural parameters

Significant linear relationships with  $\lambda$ , regardless of compression temperature or strain rate, were found only for the mean feret minimum and median  $\alpha$  area, Figures 6.6 and 6.7, respectively. The measured values for the mean feret minimum and median  $\alpha$  area with respect to  $\lambda$  are shown for each strain rate and FAST temperature. The lines of best fit for all measured values and the mid-radius points which confirm the accuracy of these derived relationships are also shown.

The mean feret minimum and median  $\alpha$  area decrease with increasing  $\lambda$  for both FAST temperatures.  $\lambda$  is dependent on the strain rate, strain, and temperature during compression tests (Eq.s 6.1, 6.5, 6.8); it can be seen in Figures 6.6 and 6.7 that  $\lambda$  generally increases with increasing strain rate, which is associated with a decrease in the mean feret minimum and median  $\alpha$  area.

The mid-radius points taken to examine the accuracy of the derived relationships are shown to fit well with the lines of best fit in Figures 6.6 and 6.7.

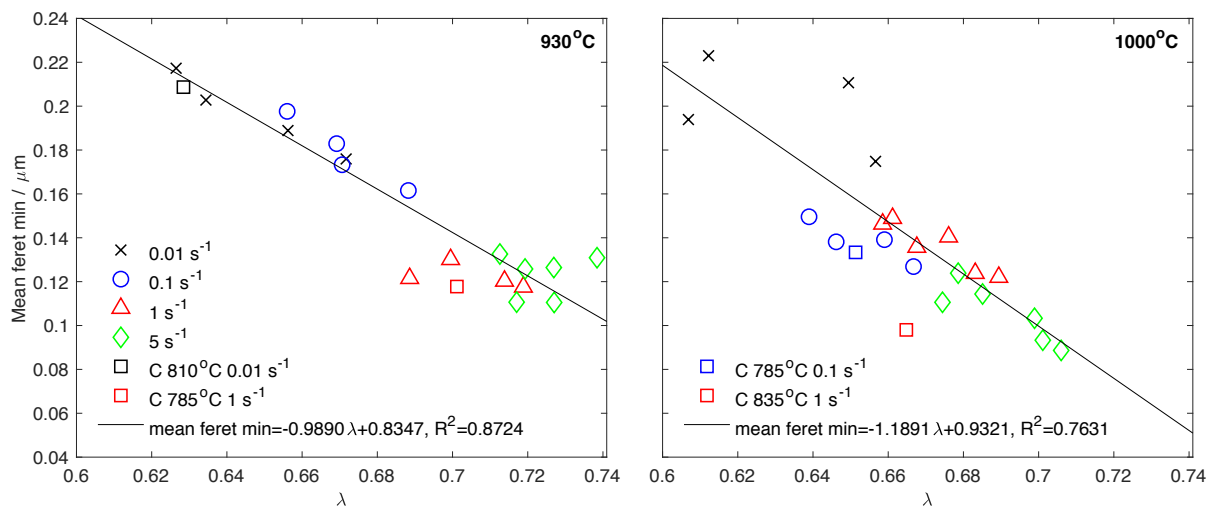


Figure 6.6: Relationship between the measured mean feret minimum values and  $\lambda$ , with different strain rates and FAST temperatures (930 and 1000°C) shown, and mid-radius points confirming the accuracy of the derived relationship

Significant linear relationships between the aspect ratio of the  $\alpha$  laths and  $\lambda$  were also found, Fig 6.8, although they were dependent on the strain rate of the compression test. The aspect ratio increases as  $\lambda$  increases for all strain rates, and the gradients of the lines of best fit generally increase with increasing strain rate.

The mid-radius points taken to examine the accuracy of the derived relationships are shown to fit well with the lines of best fit, which demonstrates that the aspect ratio can be accurately predicted using  $\lambda$  when controlled strain rates of 0.01, 0.1, 1, and 5 s<sup>-1</sup> are used.



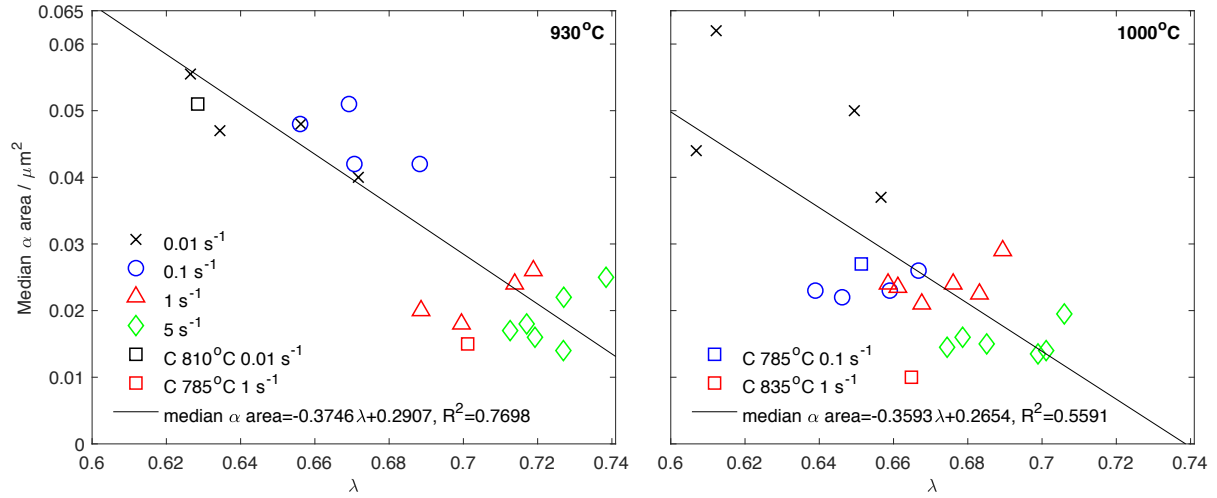


Figure 6.7: Relationship between the measured median  $\alpha$  area values and  $\lambda$ , with different strain rates and FAST temperatures (930 and 1000°C) shown, and mid-radius points confirming the accuracy of the derived relationship

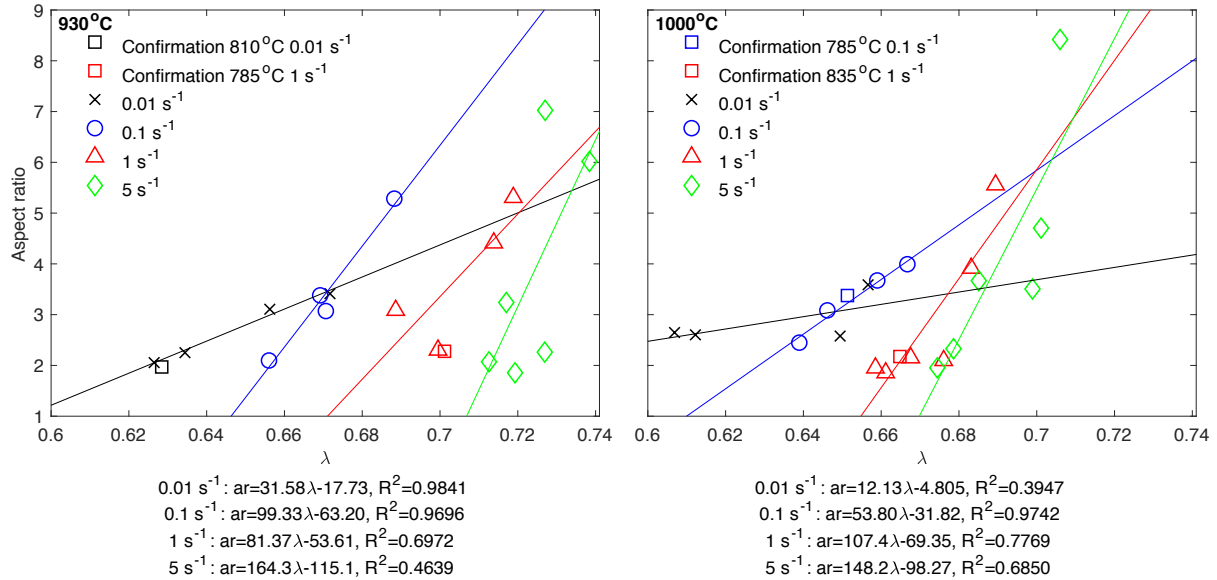


Figure 6.8: Relationship between the measured aspect ratio values and  $\lambda$  for different strain rates and FAST temperatures (930 and 1000°C), and mid-radius points confirming the accuracy of the derived relationships



### 6.4.3 Forged Ti-5553 ‘eye bolt’ specimen

#### 6.4.3.1 Microstructural examination and FEM

Figure 6.9 shows the forged ‘eye bolt’ alongside the FEM simulation of the multi-blow forging. The starter and finisher dies used during forging are shown in Figure 6.3a, along with video stills of the second and tenth blow, Figure 6.3b and c, and the closed-die drop forge used, Figure 6.3d.

Both sides of the ‘eye bolt’ show under-filling of the dies due to insufficient material, as the size of the forged bar was limited by the FAST specimen height. The simulation accurately duplicates the under-filling of the dies and shows the effective strain within the forged ‘eye bolt’.

A slice of the forged ‘eye bolt’ specimen was taken to examine the microstructure at various positions, from low (P1) to high (P7) strain, Figure 6.10. The FEM simulation was used to find the effective strain at the seven corresponding positions.

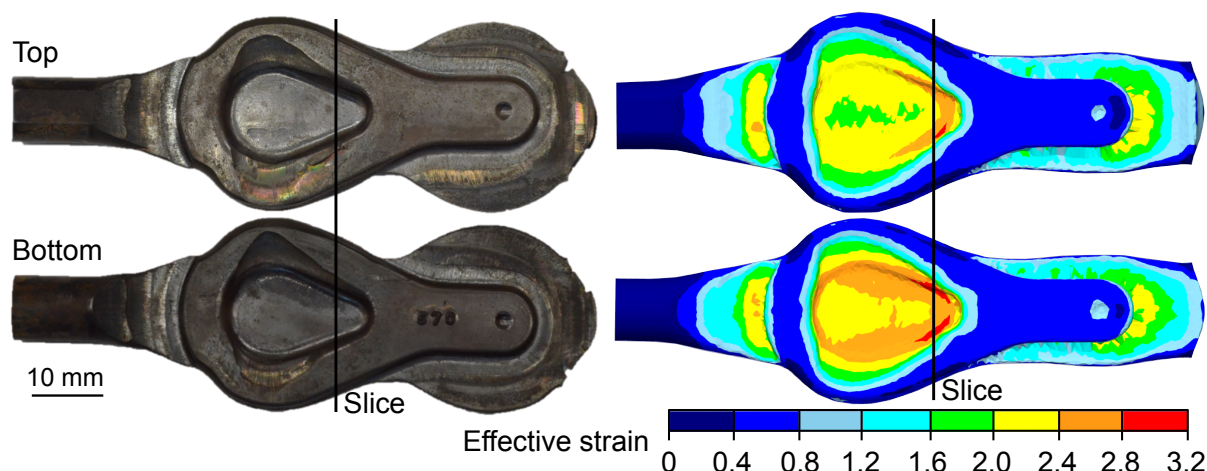


Figure 6.9: Forged Ti-5553 ‘eye bolt’ specimen and its FEM simulation, which shows the effective strain imparted during forging. Vertical lines indicate where the forged specimen was sectioned to produce a slice for microstructural examination (see Figure 6.10) and the corresponding slice taken from the FEM simulation. The forging direction is into the page

Compared to P5–P7, P1–P4 contain a larger volume fraction of the  $\alpha$  phase, which is also more lath-like in structure, due to relatively low strains. From P1–P4 the level of break-up and spherodisation of  $\alpha$  increases, and the  $\alpha$  laths become more aligned with the perpendicular of the forging direction due to increasing strain and temperature (deformation heating). In P5–P7 there is primarily spherodised  $\alpha$  phase, as the laths have been broken upon during deformation due to higher strains. P5 contains a larger volume fraction of  $\alpha$  compared to P6 and P7, which indicates that the temperature was higher at P6 and P7.

There is some indication of the presence of  $\beta$  sub-grains in P1–P7, especially at higher strains.

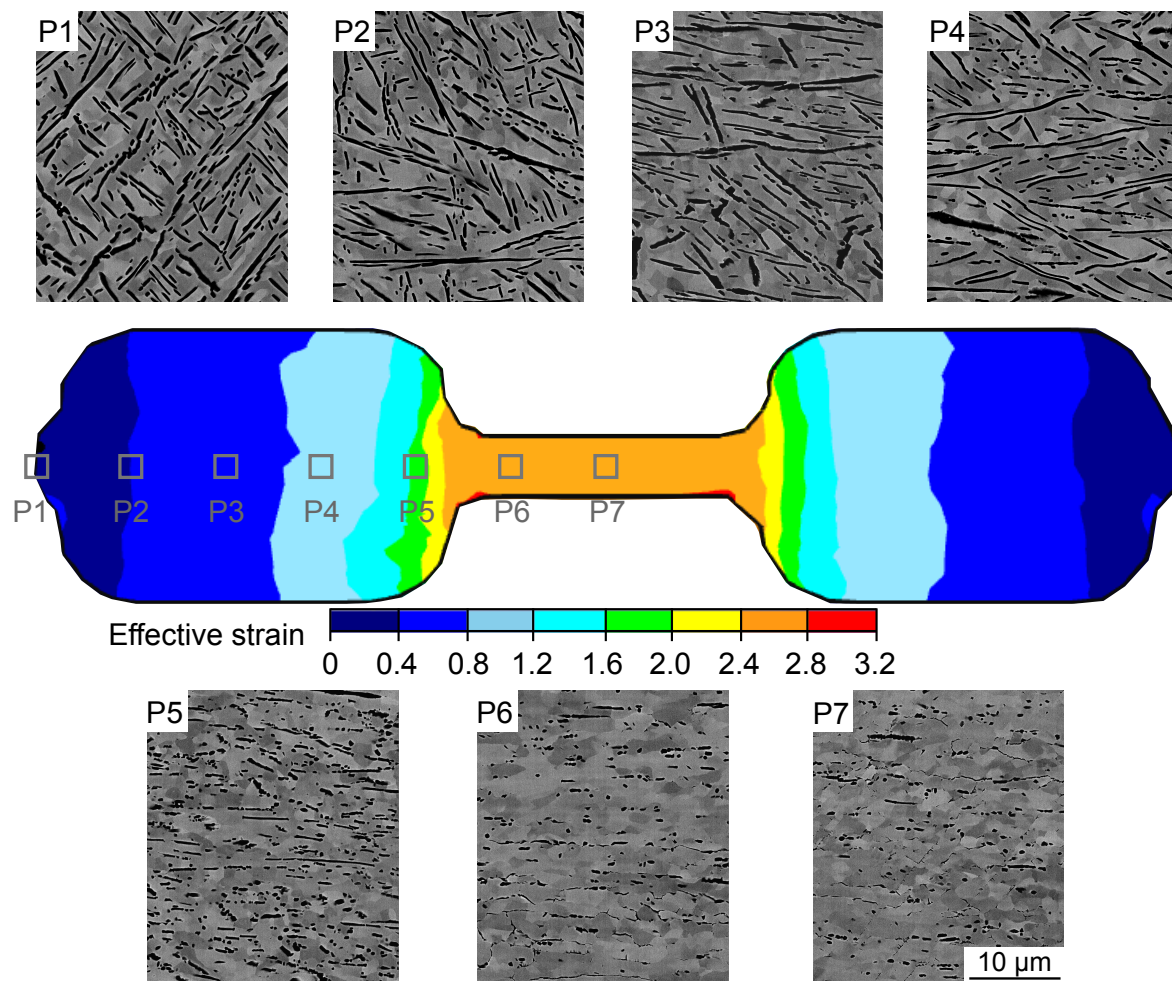


Figure 6.10: FEM simulation slice of the forged Ti-5553 ‘eye bolt’ specimen, corresponding to the vertical line in Figure 6.9. Positions 1–7 indicate the progression from low to high strain throughout the forged specimen, with the corresponding microstructures shown. The forging direction is in line with the page

#### 6.4.3.2 $\alpha$ phase analysis

The  $\lambda$  values for the forged ‘eye bolt’ specimen were calculated from the measured mean feret minimum and median  $\alpha$  area, using the line of best fit equations for 1000°C in Figure 6.6 and 6.7. This produced unrealistic values, however, as the heating dwell period of 22 min for the ‘eye bolt’ specimen was much longer than that of the compression specimens, which were heated for 20 s.

To allow for the  $\alpha$  phase growth which would have occurred during this extended time at temperature, the mean feret minimum was divided by 2.5 (an approximation made due to the difference in SEM magnification for the ‘eye bolt’ and compression specimens). It was therefore assumed that the median  $\alpha$  area would be corrected by dividing by 6.25 ( $2.5^2$ ).

The calculated  $\lambda$  values were used to estimate the temperature and strain rate during forging.

The temperature was limited to less than 890°C due to the existence of  $\alpha$  phase, Figure 6.10, which would not exist above the  $\beta$  transus temperature of  $\sim 890^\circ\text{C}$ . The minimum temperature was limited to 800°C for P1–P3 and 700°C for P4–P7 to produce realistic strain rate values.

The range of temperatures and strain rates for each position is given in Table 6.2 for the mean feret minimum, and Table 6.3 for the median  $\alpha$  area. The ranges show the degree of variability of strain rate within the same specimen during forging. At most positions there is some overlap between the estimated strain rates in Tables 6.2 and 6.3.

Table 6.2: Estimated minimum and maximum temperatures ( $T$ ) and strain rates ( $\dot{\epsilon}$ ) at positions P1–P7 in the forged ‘eye bolt’ specimen, using the  $\lambda$  values calculated from the mean feret minimum divided by 2.5

Position	$\epsilon$	Min. $T$	Max. $T$	Min. $\dot{\epsilon}$	Max. $\dot{\epsilon}$	$\lambda$
P1	0.304194717	800	890	2.03834E-06	1.47332E-05	0.639370315
P2	0.418674517	800	890	0.008373624	0.06052501	0.665587389
P3	0.676035127	800	890	0.006849577	0.049509114	0.62223046
P4	0.907400829	700	890	0.026843842	2.6835866	0.65959327
P5	1.763011428	700	890	0.14670251	14.665892	0.67653542
P6	2.623984804	700	890	0.2245245	22.445778	0.682202181
P7	2.568832802	700	890	0.17085831	17.080754	0.678486126

Table 6.3: Estimated minimum and maximum temperatures ( $T$ ) and strain rates ( $\dot{\epsilon}$ ) at positions P1–P7 in the forged ‘eye bolt’ specimen, using the  $\lambda$  values calculated from the median  $\alpha$  area divided by 6.25

Position	$\epsilon$	Min. $T$	Max. $T$	Min. $\dot{\epsilon}$	Max. $\dot{\epsilon}$	$\lambda$
P1	0.304194717	800	890	2.4823E-08	1.79422E-07	0.607291957
P2	0.418674517	800	890	0.003511317	0.025379994	0.656721403
P3	0.676035127	800	890	0.002331775	0.016854193	0.609963819
P4	0.907400829	700	890	0.000800453	0.08002153	0.615975508
P5	1.763011428	700	890	0.26882898	26.87491	0.684775953
P6	2.623984804	700	890	0.62678395	62.65977	0.696354022
P7	2.568832802	700	890	0.23408652	23.401696	0.682772057

## 6.5 Discussion

### 6.5.1 Bate-Brooks microstructural prediction model

The so-called ‘Bate-Brooks’ method has been used to predict the flow stress of Ti-5553 during compression tests, carried out at various temperatures and strain rates. The inclusion of a structure-related internal variable,  $\lambda$ , in the equation for the predicted flow stress has led to similar flow softening behaviour and steady state stress values compared to the measured flow stresses for compression specimens produced by FAST at 930 and 1000°C, with errors of  $\sim 21\%$ , Figures 6.4 and 6.5.

Similarities between the predicted stresses for the different FAST temperatures of 930 and 1000°C can be seen when comparing Figures 6.4 and 6.5, and in the final values for the Bate-Brooks constant values in Table 6.1. These similarities are also illustrated in Chapter 5 in Figures 5.4 and 5.5, where both FAST temperatures produce a microstructure consisting of fine  $\alpha$  laths in a  $\beta$  matrix, and in Figure 5.7 where the measured stress values are very similar for 930 and 1000°C (excluding the tests which were known to have over or under-heated).

Following the determination of the Bate-Brooks constant values in Table 6.1, and using FEM simulations of the compression tests to determine the strain, the values for  $\lambda$  were calculated.  $\lambda$  was found to relate to the mean feret minimum and median  $\alpha$  area, Figures 6.6 and 6.7, regardless of the temperature and strain rate used during compression testing. The mid-radius points taken to examine the accuracy of the derived relationships are shown to fit well with the lines of best fit, which demonstrates that the mean feret minimum and median  $\alpha$  area can be accurately predicted using the line of best fit equations and  $\lambda$ .

According to Eq. 6.1,  $Z \propto \dot{\epsilon}$  and  $Z \propto \exp\left(\frac{1}{T}\right)$ . Therefore,  $\lambda_{ss} \propto \dot{\epsilon}$  and  $\lambda_{ss} \propto \exp\left(\frac{1}{T}\right)$  must also be true, Eq. 6.8, and consequently  $\lambda \propto \dot{\epsilon}$  and  $\lambda \propto \exp\left(\frac{1}{T}\right)$ , Eq. 6.5. From Eq. 6.5,  $\lambda \propto \exp(-\epsilon)$  is also true. An increase in  $\lambda$  therefore corresponds to an increase in strain rate ( $\dot{\epsilon}$ ), and a decrease in temperature ( $T$ ) and strain ( $\epsilon$ ).

The mean feret minimum and median  $\alpha$  area both decreased with increasing  $\lambda$ , which roughly corresponds to an increase in strain rate. At higher strain rates, the  $\alpha$  laths may be more broken up and spherodised, and the  $\alpha$  volume fraction may be slightly lower, which could have caused a reduction in the mean feret minimum and median  $\alpha$  area values with increasing strain rate.

However, an increase in  $\lambda$  not only corresponds to an increase in the strain rate, but also to a decrease in temperature, as described above. A decrease in temperature would also lead to a reduction in the mean feret minimum and median  $\alpha$  area due to decreased diffusion at lower temperatures.

The relationships between the mean feret minimum and the median  $\alpha$  area and  $\lambda$  were comparable for both FAST temperatures: this confirms the observation that the predicted flow stresses, Bate-Brooks constant values, and microstructures were similar for both.

Significant relationships were also found between the aspect ratio and  $\lambda$  for both FAST temperatures, although they were dependent on the strain rate, Figure 6.8. The aspect ratio of the feret maximum to the feret minimum increases as  $\lambda$  increases for each strain rate. This is likely due to the decrease in strain, which increases  $\lambda$ , and results in an increase in the aspect ratio as the amount of break-up and spheroidisation of the  $\alpha$  laths reduces.

While the relationships between the aspect ratio and  $\lambda$  are useful for tests with a controlled strain rate and near isothermal conditions, the relationships between the mean feret minimum and median  $\alpha$  area and  $\lambda$  are far more useful for practical applications, such as complex-shaped forgings, as they are independent of strain rate and temperature. Complex shapes can produce varying strain rates within a specimen, and temperatures can fluctuate owing to differing thicknesses and cooler dies.

### 6.5.2 Forged Ti-5553 ‘eye bolt’ specimen

The forged ‘eye bolt’ is an example of a complex-shaped forging. The specimen, shown in Figure 6.9, showed no sign of cracking despite being forged in non-isothermal conditions, and with limited strain rate and temperature control (due to the nature of the drop forging process). The machined bar’s size, Figure 6.2, was limited by the height of the FAST billet and was therefore too small for the dies, which led to under-filling.

It is believed that this is the first time a complex-shaped forging has been produced from Ti-5553 billet produced by FAST, and it was forged without issue, in spite of limited processing control.

It was intended that the ‘eye bolt’ would be used as confirmation of the relationship between the chosen microstructural parameter and  $\lambda$ . However, the calculation of  $\lambda$  involves knowledge of the strain rate and temperature, neither of which could be accurately measured during the drop forging process. The FEM simulation gave nonsensical values for the strain rate and temperature, which were clearly too high, so they could not be used. Also, the long pre-heat in the furnace increased the size of the  $\alpha$  phase, which meant that the measured values of the mean feret minimum and median  $\alpha$  area needed to be adjusted (by  $2.5\times$  and  $6.25\times$ , respectively).

For reference, the growth of the  $\alpha$  phase is clearly significant when the pre-forged microstructure, shown in Figure 5.4, is compared with that in Figure 6.10.

Therefore, the  $\lambda$  values were calculated using the effective strain from the FEM simulation,

Figure 6.9, and used to estimate the temperatures and strain rates during forging. The presence of  $\alpha$  phase in Figure 6.10 proves that the temperature did not exceed the  $\beta$  transus temperature of  $\sim 890^\circ\text{C}$ , so this was set as the maximum temperature at all positions. The minimum temperatures were limited to produce realistic values for the strain rates.

There is a large amount of variability in the strain rate values within the specimen, which demonstrates the complexity of the drop forging process when compared to uniaxial compression testing.

P1–P4 have similar  $\alpha$  phase volume fractions, which implies that they were at similar temperatures and relatively similar strains (as shown in Table 6.2). P5–P7 have lower  $\alpha$  volume fractions compared to P1–P4 which implies that they were at higher temperatures. P5 contains more  $\alpha$  phase than P6 and P7, however, possibly due to the lower strain (1.76 compared to 2.62 and 2.57).

From P1–P4 the  $\alpha$  laths become more broken up and more aligned to the perpendicular of the forging direction, as strain increases. P5 contains far more broken up and spherodised  $\alpha$  phase than P4, likely due to the doubling in strain from P4–P5 (0.91–1.76). P6 and P7 have the highest strains, Table 6.2, which have led to highly spherodised and broken up  $\alpha$ . Both have low  $\alpha$  volume fractions which are possibly caused by increased deformation heating due to higher strain rates, although P6 has slightly less than P7 as a result of slightly higher strain.

These observations generally correlate to the predicted strain rates in Tables 6.2 and 6.3, where P1 has the lowest strain rate and P6 the highest. At higher strain rates the  $\alpha$  laths are more broken up and spherodised, as shown in Figures 6.6 and 6.7, where higher strain rates led to increased flow softening. However, due to the higher R-squared measure of fit for the relationship between the mean feret minimum and  $\lambda$  compared to the median  $\alpha$  area and  $\lambda$ , the strain rate values are more likely to be closer to those of Table 6.2.

The microstructure in Figure 6.10 can be compared with that of the double truncated cones produced by FAST at the same temperature,  $1000^\circ\text{C}$ , and forged at  $785$ ,  $810$  and  $835^\circ\text{C}$  at approximately  $3\text{ s}^{-1}$ , Figure 5.10. The scale of the ‘eye bolt’ microstructures is twice that of the cones, and the  $\alpha$  size and morphology in P1 bears most resemblance to that of the lowest strain microstructure of the cone forged at  $810^\circ\text{C}$  (both with strain of 0.3), implying that the ‘eye bolt’ was forged at approximately  $810^\circ\text{C}$ .

As seen within the double truncated cones in Figure 5.10, there are also  $\beta$  sub-grains present in Figure 6.10. They are more prominent than the sub-grains seen in the cones, which implies that there is more deformation, and therefore that the ‘eye bolt’ was forged at a strain rate higher than  $3\text{ s}^{-1}$ . The sub-grains also become more obvious as the strain increases, P1–P7, which

is as seen in the microstructure of the compression test specimens and the cones, Figures 5.6 and 5.10.

## 6.6 Conclusions

The Bate-Brooks method has been used to relate a structure-related internal variable,  $\lambda$ , to the flow stress of Ti-5553 produced by FAST.  $\lambda$  was then related to various microstructural features, so that the microstructure could be predicted from the flow stress.

The main conclusions drawn from this chapter are as follows.

1. The predicted flow stress calculated by the Bate-Brooks method was found to produce similar flow softening behaviour and steady state stress values, when compared to the measured flow stresses for compression specimens produced by FAST at 930 and 1000°C.
2. Significant relationships were found between the mean feret minimum and median  $\alpha$  area and  $\lambda$ , for all strain rates and temperatures. The mean feret minimum and median  $\alpha$  area both decreased as  $\lambda$  increased, which roughly corresponded to an increase in strain rate due to increased break-up and spherodisation of  $\alpha$  laths. These relationships are particularly useful as they are independent of strain rate and temperature, and therefore can be used for forging where the strain rate or temperature is not easily controlled or is not consistent within the forging.
3. Significant relationships were also found between the aspect ratio of feret maximum to feret minimum and  $\lambda$  for each strain rate. The aspect ratio decreased as  $\lambda$  decreased due to an increase in strain, which caused break-up and spherodisation of the  $\alpha$  laths.
4. The forged ‘eye bolt’ specimen shows that a Ti-5553 billet produced by FAST can be forged into a complex shape with no cracking, despite minimal control over strain rate and temperature.
5. The microstructure of the ‘eye bolt’ specimen was taken at seven positions which corresponded to positions in the FEM simulation to give the strain values. As the strain increased from P1–P7, the  $\alpha$  laths became more spherodised and broken up, and more aligned with the perpendicular of the forging direction. P6 and P7 experienced the highest strains and strain rates, and as such contained a lower  $\alpha$  phase volume fraction and the most spherodised  $\alpha$  phase.
6. The relationships between the mean feret minimum and median  $\alpha$  area and  $\lambda$  were used to predict the strain rate and temperature at seven positions within the ‘eye bolt’ forged specimen. The temperatures could be roughly predicted from the microstructure and



allowed ranges to be calculated for the strain rates. Strain rates were found to generally correlate with the microstructural observations made.

7. There were similarities between the microstructure found in the ‘eye bolt’ specimen and that of the forged double truncated cones in Chapter 5. The  $\alpha$  laths were similar in size to those of the cone forged at 810°C, implying that the ‘eye bolt’ was forged at around that temperature.  $\beta$  sub-grains were also seen in both specimens, although they were more prominent in the high strain regions of the ‘eye bolt’ specimen than the high strain regions of the cones, implying that the strain rate was higher than  $3 \text{ s}^{-1}$  (that of the forged cones) in the ‘eye bolt’ specimen.

## Chapter 7

# FAST of Ti-5553–TiFeMo Composites

### 7.1 Outline

This chapter contains a literature review and experimental procedure which are specific to the TiFeMo alloy, composites, and reinforcement methods for Ti-5553. The literature review should be used in conjunction with the literature review in Chapter 2. The majority of the results in this chapter have been published previously in Scripta Materialia in [7].

## 7.2 Literature review

### 7.2.1 Current reinforcement methods for Ti-5553

High strength, heavily alloyed titanium alloys such as Ti-5553 can possess yield strengths of  $\sim 1300$  MPa, which given the relatively low density of titanium, results in favourable combinations of specific strength ( $\sim 280 \text{ kNmkg}^{-1}$ ) and specific toughness ( $\sim 9 \text{ kNm}^{3/2}\text{kg}^{-1}$ ) [92] compared to even the best steels, such as A300M ( $267 \text{ kNmkg}^{-1}$  and  $9 \text{ kNm}^{3/2}\text{kg}^{-1}$ ) [93, 94].

These alloys achieve these strengths and toughnesses through the precipitation of a high volume fraction of 10–25 nm fine-scale hcp  $\alpha$  phase within the bcc  $\beta$  matrix [23, 95], but the improvement in properties achieved in titanium alloys has begun to plateau in recent years, following much progress that was achieved in the 1950s to 1970s [1].

Long-fibre ceramic reinforcement, e.g. with SiC has long been proposed, chiefly using relatively conventional alloys such as Ti-6Al-4V as the matrix [96], and more recently the use of high strength Ti-5553 as the matrix has achieved specific strengths as high as 2050 MPa (in tension) and 3500 MPa (in compression) [97]. However, such microstructures require the laying-up of a composite structure using ceramic fibres, which is a costly manufacturing route.

Ti-5553 has also been reinforced with 12 vol% of TiB and TiC in various ratios using FAST, which produced an increase in hardness of 15–20 % and an increase in compressive strength of 18–23 % [98]. However, there were issues with reinforcement particle delamination from the matrix, which led to failure of the compression specimens at low strains ( $< 0.3$ ).

In conclusion, there are currently a limited number of methods for reinforcement of Ti-5553, and these have issues such as high manufacturing cost and low ductility.

### 7.2.2 TiFeMo alloy

Fe addition to titanium results in the formation of  $\beta$  eutectoid systems [13]. TiFe alloys have previously been investigated because Fe can provide solid solution strengthening to titanium, due to its high misfit at low solute content when compared to other eutectoid forming elements [13, 99].

Mo is a  $\beta$  isomorphous stabilising element: it therefore has the benefit of stabilising the bcc  $\beta$  phase in titanium [13]. In the TiFeMo alloy, at selected chemistries, a Mo-rich bcc A2  $\beta$  phase and an Fe-rich B2  $\beta'$  phase exist in the form of  $\sim 50$  nm ordered  $\beta'$  B2 TiFe intermetallics within an A2 Ti, Mo  $\beta$  phase matrix (where A2 and B2 are the Strukturbericht designations for an  $\text{Im}\bar{3}\text{m}$  body-centred cubic (bcc) structure and a  $\text{Pm}\bar{3}\text{m}$  (primitive) simple cubic (CsCl) structure, respectively) [100–102]. Such TiFeMo alloys can possess strengths in the order of

2 GPa, but have low ductility [101].

Following the positive results shown in Chapters 4 and 5, FAST was utilised as a low-cost processing route for the production of a Ti-5553 and TiFeMo composite. It was theorised that the TiFeMo alloy particles would be strengthened by the  $\beta'$  B2 TiFe intermetallics and the  $\omega$  phase, as seen previously in [101]. These strengthened particles were expected to act as hard precipitates in the softer Ti-5553 matrix, and provide reinforcement while allowing for plastic deformation [103]. As TiFeMo and Ti-5553 both possess a  $\beta$  matrix, interdiffusion during FAST was anticipated to produce strong interfacial bonding without the precipitation of undesirable brittle phases [104].

This chapter evaluates the mechanical behaviour of the Ti-5553–TiFeMo composites produced by FAST.

### 7.2.3 Detection of $\omega$ phase using TEM diffraction patterns

Transmission electron microscopy (TEM) has been used to produce selected area diffraction patterns (SADPs), from which the phases present and the crystal structure can be determined. Electrons emitted during TEM are diffracted by their interaction with atoms of the crystal lattice, and are scattered to certain specific angles based on the crystal structure.

The incident beam is the un-diffracted beam and is usually shown as the brightest diffraction spot in the centre, Figure 7.1c. The zone axis used in Figure 7.1 and in the results for this chapter is the  $[110]_{\text{bcc}}$ , which is aligned with the  $[110]$  direction in the bcc lattice. The nine brightest spots are therefore the reflections from the interactions between the electron beam and the atoms of the bcc  $\beta$  phase, shown in Figure 7.1.

Figures 7.1a and e show the commensurate (ideal) position of the  $\omega$  phase, between the  $\beta$  phase reflections [14, 106]. Figures 7.1b and f show the incommensurate (partial) position of the  $\omega$  phase in solution treated and quenched Ti-5553 (athermal), and Ti-Cr and Ti-V alloys, respectively [14, 106]. The  $\omega$  phase reflections in these diffraction patterns are diffuse and smeared, whereas the incommensurate  $\omega$  phase shown in Figure 7.1g for Ti-Fe alloys has sharp circular reflections [106]. Figures 7.1c and d show the  $\alpha$  reflections following ageing of Ti-5553 at 400°C for 8 h [105].

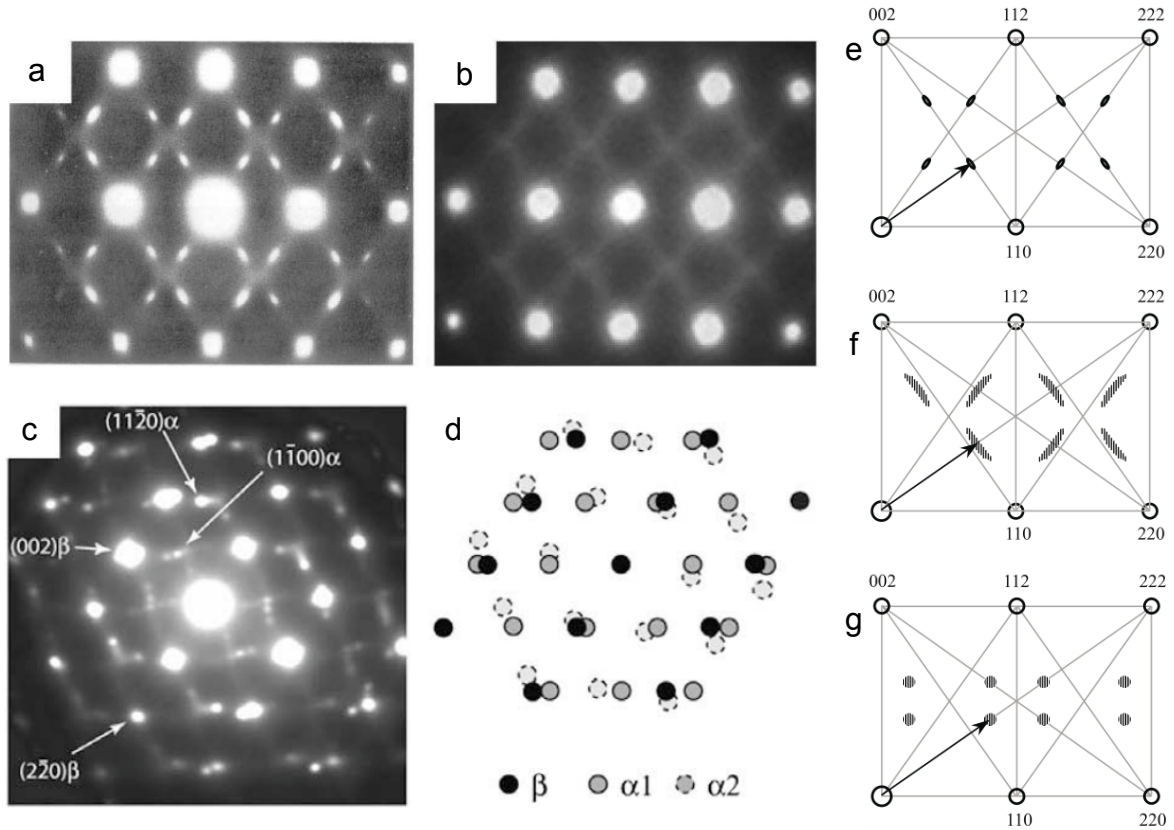


Figure 7.1: Selected area diffraction patterns from the  $[110]_{\text{bcc}}$  zone axis of: (a) the commensurate (ideal)  $\omega$  phase (Zr-Nb alloy), (b) solution treated and quenched Ti-5553, showing the athermal incommensurate (partial)  $\omega$  phase with diffuse streaking, and (c) aged Ti-5553, showing the  $\alpha$  and  $\beta$  phases. Key diagrams of: (d) the diffraction pattern shown in (c), (e) the position of the commensurate (ideal)  $\omega$  phase, (f) the position of the incommensurate  $\omega$  phase with smeared reflections, seen in Ti-Cr and Ti-V alloys, and (g) the position of the incommensurate  $\omega$  phase seen in Ti-Fe alloys, where the open circles are bcc  $\beta$  phase reflections and the shaded circles are  $\omega$  phase reflections [14, 105, 106]

### 7.3 Experimental procedure

#### 7.3.1 TiFeMo powder

Wrought Ti-5553 was gas atomised as described in Chapter 3 to produce spherodised powder with chemistry and particle size distribution (PSD) reported in Tables 7.1 and 7.2. The TiFeMo alloy processed as described in [100] was mechanically ground to produce an angular powder, Tables 7.1 and 7.2. PSD for Ti-5553 powder was measured using a Malvern Mastersizer 3000 laser particle size analyser using the dry dispersion method; for the TiFeMo powder particles were measured post-FAST using ImageJ image analysis software [67] and a cumulative frequency distribution gave values for Dx10, Dx50 and Dx90 (Dx10 is the size of powder particles relating to 10 % of the cumulative mass, etc.).

Table 7.1: Chemical analysis of Ti-5Al-5Mo-5V-3Cr gas atomised powder, and TiFeMo alloy powder (wt.%)

	<b>Al</b>	<b>Cr</b>	<b>Fe</b>	<b>Mo</b>	<b>Ni</b>	<b>V</b>	<b>Ti</b>
Ti-5553	5.1	2.7	0.4	5.1	0.1	5.2	80.8
TiFeMo	0	0	15.8	36.6	0	0	47.6

#### 7.3.2 FAST production

FAST was performed using an FCT Systeme GmbH Spark Plasma Sintering furnace type HP D 25. Three specimens were produced with a diameter of 20 mm, (1) Ti-5553, (2) Ti-5553 with 10 wt.% TiFeMo (Ti-5553–10 wt.% TiFeMo), and (3) Ti-5553 with 25 wt.% TiFeMo (Ti-5553–25 wt.% TiFeMo).

The FAST parameters used were: 1200°C dwell temperature held for 30 min and 60 min for Ti-5553, and 60 min for the Ti-5553–TiFeMo composites; 35 MPa pressure; 200°C/min heating rate; and a rapid cooling of  $\sim 250^\circ\text{C}/\text{min}$  to room temperature following the dwell period. Full details of FAST testing are given in Chapter 3.

Table 7.2: Particle size distribution (PSD) of spherical Ti-5553 powder, and angular TiFeMo powder (for both the Ti-5553–10 wt.% TiFeMo and Ti-5553–25 wt.% TiFeMo composites) ( $\mu\text{m}$ )

	<b>Dx10</b>	<b>Dx50</b>	<b>Dx90</b>
Ti-5553	22	63	115
10 wt.% TiFeMo	16	40	158
25 wt.% TiFeMo	14	35	63

### 7.3.3 Compression testing

Post-FAST, two 6 mm diameter by 9 mm high cylindrical specimens were wire electrical discharge machined from the Ti-5553 (30 min dwell) and Ti-5553–25 wt.% TiFeMo FAST specimens. These were compressed at room temperature (RT) at a strain rate of  $0.1 \text{ s}^{-1}$  to a true strain of 0.5 using a Servotest Thermomechanical Compression (TMC) machine, as described in more detail in Chapter 3, which was used to simulate upset forging (FAST-*forg*). Two cylindrical specimens were also compressed from the Ti-5553–10 wt.% TiFeMo FAST composite, for microstructural examination only.

### 7.3.4 Solution heat treatment and ageing

The compressed specimens were subsequently solution treated at  $785^\circ\text{C}$  for 2 h, furnace cooled to RT, and then aged at  $500^\circ\text{C}$  for 8 h (furnace cooled to RT) in an Elite furnace operated under vacuum.

### 7.3.5 Microscopy

Specimens were sectioned parallel to the compression direction and metallurgically prepared, as in Chapter 3.

Scanning electron microscopy (SEM) was performed using an FEI Inspect F50 in the backscatter electron imaging (BSEI) mode, using 10 kV accelerating voltage and working distance of  $\sim 10 \text{ mm}$ .

An FEI Quanta 200 3D SEM with a focussed ion beam (FIB) was used to mill a  $\sim 25 \mu\text{m}$  long TEM lamella,  $\sim 100 \text{ nm}$  thick, across an interdiffused particle-matrix region of the post-aged Ti-5553–25 wt.% TiFeMo composite [107].

Transmission electron microscopy (TEM) was performed using a JEOL JEM-2100F at 200 kV: selected area diffraction patterns (SADPs) with an aperture of 200 nm were taken from the Ti-5553, interdiffusion, and TiFeMo regions. A STEM-EDX map was performed on the Ti-5553 region of the TEM lamella.

### 7.3.6 $\beta$ grain size measurements

Measurements of the  $\beta$  grain size were made for the post-FAST Ti-5553 specimens (30 and 60 min dwells) and the Ti-5553–10 wt.% TiFeMo and Ti-5553–25 wt.% TiFeMo composites, as described in Chapter 3.

### 7.3.7 Chemical analysis line scans

SEM-EDX (Energy-Dispersive X-Ray Spectroscopy) line point scans across the interdiffusion regions of the post-FAST and post-aged Ti-5553–25 wt.% TiFeMo composites were performed using a Philips XL30 FEG SEM, with an Oxford Instruments detector.

An SEM-EDX line point scan of the area adjacent to the TEM lamella was also performed in the same way, to ensure comparability with the other SEM-EDX results.

DICTRA, the diffusion module of Thermo-Calc 2017b, was used to model the diffusion in the post-FAST Ti-5553–25 wt.% TiFeMo specimen across the interdiffusion boundary: the dwell period of 60 min at 1200°C was modelled using the thermodynamic TTTI3 and mobility MOBTi1 databases [108].

### 7.3.8 Micro- and nanohardness testing

Microhardness testing was performed using a Struers DuraScan-70 G5 with a Vickers indenter and 4.905 N load, held for 15 s, averaging  $\sim 50$  measurements. All hardness testing was performed on flat polished specimen surfaces to reduce error in the measurements. A 95 % confidence interval was used to determine the error from the mean, Equation 3.2.

For nanohardness, a Bruker Hysitron TI premier nanoindenter with a Berkovitch indenter and 0.01 N load was used, averaging 3–7 measurements per position, in order to assess the hardness profiles in the Ti-5553–25 wt.% TiFeMo post-FAST and post-aged composites.



## 7.4 Results

### 7.4.1 Microstructural examination

The microstructures of the Ti-5553 and Ti-5553–TiFeMo composites were characterised by SEM in the post-FAST, post-compressed, and post-compressed, solution treated and aged conditions, Figure 7.2.

Full diffusion bonding between the Ti-5553 and TiFeMo particles was achieved for all conditions, Figure 7.2b, d, and e. In addition, Figure 7.3a shows that, following FAST, the  $\beta$  grains co-exist in the Ti-5553 matrix and the TiFeMo particle.

The post-FAST  $\beta$  grain size of the Ti-5553 specimen and Ti-5553–25 wt.% TiFeMo composite were found to be very similar, whereas the  $\beta$  grain size was larger for Ti-5553–10 wt.% TiFeMo, Figure 7.2a. This was due to the shorter FAST dwell time for Ti-5553; 30 min as opposed to 60 min, and ensured that any differences in the mechanical behaviour between the Ti-5553 and Ti-5553–25 wt.% TiFeMo composite in subsequent compression testing was not due to differences in their grain sizes, Table 7.3.

When compared to a Ti-5553 specimen produced at 60 min dwell, the Ti-5553–10 wt.% TiFeMo composite has a similar  $\beta$  grain size, while the grain size of the Ti-5553–25 wt.% TiFeMo composite is  $\sim 1/3$  smaller, Table 7.3.

### 7.4.2 Compression testing and microhardness

In the compressed Ti-5553–10 wt.% TiFeMo composite, Figure 7.2c and Figure 7.3b, microcracking of the TiFeMo particles was observed; however there was an absence of cracking for particles below  $\sim 100 \mu\text{m}$ . Because of this, further refinement of the TiFeMo particle size was made for the Ti-5553–25 wt.% TiFeMo composite (Table 3.1), where cracking was limited to TiFeMo particles containing a high concentration of Fe-rich particles.

Adjacent to the Fe-rich prior interdendritic particles, there were also infrequent micron-sized B2 TiFe intermetallics in the composites as per [101], Figure 7.4.

In order to evaluate the mechanical properties of the specimens, compression testing and microhardness tests were performed, Figure 7.5.

Table 7.3: Mean  $\beta$  grain size of Ti-5553 (30 and 60 min FAST dwell) and Ti-5553–TiFeMo composites (60 min dwell) ( $\mu\text{m}$ )

<b>Ti-5553 30 min</b>	<b>Ti-5553 60 min</b>	<b>Ti-5553–10 wt.% TiFeMo</b>	<b>Ti-5553–25 wt.% TiFeMo</b>
125 $\pm$ 10	174 $\pm$ 33	177 $\pm$ 33	117 $\pm$ 10

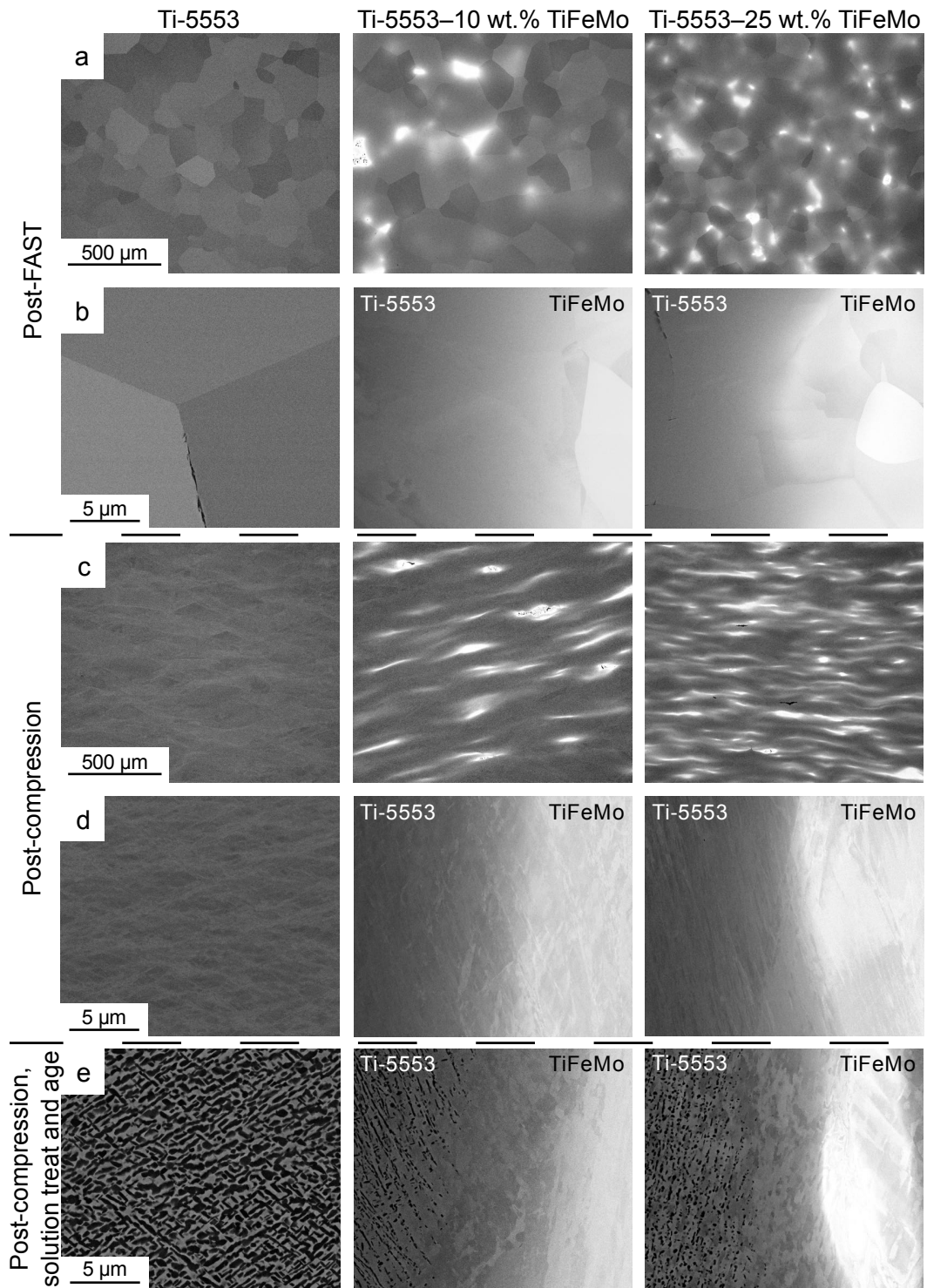


Figure 7.2: Low magnification BSEI micrographs of Ti-5553 (30 min dwell) and Ti-5553–TiFeMo composites: (a) post-FAST and (c) post-compression. High magnification BSEI micrographs of Ti-5553 (30 min dwell) and Ti-5553–TiFeMo composites: (b) post-FAST; (d) post-compression; and (e) post-compression, solution treat and age

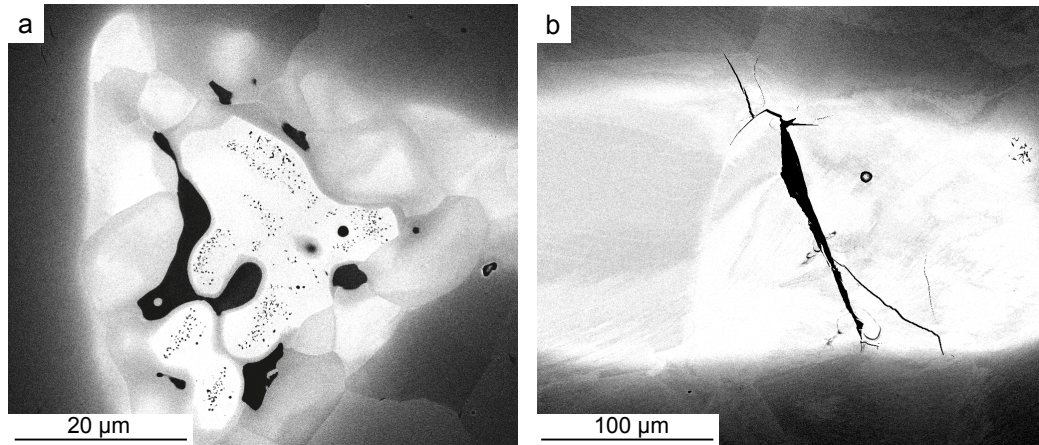


Figure 7.3: BSEI micrographs of a (a) TiFeMo particle (white) surrounded by the Ti-5553 matrix (dark grey).  $\beta$  grains can be seen to co-exist in the Ti-5553 and TiFeMo, and (b) a microcrack in a TiFeMo particle larger than 100  $\mu\text{m}$ , in the Ti-5553–10 wt.% TiFeMo compressed specimen

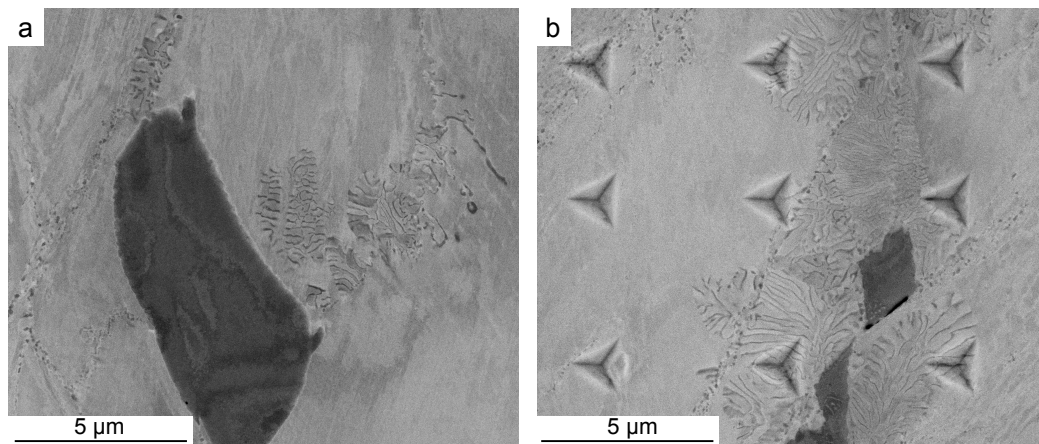


Figure 7.4: BSEI micrographs of the Ti-5553–25 wt.% TiFeMo post-aged composite, showing: (a) and (b) the infrequent dark nano-scale B2 TiFe intermetallic precipitates present adjacent to dark micron-sized Fe-rich prior interdendritic particles in the TiFeMo particles, and (b) the nanoindentations within the TiFeMo particle in Figure 7.6e in higher resolution

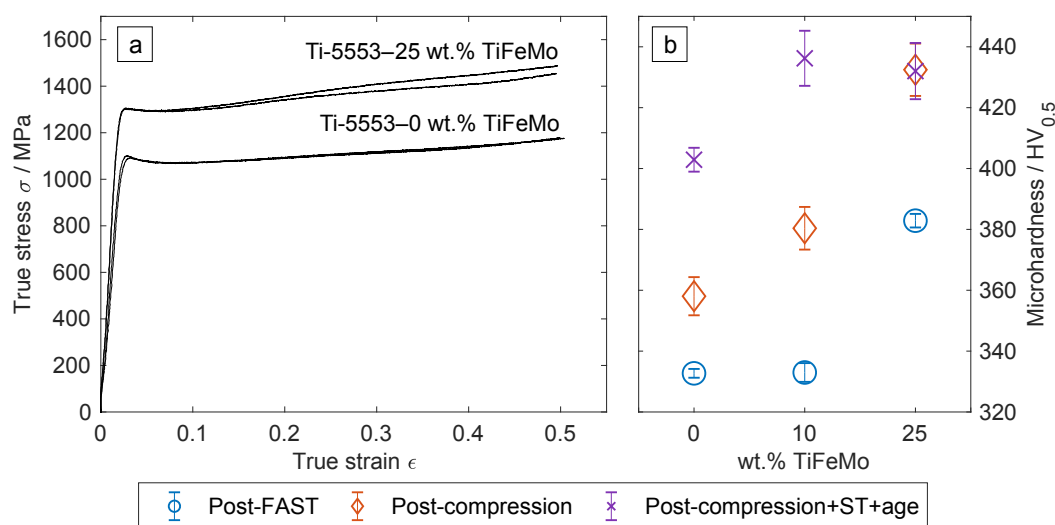


Figure 7.5: Mechanical properties: (a) Flow curves of Ti-5553 (i.e. 0 wt.% TiFeMo, 30 min dwell) and Ti-5553–25 wt.% TiFeMo specimens compressed at room temperature, and (b) microhardness for all compositions and conditions: post-FAST; post-compression; and post-compression, solution treat and age

The addition of 25 wt.% TiFeMo particles to Ti-5553 produced a  $>200$  MPa increase in compressive yield strength, which equates to an increase of  $\sim 18$  %.

The microhardness measurements showed a general trend of increasing microhardness with TiFeMo particle addition, as well as with compression and ageing.

### 7.4.3 Interdiffusion region analysis

DICTRA thermodynamic modelling was used to predict the interdiffusion of elements between the Ti-5553 and TiFeMo regions during FAST in the Ti-5553–25 wt.% TiFeMo composite, Figure 7.6a.

This prediction was in good agreement with an SEM-EDX line point scan performed across the interdiffusion region in the post-FAST condition, shown in Figure 7.6b.

Following compression, solution heat treatment and ageing, the interdiffusion profile was found to have changed minimally, owing to the reduced diffusion kinetics at the relatively low solution treat and age temperatures employed, Figures 7.6c and f. In particular, both Mo and Fe were seen to have diffused significantly into the prior Ti-5553 matrix, resulting in an increase in Mo and Fe compared to the nominal Ti-5553 composition, as well as a corresponding depletion of these elements in the prior TiFeMo particles.

The SEM-EDX line point scan of the Ti-5553–25 wt.% TiFeMo post-aged composite was performed on a TiFeMo particle containing a bcc + B2 TiFe microstructure, Figures 7.6e and f, which is shown in higher resolution in Figure 7.4b. The predominant microstructure observed

in the TiFeMo particles, however, was that of the A2 Ti, Mo phase, Figure 7.2e.

A substantial increase in nanohardness of  $\sim 2$  GPa was observed to be strongly correlated to the Fe and Mo content in both the post-FAST and post-aged conditions, Figures 7.6c, d, and f. Upon ageing, an increase in the nanohardness of  $\sim 1$  GPa was achieved in the prior Ti-5553 regions, alongside a  $\sim 0.5$  GPa increase in the prior TiFeMo particles.

#### 7.4.4 TEM lamella analysis

In order to investigate the basis for the increase in nanohardness with composition, a TEM lamella was prepared across the interdiffusion region between Ti-5553 and TiFeMo in the Ti-5553–25 wt.% TiFeMo post-aged composite, Figure 7.7a.

Here the diffusion of Fe and Mo from the prior TiFeMo particle into the Ti-5553 matrix could again be seen in an SEM-EDX line point scan of the area adjacent to the TEM lamella, Figure 7.7b.

The prior Ti-5553 region was found to contain  $\alpha$ , as demonstrated by STEM-EDX mapping in Figure 7.8. It was therefore inferred that the additional reflections in the SADP in Figure 7.7ci were caused by the presence of the  $\alpha$  phase.

All  $\beta$  regions were found to contain  $\omega$  or an  $\omega$  variant phase, as shown by the SADPs in Figures 7.7ci, iii, and vi [109].  $\omega$  was found to co-exist in the  $\beta$  phase with  $\alpha$  in the prior Ti-5553 region, Figure 7.7ci [110].

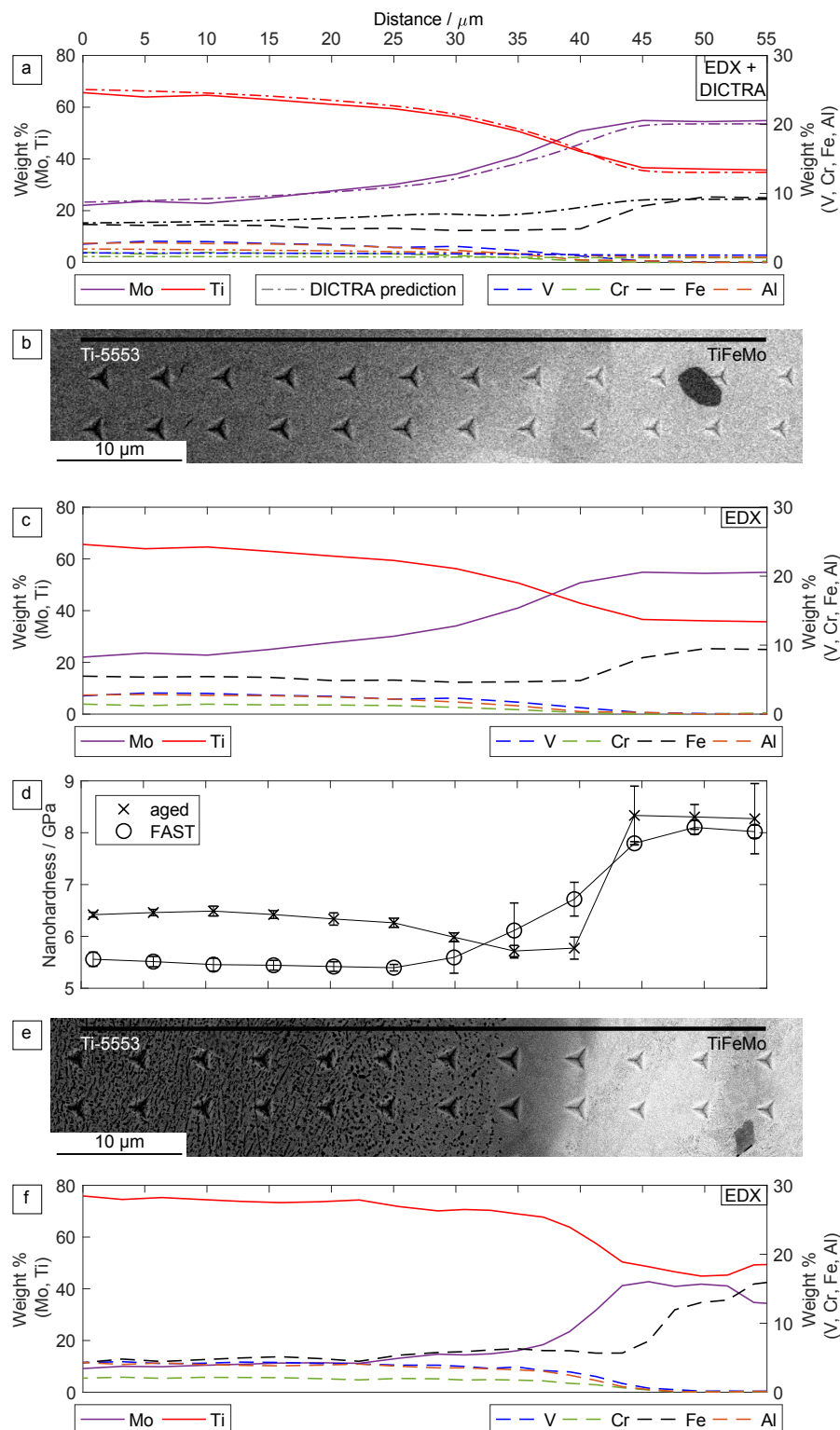


Figure 7.6: Interdiffusion region of Ti-5553–25 wt.% TiFeMo post-FAST composite: (a) DICTRA thermodynamic prediction with SEM-EDX line point scan, (b) BSEI micrograph, and (c) associated SEM-EDX line point scan. (d) nanohardness for both Ti-5553–25 wt.% TiFeMo post-FAST and post-aged composites, corresponding to indents shown in (b) and (e). Interdiffusion region of Ti-5553–25 wt.% TiFeMo post-aged composite: (e) BSEI micrograph, and (f) associated SEM-EDX line point scan. The black lines show the approximate location of the SEM-EDX line point scans. For all subfigures the Ti-5553 region is on the left and TiFeMo region is on the right



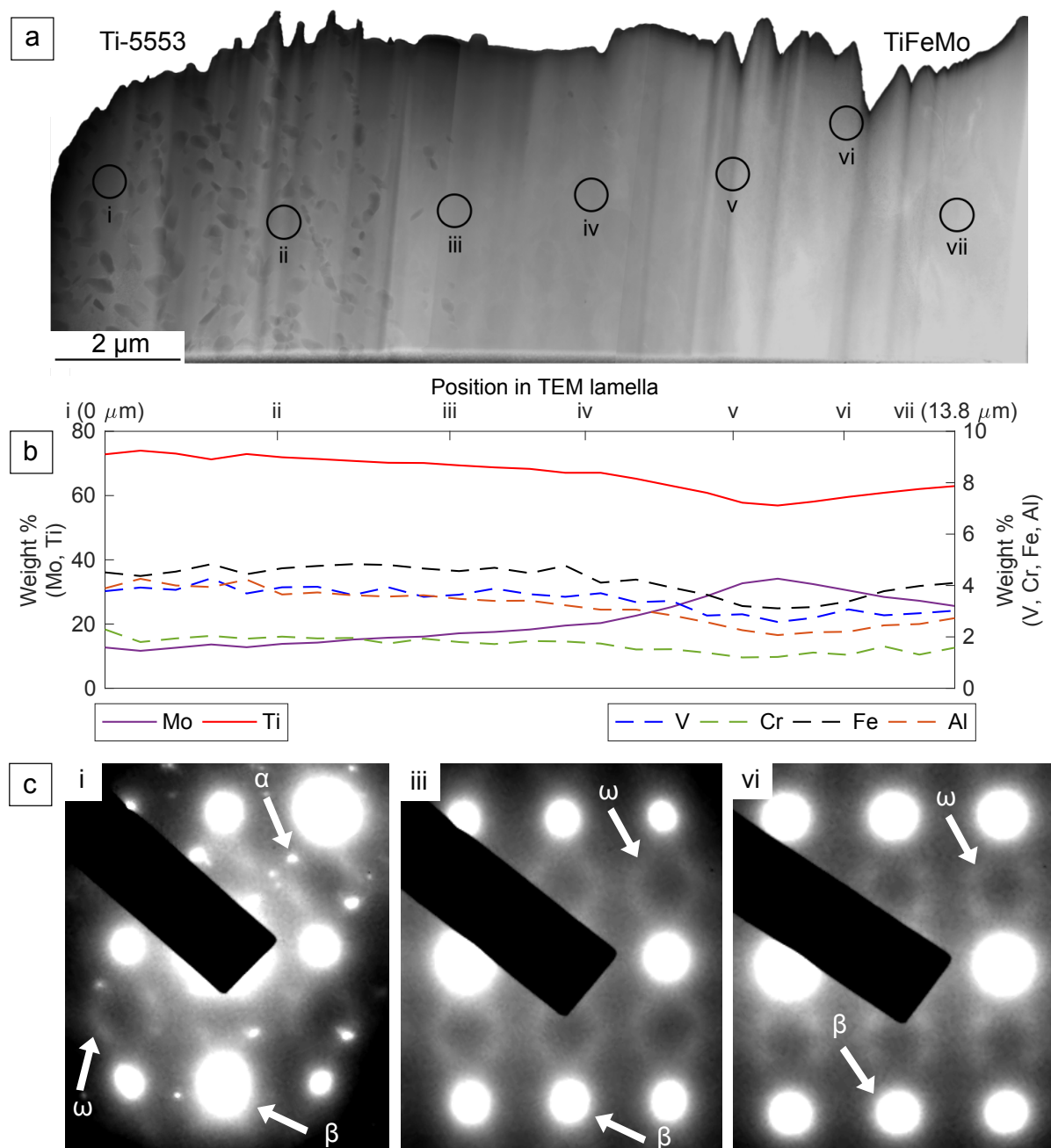


Figure 7.7: TEM lamella of the interdiffusion region in the Ti-5553–25 wt.% TiFeMo post-aged composite: (a) STEM-HAADF (high-angle annular dark-field) overview, (b) SEM-EDX line point scan of the area adjacent to the TEM lamella at points i - vii, and (c) SADPs from regions; i - overlapping bcc  $\beta$ , hcp  $\alpha$ , and  $\omega$  reflections, iii - bcc  $\beta$  and Ti-5553/TiMo type  $\omega$  reflections, and vi - bcc  $\beta$  and TiFeMo  $\omega$  variant reflections ( $[110]_{\text{bcc}}$  zone axis)

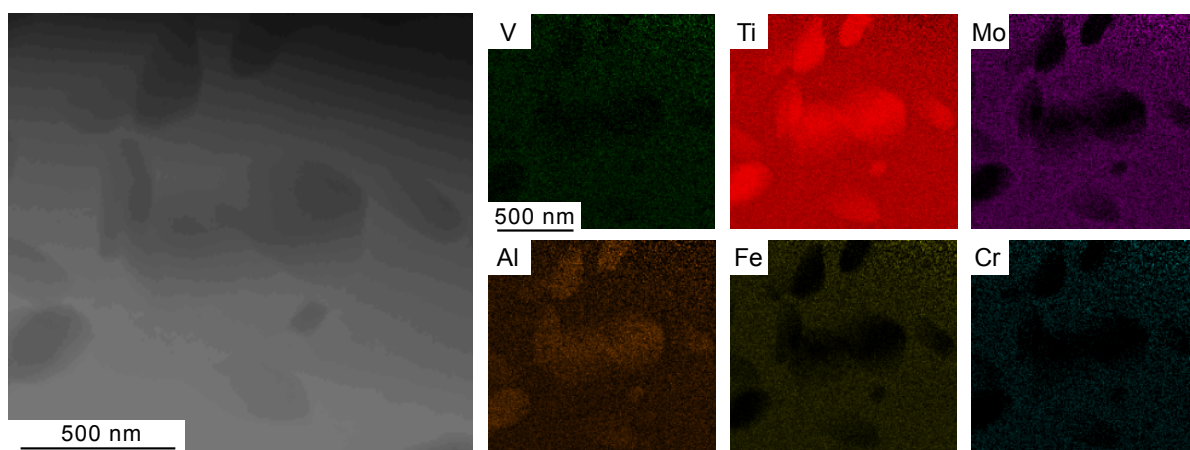


Figure 7.8: STEM-EDX map of the Ti-5553 region of the TEM lamella, indicating the presence of the  $\alpha$  phase. Areas high in Ti and Al indicate the presence of  $\alpha$  phase, whereas areas high in Fe, Cr, V, and Mo indicate the presence of  $\beta$  phase



## 7.5 Discussion

### 7.5.1 Microstructural examination and microhardness testing

As shown in Figures 7.2b, d, and e, there is full diffusion bonding between the Ti-5553 matrix and TiFeMo particles. This is significant as delamination and de-bonding between the matrix and the reinforcement media is a major cause of reinforcement failure, such as that which occurred for Grützner et al. and Qin et al. for TiB/TiC in Ti-5553 and Ti-6242, respectively [98, 111].

Figure 7.3a shows that the Ti-5553 and TiFeMo particles share  $\beta$  grains following FAST. It is not uncommon for composites to have a matrix and reinforcement particles which share the same crystal structure, in this case bcc  $\beta$  Ti-5553 and bcc  $\beta$  Ti, Mo; however it is very unusual for  $\beta$  grains to co-exist within both, as this signifies that they also share the same crystallographic orientation [112]. This enabled dislocations to easily transfer from the matrix to the particles, as there is no grain boundary to impede dislocation movement [12].

Figure 7.5a shows the comparison between the flow stresses of the Ti-5553 specimen (30 min dwell) and Ti-5553–25 wt.% TiFeMo composite which were compressed at room temperature. Addition of 25 wt.% TiFeMo particles produced a  $>200$  MPa increase in compressive yield strength, from 1100 to 1300 MPa, which equates to an increase of  $\sim 18$  %. As the  $\beta$  grain size post-FAST was found to be comparable for the Ti-5553 specimen (30 min dwell) and Ti-5553–25 wt.% TiFeMo composite, Table 7.3, this increase in strength was not due to Hall-Petch strengthening (grain refinement), and was therefore directly attributed to the influence of the TiFeMo particles. Despite the increase in strength, there appears to be minimal change in ductility and all compressed specimens were strained to 0.5 without failure occurring. This may be due to the matrix and particles' shared  $\beta$  grains, which allowed the load to be transferred to the higher strength TiFeMo particles.

Table 7.3 shows that the addition of 10 wt.% TiFeMo particles had limited effect on the  $\beta$  grain size, whereas 25 wt.% TiFeMo addition reduced the  $\beta$  grain size by  $\sim 1/3$ . This is likely due to the improved particle grinding method for the 25 wt.% TiFeMo particles, which produced smaller, more uniformly sized, and more homogeneously distributed particles within the Ti-5553 matrix, which more successfully pinned the grain boundaries [113]. Reduced grain size has the advantage of increasing both the strength and ductility, as described by the Hall-Petch equation [12].

This effect explains the microhardness results seen in Figure 7.5b: the unreinforced Ti-5553 specimen and Ti-5553–10 wt.% TiFeMo composite have very similar microhardness values post-FAST, whereas the Ti-5553–25 wt.% TiFeMo composite has a value  $\sim 50$  HV greater.

### 7.5.2 Interdiffusion region analysis

Mo and Fe were found to significantly diffuse into the prior Ti-5553 matrix in both the post-FAST and post-aged Ti-5553–25 wt.% TiFeMo composites, shown in Figures 7.6c, 7.6f, and 7.7b, partly as a result of the high temperature of FAST processing (1200°C) and extended time at the ageing temperature (8 h). The fact that both TiFeMo and Ti-5553 contain the bcc  $\beta$  phase, throughout which diffusion of alloying elements is approximately three orders of magnitude faster than the  $\alpha$  phase, greatly contributed to the extent of the Mo and Fe diffusion [13].

This increased content, particularly of Mo, led to reduced formation of  $\alpha$  within the interdiffusion region, as seen in Figures 7.6e and f, as Mo and Fe both stabilise the  $\beta$  phase [13]. SADPs performed at various regions of the TEM lamella, Figures 7.7a and c, corroborated this observation as only the  $\beta$  and  $\omega$  phases were found in the interdiffusion and TiFeMo regions (Figures 7.7ciii and vi). STEM-EDX mapping of the prior Ti-5553 region, Figure 7.8, shows that the darker areas of the microstructure contain higher amounts of Al (an  $\alpha$  stabiliser) and Ti, indicative of  $\alpha$  phase being present, while the lighter areas contain higher amounts of Fe, Mo, Cr, and V ( $\beta$  stabilisers) which is indicative of  $\beta$  phase being present. This suggests that  $\alpha$  phase was present in the prior Ti-5553 region of the TEM lamella. The additional reflections shown in Figure 7.7ci were therefore assumed to be  $\alpha$  phase, as they are similar to the reflections shown in the SADP in Figure 7.1c (which had a similar ageing temperature and duration).

The TiFeMo particle in the post-aged Ti-5553–25 wt.% TiFeMo composite, analysed in Figure 7.6, has a bcc + B2 TiFe microstructure, shown in higher resolution in Figure 7.4b. These B2 TiFe intermetallics are as observed previously for TiFeMo alloys [101]: it was anticipated that the TiFeMo particles would be reinforced by both  $\omega$  phase [32] and B2 TiFe intermetallics, as seen by Knowles et al. [101]. The majority of TiFeMo particles, however, appeared to be single phase A2 Ti, Mo when imaged by SEM, Figure 7.2e. This observation was confirmed when such a particle was analysed by a STEM-EDX line scan in Figure 7.7b, and was found to be highly depleted in Fe, potentially owing to Fe's fast diffusion rates in  $\beta$  titanium [13]. Therefore, Fe and Mo diffusion away from the prior TiFeMo particles resulted in these regions being depleted in Fe, which prevented the formation of the B2 TiFe intermetallics, as well as destabilising the formation of  $\alpha$  phase in the interdiffusion region.

Ageing of the Ti-5553–25 wt.% TiFeMo composite produced a nanohardness increase of  $\sim 1$  GPa and  $\sim 0.5$  GPa in the prior Ti-5553 region and prior TiFeMo particle, respectively, Figure 7.6d. This strengthening of the prior Ti-5553 region may predominantly be due to the secondary  $\alpha$  phase formed during the ageing heat treatment, Figures 7.6b and e [22]. The formation of infrequent B2 TiFe intermetallics upon ageing, which can be seen in some of the

nanoindentations in Figure 7.4b, could be responsible for the slight strengthening in the prior TiFeMo particle. There is also a substantial nanohardness increase of  $\sim 2$  GPa with the increase in Fe and Mo content from the prior Ti-5553 matrix to the prior TiFeMo particle, for both the post-FAST and post-aged composites. This indicates that neither B2 TiFe intermetallics nor  $\alpha$  phase were the dominant strengthening phase in the prior TiFeMo particles and interdiffusion region. To investigate further the strengthening mechanism, a TEM lamella was made from a typical A2 Ti, Mo-containing TiFeMo particle.

All  $\beta$  regions of the TEM lamella were found to contain  $\omega$  or an  $\omega$  variant phase, as shown by the SADPs in Figures 7.7ci, iii, and vi. It was found that the structure changed from that of streaked diffuse  $\omega$  observed in Ti-5553 [33, 95] and Ti-Mo [114] to that of a more distinct  $\omega$  variant reported for Ti-Fe and TiFeMo alloys [101, 115]. These changes appear similar to the changes for the  $\omega$  reflections shown in key diagrams in Figure 7.1, from the diffuse streaked  $\omega$  in Figure 7.1f to the more distinct sharp  $\omega$  in Figure 7.1g.

This, along with the increase in nanohardness shown in Figure 7.6d when comparing the prior Ti-5553 and prior TiFeMo regions, indicates that for the heat treatment applied, the regions containing the TiFeMo  $\omega$  variant provided more strengthening than that which existed in the prior Ti-5553 matrix.

### 7.5.3 Future applications

Severe macrosegregation can occur in Fe-rich alloys through conventional processing, creating ‘ $\beta$  flecks’, solute-rich areas with a different microstructure to that of the bulk, which are detrimental to fatigue strength [116].

This chapter has shown that it is possible for an Fe-rich alloy to act as reinforcement media for a  $\beta$  titanium alloy, Ti-5553, produced by FAST. Despite diffusion of Fe and Mo into the Ti-5553 matrix, high nanohardnesses across the interdiffusion region and increased bulk compressive yield strengths were achieved, without the formation of detrimental brittle phases, such as ‘ $\beta$  flecks’.

## 7.6 Conclusions

The success of the FAST-*forge* process for Ti-5553 led to an investigation into the possibility of producing a TiFeMo reinforced Ti-5553 composite by the FAST-*forge* process. The following conclusions can be drawn from this Chapter:

1. Ti-5553 composites reinforced with 10-25 wt.% of a high strength TiFeMo alloy have been fabricated with full diffusion bonding by field-assisted sintering technology (FAST).
2. The Ti-5553–25 wt.% TiFeMo composite demonstrated compressive yield strengths of 1300 MPa, >200 MPa more than that of unreinforced Ti-5553. The microhardness was 383 HV post-FAST, which was  $\sim 50$  HV higher than that of unreinforced Ti-5553, and which increased by  $\sim 50$  HV on compression, solution heat treatment, and ageing.
3. Characterisation of the interdiffusion regions between Ti-5553 and TiFeMo particles in the Ti-5553–25 wt.% TiFeMo post-FAST and post-aged composites by SEM, SEM-EDX, and nanoindentation showed that increased Fe and Mo content led to an increase in the nanohardness. However, this increase in Fe and Mo destabilised the  $\alpha$  phase formation and resulted in only infrequent formation of the B2 TiFe intermetallics.
4. TEM, STEM-HAADF, and SEM-EDX performed on a TiFeMo particle devoid of B2 TiFe intermetallics identified that  $\omega$  or an  $\omega$  variant formed throughout the post-aged Ti-5553–25 wt.% TiFeMo composite; and that the diffusion of Fe and Mo were correlated to a change in the  $\omega$  structure, from that of  $\omega$  phase in Ti-5553 to that of the  $\omega$  variant in TiFeMo, which corresponded to an increase in nanohardness.
5. FAST-*forge* of TiFeMo reinforced Ti-5553 has produced improved strength and microhardness, despite the strengthening B2 TiFe intermetallics not being present. This shows that FAST-*forge* can be used to produce higher strength titanium-titanium composites, which could not be produced by conventional processing methods.

## Chapter 8

# Conclusions

Throughout this thesis, it has been shown that FAST is an effective processing method for the consolidation of titanium alloy powders, both for single alloys and for multiple alloys in the form of titanium-titanium composites. The success of the scale-up of FAST to the industrial scale, and the subsequent thermomechanical processing and heat treatment has shown the capability of the FAST-*forg*e process to be a viable near-net shape titanium powder processing method.

### 8.1 Small-scale FAST of Ti-5553

The small-scale FAST testing performed in Chapter 4 has shown that the  $\beta$  grain size of Ti-5553 produced at temperatures above the  $\beta$  transus temperature can be controlled by the dwell temperature and dwell time. This is very important, as the final microstructure, and therefore mechanical properties, of Ti-5553 are very dependent on the  $\beta$  grain size prior to thermomechanical processing. The conventional process does not allow for this level of control over the  $\beta$  grain size, which shows the advantage of using FAST.

The dwell temperature had a significant effect on the  $\beta$  grain size, with higher temperatures producing larger grain sizes due to the larger driving force for grain growth. The porosity was found to reduce significantly at higher temperatures, but only at the lower dwell times (3 and 10 min). At dwell times of 30 min and above, the porosity was found to be unaffected by increasing temperature (for temperatures close to, or above the  $\beta$  transus, 850–1200°C). The specimens produced at 800°C by FAST showed much higher porosities, due to the large  $\alpha$  phase volume fraction. The  $\alpha$  phase impeded the removal of porosity during FAST, owing to slower diffusion rates in the  $\alpha$  phase compared with the  $\beta$  phase.

The dwell time had a mixed effect on the  $\beta$  grain size, depending on the dwell temperature. At some dwell temperatures, 900–970°C, the increase in dwell time from 10 to 30 min produced a

large increase in grain size, whereas the increase from 30 to 60 min showed minimal difference in grain size. At other temperatures, 1000–1200°C, the trends were reversed. The only consistent relationship was between dwell times of 3–10 min, which showed extensive grain growth with the increase in dwell time. In general, however, the dwell time had less of an effect on the grain size than the dwell temperature. Densities between 99.5 and 100 % were possible for all dwell temperatures at dwell times of 30 min and above. The complicated relationships between the  $\beta$  grain size and the dwell time are likely to be linked to the changing level of porosity, and its effect on the grain size.

## 8.2 Large-scale FAST of Ti-5553

Based on the results of the small-scale FAST testing in Chapter 4, large-scale FAST testing was performed on Ti-5553, along with a subsequent compression testing study, compression testing and heat treatment study, and a large-scale forging and heat treatment study in Chapter 5.

Large-scale FAST produced Ti-5553 billets which were close to fully dense. The post-FAST microstructure varied from that of the small-scale FAST testing due to the large difference in cooling rate (250°C/min at the small and 14°C/min at the large-scale). This slow cooling allowed fine-scale  $\alpha$  phase to precipitate at the grain boundaries and within the grains in the large-scale FAST specimens produced above the  $\beta$  transus (at 930 and 1000°C). The microstructure produced was very similar to that of conventionally  $\beta$  forged Ti-5553, and had microhardness values of 436–446 HV. It showed no indication of the prior powder structure once it had been processed by FAST, and retained the fine  $\beta$  grain size of the powder.

The compression testing study of the 930 and 1000°C post-FAST material has produced flow curves very similar to those of conventionally produced  $\beta$  forged Ti-5553, and the flow curves are relatively consistent despite different FAST temperatures of 850, 930, and 1000°C. The main difference between the 850°C, and 930 and 1000°C post-FAST specimens is the degree of flow softening during compression testing, due to the presence of fine acicular  $\alpha$  at 930 and 1000°C. The acicular  $\alpha$  was broken up and spheroidised as strain increased, leading to extensive flow softening, whereas at 850°C the primary  $\alpha$  grains showed only slight deformation perpendicular to the compression direction. Sub-grains were found in the  $\beta$  phase in all compressed specimens, but were especially prominent at higher strain rates. The increased work hardening rate at higher strain rates resulted in an increase in the dislocation density, due to which the dislocations rearranged into the lowest energy formation,  $\beta$  sub-grains.

Double truncated cones were also compressed at a single temperature and strain rate (785°C and 0.1 s<sup>-1</sup>) to conduct a heat treatment study, with the cone providing a large variation in

strain from centre to edge (perpendicular to the compression axis). Various temperatures (400–600°C) and times (2–8 h) were used to determine the effect on the microstructure. However, due to the solution heat treatment producing a large primary  $\alpha$  volume fraction in the specimens produced by FAST at 930 and 1000°C, minimal secondary  $\alpha$  was able to precipitate out during ageing, leading to very similar microhardness results. Some secondary  $\alpha$  was able to precipitate out in the specimen produced by FAST at 850°C, which gave rise to a more typical Ti-5553 solution treated and aged microstructure, and increased the microhardness beyond that of the post-FAST and post-compressed specimens.

Large-scale industrial forging and heat treatment of Ti-5553 produced by FAST has resulted in microstructures similar to those of conventionally produced Ti-5553, despite taking only three processing steps (far fewer than for the conventional process shown in Figure 1.1), as shown in Figure 5.14. The forged microstructures of specimens produced by FAST were shown to vary with forging temperature and level of strain, whereas only slight variations were seen in the heat treated microstructure, even at higher resolution in TEM. Microhardness measurements of the heat treated specimens also found that different forging temperatures and levels of strain had minimal effect on the microhardness values, with averages of between 410 and 417 HV for different forging temperatures measured. These have been shown to be higher than that of conventionally produced Ti-5553 which has undergone the same heat treatment, 385 and 405 HV [84]. It is important to note that there is also no indication in the material flow or microhardness data that the heat treated material originates from powder rather than conventional billet.

Overall, the results in Chapter 5 have shown that the FAST-*forge* process is capable of producing forged and heat treated Ti-5553 microstructures, microhardness values, and flow behaviour similar to that of conventional processing, while significantly reducing the number of processing steps.

### 8.3 Microstructural prediction of Ti-5553 produced by FAST-*forge*

The Bate-Brooks method has been used to relate a structure-related internal variable,  $\lambda$ , to the flow curves of Ti-5553 produced by FAST (at 930 and 1000°C), generated in Chapter 5.  $\lambda$  was then related to various microstructural features, so that the microstructure could be predicted from the flow stress.

In Chapter 6 the predicted flow curves calculated by the Bate-Brooks method were found

to produce similar flow softening behaviour and steady state stress values, when compared to the measured flow curves for compression specimens produced by FAST at 930 and 1000°C.

Significant relationships were found between the mean feret minimum and median  $\alpha$  area and  $\lambda$ , for all strain rates and temperatures. The mean feret minimum and median  $\alpha$  area both decreased as  $\lambda$  increased which roughly corresponded to an increase in strain rate, due to increased break-up and spherodisation of  $\alpha$  laths. These relationships are particularly useful as they are independent of strain rate and temperature, and therefore can be used for forging where the strain rate or temperature is not easily controlled or is not consistent within the forging, such as multi-hit closed-die forging. Significant relationships were found between the aspect ratio of the feret maximum to feret minimum and  $\lambda$  for each strain rate. The aspect ratio decreased as  $\lambda$  decreased due to an increase in strain, which caused break-up and spherodisation of the  $\alpha$  laths.

It was desired that by the end of this project, there would be a complex Ti-5553 component produced by FAST and forged on a scale comparable to that of landing gear components. That has been achieved in Chapter 6, where a complex near-net shape forging, an ‘eye bolt’, was produced with no cracking, despite minimal control over strain rate and temperature, and was evaluated using data generated by smaller-scale compression testing.

The microstructure of the ‘eye bolt’ specimen was taken at seven positions, which were correlated to positions in the FEM simulation to give the strain. As the strain increased from P1–P7 (from the edge to the centre of the forging), the  $\alpha$  laths became more spherodised and broken up, and more aligned with the perpendicular of the forging direction. P6 and P7 experienced the highest strains and strain rates, and as such contained a lower  $\alpha$  phase volume fraction and the most spherodised  $\alpha$  phase.

The relationships between the mean feret minimum and median  $\alpha$  area and  $\lambda$  were used to predict the strain rate and temperature at seven positions within the ‘eye bolt’ forged specimen. The temperatures could be roughly predicted from the microstructure and allowed ranges to be calculated for the strain rates. Strain rates were found to generally correlate with the microstructural observations made.

There were similarities between the microstructure found in the ‘eye bolt’ specimen and that of the compressed and forged double truncated cones in Chapter 5. The  $\alpha$  laths were similar in size and morphology for an equivalent level of strain to those of the cone specimen forged at 810°C, implying that the ‘eye bolt’ was forged at around that temperature.  $\beta$  sub-grains were also seen in both specimens, although they were more prominent in the high strain regions of the ‘eye bolt’ specimen than the high strain regions of the cones, implying that the strain rate



was higher than  $3 \text{ s}^{-1}$  (that of the forged cones) in the ‘eye bolt’ specimen.

## 8.4 Ti-5553–TiFeMo composites produced by FAST-*forge*

The success of the application of the FAST-*forge* process to Ti-5553 led to an investigation into the strengthening of Ti-5553 by high strength TiFeMo particles using FAST.

The powders were mixed together to produce a Ti-5553 matrix interspersed with 10–25 wt.% TiFeMo particles, and full diffusion bonding was achieved following FAST. The existence of a shared phase, the bcc  $\beta$  phase, meant that there was very good coherency between the two alloys.

Room temperature compression testing of the Ti-5553–25 wt.% TiFeMo composite demonstrated compressive yield strengths of 1300 MPa, >200 MPa more than that of unreinforced Ti-5553.

The microhardness was also found to increase, with values of 383 HV post-FAST, which was  $\sim 50$  HV higher than that of unreinforced Ti-5553. The microhardness also increased by  $\sim 50$  HV on compression, solution heat treatment, and ageing.

The interdiffusion region between the Ti-5553 and TiFeMo particles in the Ti-5553–25 wt.% TiFeMo specimen was investigated in the post-FAST and post-aged conditions. Chemical analysis and nanoindentation across the interdiffusion region showed that there was an increase in Fe and Mo towards the TiFeMo particles, with a corresponding increase in the nanohardness. However, this increase in Fe and Mo destabilised the  $\alpha$  phase formation in the Ti-5553 region and resulted in only infrequent formation of the B2 TiFe intermetallics in the TiFeMo region. The microstructure of the TiFeMo particles was found to be mainly the A2 Ti, Mo phase, so it did not benefit from the high strength nanoscale B2 TiFe intermetallics.

Upon ageing the nanohardness was found to increase in both the Ti-5553 and TiFeMo regions of the interdiffusion region, and further analysis was performed to identify the strengthening mechanism. The interdiffusion region between a typical TiFeMo particle and the Ti-5553 matrix in the post-aged Ti-5553–25 wt.% TiFeMo composite was analysed by TEM, STEM-HAADF, and chemical analysis.  $\omega$  phase was observed in the Ti-5553 region, and an  $\omega$  phase variant, found in TiFeMo previously, was observed in the TiFeMo region. The diffusion of Fe and Mo were found to correlate to the change in the  $\omega$  structure, from that of  $\omega$  phase in Ti-5553 to that of the  $\omega$  variant in TiFeMo, which corresponded to an increase in nanohardness.

## Chapter 9

# Future Work

There are numerous ways in which the work in this thesis can be furthered. The main issue to be addressed is the expense of the starting powder used in this thesis. The Ti-5553 provided by Safran Landing Systems was an off-cut of a forged landing gear, which was then gas atomised to produce the spherical powder used in this thesis. The aim was to establish the effectiveness of the FAST-*forge* process for a commercial metastable  $\beta$  titanium alloy, with the view that a metastable  $\beta$  alloy produced by a low-cost process could be substituted in the future, in order to produce it at reduced cost.

The main items to be investigated in the future are listed below.

1. The FAST-*forge* process could be implemented with a low-cost particulate feedstock, such as that produced by the Metalysis (FFC) process, to reduce the cost of titanium alloy production. If a new  $\beta$  titanium alloy could be manufactured by this method, the work in this thesis could be used as a guideline for the processing using the FAST-*forge* process.
2. The flexibility of the FAST-*forge* process means that different alloy powders can be used in different regions to provide optimum mechanical properties in each region. Some work on this topic has already been performed with positive results, for combinations of Ti-5553 with cp-Ti, Ti-5553 with Ti-64, and Ti-64 with cp-Ti [117]. When compared to welding, FAST-*forge* provides a stronger diffusion bond as the powders have been sintered together and have consistent microstructure. There is no heat affected zone (HAZ) as is commonly found in welding, so there is no region with a differing microstructure that could act as a point of weakness.
3. The FAST process is very flexible with regard to the powder morphology. Large size fractions of gas atomised powder produce optimum density due to better packing, which allows un-sieved powder to be used at reduced cost. Waste material from the additive

manufacturing process, in the form of spherodised gas atomised powder of an incorrect particle size, can also be used in the FAST-*forg*e process to reduce the cost. Angular powders such as HDH powders can be used with minimal difference to gas atomised spherical powders [64]. This means that swarf could be used as a feedstock to make use of the expensive waste from titanium alloy products, as machining can remove as much as 90 % of the original material.

4. In this thesis, only cylindrical FAST specimens were produced. However, shaped FAST moulds could be used to produce near-net shape components which would reduce the amount of material that needed to be removed by machining. Some work on this has already been performed by Weston et al. and has yielded positive results [4].
5. More substantial mechanical testing, such as fatigue and tensile tests, would be required on Ti-5553 produced by FAST in the future, in order to establish whether the process produces similar mechanical properties to that of conventionally produced material. Given that bi-modal microstructure has been produced for the forged and heat treated Ti-5553 produced by FAST in this thesis, which is very similar to the currently used microstructures with adequate fatigue and tensile properties, this seems likely (see Figure 5.14).
6. Further heat treatment regimes should be investigated to optimise the heat treatment for Ti-5553 produced by FAST, as this will produce the optimum properties for fatigue, tensile strength, and fracture toughness which are required for landing gear components.
7. Following on from the work in Chapter 7, there is an obvious set of future work which includes the production of other multiple alloy components. This ability to produce multiple-alloy systems from powder is one of the main advantages of the FAST-*forg*e process, as it is very difficult to achieve by other methods. Some work has been completed before where ceramic particles have been embedded in titanium alloys, but the work in this thesis is the first time the process has been used to strengthen a titanium alloy with another titanium alloy, and it eliminates some of the issues found with bonding between ceramic particles and a titanium matrix.
8. The work in Chapter 7 also demonstrates the opportunity to use FAST to produce Fe-rich titanium alloy particles (as a strengthening media) in the matrix of a different titanium alloy. There are issues with the use of Fe in titanium alloys, despite its ability to strengthen titanium, due to macrosegregation which occur during melting in conventional processing (VAR). As there is no melting involved in the FAST-*forg*e process, there is reduced risk of macrosegregation of Fe in the final product.

## Chapter 10

# Appendix

Finite increment theory was employed to work out  $\Delta\lambda$ .

$$\begin{aligned}\frac{\partial\lambda}{\partial\varepsilon} &= \alpha(\lambda_{ss} - \lambda) \\ \text{Let } Y &= \lambda - \lambda_{ss} \\ \frac{\partial\lambda}{\partial\varepsilon} &= -\alpha Y\end{aligned}\tag{10.1}$$

Integration of Eq. 10.1 gives:

$$\begin{aligned}Y &= \exp(-\alpha\varepsilon) \\ \lambda &= \lambda_{ss} + \exp(-\alpha\varepsilon)\end{aligned}\tag{10.2}$$

For  $\Delta\lambda \rightarrow \Delta\varepsilon$ , and according to the finite increment theorem:

$$\lambda(\varepsilon + \Delta\varepsilon) = \Delta\lambda + \lambda(\varepsilon)\tag{10.3}$$

Where  $\lambda(\varepsilon) \equiv \lambda$  in previous equations

Eq. 10.2 for  $\varepsilon + \Delta\varepsilon$  gives:

$$\begin{aligned}\lambda(\varepsilon + \Delta\varepsilon) &= \lambda_{ss} + \exp(-\alpha(\varepsilon + \Delta\varepsilon)) \\ \lambda(\varepsilon + \Delta\varepsilon) &= \lambda_{ss} + \exp(-\alpha\varepsilon) \exp(-\alpha\Delta\varepsilon)\end{aligned}\tag{10.4}$$

Rearrangement of Eq. 10.2 and substitution into Eq. 10.4 gives:

$$\lambda(\varepsilon + \Delta\varepsilon) = \lambda_{ss} + [\lambda(\varepsilon) - \lambda_{ss}] \exp(-\alpha\Delta\varepsilon)\tag{10.5}$$

Substitution of Eq. 10.5 into Eq. 10.3 and rearrangement to get  $\Delta\lambda$  gives:

$$\Delta\lambda = \lambda_{ss} + [\lambda(\varepsilon) - \lambda_{ss}] \exp(-\alpha\Delta\varepsilon) - \lambda(\varepsilon) \quad (10.6)$$

Substitution of Eq. 10.2 into Eq. 10.6 gives:

$$\begin{aligned} \Delta\lambda &= \lambda_{ss} + [\lambda(\varepsilon) - \lambda_{ss}] \exp(-\alpha\Delta\varepsilon) - [\lambda_{ss} + \exp(-\alpha\varepsilon)] \\ \Delta\lambda &= [\lambda(\varepsilon) - \lambda_{ss}] \exp(-\alpha\Delta\varepsilon) - \exp(-\alpha\varepsilon) \end{aligned} \quad (10.7)$$

Rearrangement of Eq. 10.2 and substitution into Eq. 10.7 gives:

$$\begin{aligned} \Delta\lambda &= [\lambda(\varepsilon) - \lambda_{ss}] \exp(-\alpha\Delta\varepsilon) - [\lambda(\varepsilon) - \lambda_{ss}] \\ \Delta\lambda &= [\lambda(\varepsilon) - \lambda_{ss}] [\exp(-\alpha\Delta\varepsilon) - 1] \end{aligned} \quad (10.8)$$

## 10.1 Rights and Permissions

Chapters 4, 5, 7 contain results which have been previously published in Key Engineering Materials conference proceedings [5], Journal of Materials Processing Technology [6], and Scripta Materialia [7].

Permissions have been acquired to re-use the contents of these papers in this thesis.




The screenshot shows the RightsLink interface for a document. On the left is a thumbnail of the journal cover. To its right, the following metadata is displayed:

- Title:** Thermomechanical processing of a high strength metastable beta titanium alloy powder, consolidated using the low-cost FAST-forge process
- Author:** Emma Calvert, Brad Wynne, Nick Weston, Adam Tudball, Martin Jackson
- Publication:** Journal of Materials Processing Technology
- Publisher:** Elsevier
- Date:** April 2018

Below the metadata, it states: "Crown Copyright © 2017 Published by Elsevier B.V. All rights reserved." On the right side of the interface, there is a "LOGIN" button and a text box that reads: "If you're a copyright.com user, you can login to RightsLink using your copyright.com credentials. Already a RightsLink user or want to learn more?" At the bottom of the interface are "BACK" and "CLOSE WINDOW" buttons.

Please note that, as the author of this Elsevier article, you retain the right to include it in a thesis or dissertation, provided it is not published commercially. Permission is not required, but please ensure that you reference the journal as the original source. For more information on this and on your other retained rights, please visit: <https://www.elsevier.com/about/our-business/policies/copyright#Author-rights>

Copyright © 2019 Copyright Clearance Center, Inc. All Rights Reserved. [Privacy statement](#). [Terms and Conditions](#). Comments? We would like to hear from you. E-mail us at [customer@copyright.com](mailto:customer@copyright.com)



The screenshot shows the RightsLink interface for a document. On the left is a thumbnail of the journal cover. To its right, the following metadata is displayed:

- Title:** Novel high strength titanium-titanium composites produced using field-assisted sintering technology (FAST)
- Author:** E.L. Calvert, A.J. Knowles, J.J. Pope, D. Dye, M. Jackson
- Publication:** Scripta Materialia
- Publisher:** Elsevier
- Date:** 15 January 2019

Below the metadata, it states: "© 2018 Acta Materialia Inc. Published by Elsevier Ltd." On the right side of the interface, there is a "LOGIN" button and a text box that reads: "If you're a copyright.com user, you can login to RightsLink using your copyright.com credentials. Already a RightsLink user or want to learn more?" At the bottom of the interface are "BACK" and "CLOSE WINDOW" buttons.

Please note that, as the author of this Elsevier article, you retain the right to include it in a thesis or dissertation, provided it is not published commercially. Permission is not required, but please ensure that you reference the journal as the original source. For more information on this and on your other retained rights, please visit: <https://www.elsevier.com/about/our-business/policies/copyright#Author-rights>

Copyright © 2019 Copyright Clearance Center, Inc. All Rights Reserved. [Privacy statement](#). [Terms and Conditions](#). Comments? We would like to hear from you. E-mail us at [customer@copyright.com](mailto:customer@copyright.com)

# References

- [1] R. R. Boyer and R. D. Briggs, “The Use of  $\beta$  Titanium Alloys in the Aerospace Industry,” *Journal of Materials Engineering and Performance*, vol. 14, no. 6, pp. 681–685, 2005.
- [2] Reuters, “Boeing makes planes heavier to save money,” 2015. [Online]. Available: <http://www.telegraph.co.uk/finance/newsbysector/transport/11761286/Boeing-makes-planes-heavier-to-save-money.html>
- [3] Y. Yamada, “Titanium Alloys for Springs,” in *Materials for Springs*, Y. Yamada, Ed. New York: Springer-Verlag Berlin Heidelberg, 2007, ch. 2.5, pp. 296 – 307.
- [4] N. S. Weston and M. Jackson, “FAST- forge - A new cost-effective hybrid processing route for consolidating titanium powder into near net shape forged components,” *Journal of Materials Processing Technology*, vol. 243, pp. 335–346, 2017.
- [5] E. L. Calvert, B. Wynne, and M. Jackson, “Exploitation of field-assisted sintering technology (FAST) to produce pre-forged billets from metastable beta titanium alloy powder,” *Key Engineering Materials*, vol. 716, pp. 800–816, 2016.
- [6] E. L. Calvert, B. Wynne, N. S. Weston, A. Tudball, and M. Jackson, “Thermomechanical processing of a high strength metastable beta titanium alloy powder, consolidated using the low-cost FAST-forge process,” *Journal of Materials Processing Technology*, vol. 254, pp. 158–170, 2018.
- [7] E. L. Calvert, A. J. Knowles, J. J. Pope, D. Dye, and M. Jackson, “Novel high strength titanium-titanium composites produced using field-assisted sintering technology (FAST),” *Scripta Materialia*, vol. 159, pp. 51–57, 2019.
- [8] G. Lütjering and J. Williams, “Introduction,” in *Titanium*, 2nd ed., B. Derby, Ed. Berlin: Springer-Verlag Berlin Heidelberg, 2007, ch. 1, pp. 1–14.
- [9] M. Peters, J. Hemptenmacher, J. Kumpfert, and C. Leyens, “Structure and Properties of Titanium and Titanium Alloys,” in *Titanium and Titanium Alloys: Fundamentals and*

- Applications*, C. Leyens and M. Peters, Eds. Weinheim: Wiley-VCH Verlag GmbH & Co. KGaA, 2003, ch. 1, pp. 1–36.
- [10] Questionbase.50megs.com, “AS Chemistry - Revision Notes,” 2013. [Online]. Available: <http://lanther.co.uk/notes/CHM2.pdf>
- [11] M. Donachie Jr, “Ingot Metallurgy and Mill Products,” in *Titanium: A Technical Guide*, 2nd ed. Ohio: ASM International, 2000, ch. 4, pp. 25–32.
- [12] W. D. Callister Jr, “Dislocations and Strengthening Mechanisms,” in *Materials Science and Engineering: An Introduction*, 7th ed. New York: John Wiley & Sons Inc, 2007, ch. 7, pp. 174–206.
- [13] G. Lütjering and J. Williams, “Fundamental Aspects,” in *Titanium*, 2nd ed., B. Derby, Ed. Berlin: Springer-Verlag Berlin Heidelberg, 2007, ch. 2, pp. 15–52.
- [14] N. G. Jones, “Microstructural Evolution of Ti-5Al-5Mo-5V-3Cr,” Ph.D. dissertation, Imperial College London, 2008.
- [15] F. Humphreys and M. Hatherly, “Grain growth following recrystallization,” in *Recrystallization and Related Annealing Phenomena*, 2nd ed. Oxford: Elsevier Ltd., 2004, ch. 11, pp. 333–378.
- [16] G. Lütjering and J. Williams, “Commercially Pure (CP) Titanium and Alpha Alloys,” in *Titanium*, 2nd ed., B. Derby, Ed. Berlin: Springer-Verlag Berlin Heidelberg, 2007, ch. 4, pp. 174–201.
- [17] R. S. Mohan, S. Krishna, and C. M. Ramesh, “A Comparative Study of Aluminium Alloy and Titanium Alloy,” *International Journal on Recent Technologies in Mechanical and Electrical Engineering*, vol. 2, no. 8, pp. 85–88, 2015.
- [18] G. Lütjering and J. C. Williams, “High Temperature Alloys,” in *Titanium*, 2nd ed., B. Derby, Ed. Berlin: Springer-Verlag Berlin Heidelberg, 2007, ch. 6, pp. 259–282.
- [19] M. Donachie Jr, “Understanding the Metallurgy of Titanium,” in *Titanium: A Technical Guide*, 2nd ed. Ohio: ASM International, 2000, ch. 3, pp. 13–24.
- [20] G. Lütjering and J. Williams, “Alpha + Beta Alloys,” in *Titanium*, 2nd ed., B. Derby, Ed. Berlin: Springer-Verlag Berlin Heidelberg, 2007, ch. 5, pp. 203–258.



- [21] G. Terlinde and G. Fischer, “Beta Titanium Alloys,” in *Titanium and Titanium Alloys: Fundamentals and Applications*, C. Leyens and M. Peters, Eds. Weinheim: Wiley-VCH Verlag GmbH & Co. KGaA, 2003, ch. 2, pp. 37–57.
- [22] G. Lütjering and J. Williams, “Beta Alloys,” in *Titanium*, 2nd ed., B. Derby, Ed. Berlin: Springer-Verlag Berlin Heidelberg, 2007, ch. 7, pp. 283 – 336.
- [23] J. D. Cotton, R. D. Briggs, R. R. Boyer, S. Tamirisakandala, P. Russo, N. Shchetnikov, and J. C. Fanning, “State of the Art in Beta Titanium Alloys for Airframe Applications,” *JOM*, vol. 67, no. 6, pp. 1281–1303, 2015.
- [24] H. M. Flower, “Microstructural development in relation to hot working of titanium alloys,” *Materials Science and Technology*, vol. 6, pp. 1082–1092, 1990.
- [25] S. Nyakana, J. Fanning, and R. Boyer, “Quick Reference Guide for  $\beta$  Titanium Alloys in the 00s,” *Journal of Materials Engineering and Performance*, vol. 14, no. 6, pp. 799–811, 2005.
- [26] N. G. Jones, R. J. Dashwood, D. Dye, and M. Jackson, “Thermomechanical processing of Ti-5Al-5Mo-5V-3Cr,” *Materials Science and Engineering: A*, vol. 490, pp. 369–377, 2008.
- [27] Titanium Metals Corporation, “TIMET Articles: Sponge Production,” 2013. [Online]. Available: <http://www.timet.com/component/content/article/14-titanium-101/43-sponge-production>
- [28] Titanium Metals Corp., “TIMET Articles: Vacuum Arc Remelt Process,” 2013. [Online]. Available: <http://www.timet.com/component/content/article/14-titanium-101/44-var-vacuum-arc-remelt-process>
- [29] E. Kraft, “Summary of Emerging Titanium Cost Reduction Technologies,” EHK Technologies, Vancouver, WA., Tech. Rep., 2004.
- [30] M. Donachie Jr, “Relationships among Structures, Processing, and Properties,” in *Titanium: A Technical Guide*, 2nd ed. Ohio: ASM International, 2000, ch. 12, pp. 95–121.
- [31] S. K. Kar, S. Suman, S. Shivaprasad, A. Chaudhuri, and A. Bhattacharjee, “Processing-microstructure-yield strength correlation in a near  $\beta$  Ti alloy, Ti-5Al-5Mo-5V-3Cr,” *Materials Science and Engineering A*, vol. 610, pp. 171–180, 2014.
- [32] S. K. Sikka, Y. K. Vohra, and R. Chidambaram, “Omega Phase in Materials,” *Progress in Materials Science*, vol. 27, pp. 245–310, 1982.

- [33] S. Nag, R. Banerjee, R. Srinivasan, J. Y. Hwang, M. Harper, and H. L. Fraser, “Omega-Assisted nucleation and growth of alpha precipitates in the Ti-5Al-5Mo-5V-3Cr-0.5Fe beta titanium alloy,” *Acta Materialia*, vol. 57, pp. 2136–2147, 2009.
- [34] J. Coakley, V. A. Vorontsov, N. G. Jones, A. Radecka, P. A. Bagot, K. C. Littrell, R. K. Heenan, F. Hu, A. P. Magyar, D. C. Bell, and D. Dye, “Precipitation processes in the Beta-Titanium alloy Ti-5Al-5Mo-5V-3Cr,” *Journal of Alloys and Compounds*, vol. 646, pp. 946–953, 2015.
- [35] A. Dehghan-Manshadi and R. J. Dippenaar, “Development of  $\alpha$ -phase morphologies during low temperature isothermal heat treatment of a Ti-5Al-5Mo-5V-3Cr alloy,” *Materials Science and Engineering: A*, vol. 528, pp. 1833–1839, 2011.
- [36] N. Clément, A. Lenain, and P. J. Jacques, “Mechanical Property Optimization via Microstructural Control of New Metastable Beta Titanium Alloys,” *JOM*, pp. 50–53, 2007.
- [37] N. Jones, R. Dashwood, D. Dye, and M. Jackson, “The Flow Behavior and Microstructural Evolution of Ti-5Al-5Mo-5V-3Cr during Subtransus Isothermal Forging,” *Metallurgical and Materials Transactions A*, vol. 40, pp. 1944–1954, 2009.
- [38] S. Grasso and M. Reece, “High-Tech Sintering,” 2012. [Online]. Available: <http://www.ceramicindustry.com/articles/92601-high-tech-sintering>
- [39] M. Suárez, A. Fernández, J. L. Menéndez, R. Torrecillas, H. U. Kessel, J. Hennicke, R. Kirchner, and T. Kessel, “Challenges and Opportunities for Spark Plasma Sintering: A Key Technology for a New Generation of Materials,” in *Sintering Applications*, B. Ertug, Ed. InTech, 2013, ch. 13, pp. 319 – 342.
- [40] Fraunhofer Gesellschaft, “Spark Plasma Sintering System,” 2015. [Online]. Available: <http://www.ifam.fraunhofer.de/en/Dresden/technologien/Formgebung/spark{-}plasma{-}sinteranlage.html>
- [41] Fuji Electronic Industrial Co. Ltd, “Principles and Mechanism of the SPS Process,” 2015. [Online]. Available: <http://sps.fdc.co.jp/whats/whats4.html>
- [42] M. Zadra, F. Casari, L. Girardini, and A. Molinari, “Microstructure and mechanical properties of cp-titanium produced by spark plasma sintering,” *Powder Metallurgy*, vol. 51, no. 1, pp. 59–65, 2008.

- [43] Z. A. Munir, U. Anselmi-Tamburini, and M. Ohyanagi, "The effect of electric field and pressure on the synthesis and consolidation of materials: A review of the spark plasma sintering method," *Journal of Materials Science*, vol. 41, pp. 763–777, 2006.
- [44] W. Chen, U. Anselmi-Tamburini, J. Garay, J. Groza, and Z. Munir, "Fundamental investigations on the spark plasma sintering/synthesis process I. Effect of dc pulsing on reactivity," *Materials Science and Engineering A*, vol. 394, pp. 132–138, 2004.
- [45] N. Saheb, Z. Iqbal, A. Khalil, A. S. Hakeem, N. Al Aqeeli, T. Laoui, A. Al-Qutub, and R. Kirchner, "Spark plasma sintering of metals and metal matrix nanocomposites: A review," *Journal of Nanomaterials*, vol. 2012, pp. 1–13, 2012.
- [46] Thermal Technology LLC, "Spark Plasma Sintering (SPS/DCS)," 2015. [Online]. Available: <http://www.thermaltechnology.com/spark-plasma-sintering.html>
- [47] F. Zhang, M. Reich, O. Kessler, and E. Burkel, "The potential of rapid cooling spark plasma sintering for metallic materials," *Materials Today*, vol. 16, no. 5, pp. 192–197, 2013.
- [48] Z. A. Munir, D. V. Quach, and M. Ohyanagi, "Electric Current Activation of Sintering: A Review of the Pulsed Electric Current Sintering Process," *Journal of the American Ceramic Society*, vol. 94, no. 1, pp. 1–19, 2011.
- [49] Y. An and W. Lee, "Synthesis of porous titanium implants by environmental-electro-discharge-sintering process," *Materials Chemistry and Physics*, vol. 95, pp. 242–247, 2006.
- [50] Y. Quan, F. Zhang, H. Rebl, B. Nebe, O. Keßler, and E. Burkel, "Ti-6Al-4V foams fabricated by spark plasma sintering with post-heat treatment," *Materials Science and Engineering A*, vol. 565, pp. 118–125, 2013.
- [51] S. S. Dheda, Y. K. Kim, C. Melnyk, W. Liu, and F. A. Mohamed, "Corrosion and in vitro biocompatibility properties of cryomilled-spark plasma sintered commercially pure titanium," *Journal of Materials Science: Materials in Medicine*, vol. 24, pp. 1239–1249, 2013.
- [52] D. Handtrack, C. Sauer, and B. Kieback, "Microstructure and properties of ultrafine-grained and dispersion- strengthened titanium materials for implants," *Journal of Materials Science*, vol. 43, pp. 671–679, 2008.

- [53] D. Handtrack, F. Despang, C. Sauer, B. Kieback, N. Reinfried, and Y. Grin, “Fabrication of ultra-fine grained and dispersion-strengthened titanium materials by spark plasma sintering,” *Materials Science and Engineering A*, vol. 437, pp. 423–429, 2006.
- [54] F. Watari, A. Yokoyama, M. Omori, T. Hirai, H. Kondo, M. Uo, and T. Kawasaki, “Biocompatibility of materials and development to functionally graded implant for biomedical application,” *Composites Science and Technology*, vol. 64, pp. 893–908, 2004.
- [55] G. Xie, F. Qin, and S. Zhu, “Recent Progress in Ti-Based Metallic Glasses for Application as Biomaterials,” *Materials Transactions*, vol. 54, no. 8, pp. 1314–1323, 2013.
- [56] K. Yoshida, H. Mishina, S. Sasaki, M. Morita, and K. Mabuchi, “Mechanical Properties of Titanium Cermets for Joint Prostheses,” *Materials Transactions*, vol. 47, no. 2, pp. 418–425, 2006.
- [57] A. Couret, G. Molénat, J. Galy, and M. Thomas, “Microstructures and mechanical properties of TiAl alloys consolidated by spark plasma sintering,” *Intermetallics*, vol. 16, pp. 1134–1141, 2008.
- [58] K. Crosby, L. L. Shaw, C. Estournes, G. Chevallier, A. W. Fliflet, and M. A. Imam, “Enhancement in Ti-6Al-4V sintering via nanostructured powder and spark plasma sintering,” *Powder Metallurgy*, vol. 57, no. 2, pp. 147–154, 2014.
- [59] M. Eriksson, Z. Shen, and M. Nygren, “Fast densification and deformation of titanium powder,” *Powder Metallurgy*, vol. 48, no. 3, pp. 231–236, 2005.
- [60] O. Ertorer, T. D. Topping, Y. Li, W. Moss, and E. J. Lavernia, “Nanostructured Ti consolidated via spark plasma sintering,” *Metallurgical and Materials Transactions A*, vol. 42, pp. 964–973, 2011.
- [61] A. Pettersson, P. Magnusson, P. Lundberg, and M. Nygren, “Titanium-titanium diboride composites as part of a gradient armour material,” *International Journal of Impact Engineering*, vol. 32, pp. 387–399, 2005.
- [62] N. Vicente Jr, C. Menapace, and A. Molinari, “Hot Deformation of the Ti-6Al-4V Alloy Preform Obtained by Spark Plasma Sintering of Powders,” in *21st Brazilian Congress of Mechanical Engineering*, 2011.
- [63] C. Menapace, N. Vicente Jr, and A. Molinari, “Hot forging of Ti-6Al-4V alloy preforms produced by spark plasma sintering of powders,” *Powder Metallurgy*, vol. 56, no. 2, pp. 102–110, 2013.

## REFERENCES

---

- [64] N. S. Weston, F. Derguti, A. Tudball, and M. Jackson, “Spark plasma sintering of commercial and development titanium alloy powders,” *Journal of Materials Science*, vol. 50, pp. 4860–4878, 2015.
- [65] G. Terlinde, T. Witulski, and G. Fischer, “Forging of Titanium,” in *Titanium and Titanium Alloys: Fundamentals and Applications*, C. Leyens and M. Peters, Eds. Weinheim: Wiley-VCH Verlag GmbH & Co. KGaA, 2003, ch. 11, pp. 289–304.
- [66] M. Jackson, R. Dashwood, L. Christodoulou, and H. Flower, “The microstructural evolution of near beta alloy Ti-10V-2Fe-3Al during subtransus forging,” *Metallurgical and Materials Transactions A*, vol. 36, pp. 1317–1327, 2005.
- [67] W. Rasband, “ImageJ 1.46r Image Analysis Software,” Bethesda, Maryland, 1997.
- [68] Buehler, “Omnimet Capture Advanced 9.5 Image Analysis Software.” [Online]. Available: <https://shop.buehler.com/digital-imaging-image-analysis>
- [69] F. Cervera, “Thermal Expansion,” in *Thermal Properties of Metals*. Ohio: ASM International, 2002, ch. 2, pp. 9–220.
- [70] S. B. Davenport, N. J. Silk, C. N. Sparks, and C. M. Sellars, “Development of constitutive equations for modelling of hot rolling,” *Materials Science and Technology*, vol. 16, no. 5, pp. 539–546, 2000.
- [71] G. Dieter, “Hot Compression Testing,” in *Handbook of Workability and Process Design*, 1st ed., G. Dieter, H. Kuhn, and S. L. Semiatin, Eds. Ohio: ASM International, 2003, ch. 6, pp. 61–67.
- [72] Scientific Forming Technologies Corporation, “DEFORM 11.0.1.” Columbus, Ohio, 2016.
- [73] V. Wagner, M. Baili, G. Dessein, and D. Lallement, “Experimental Characterization of Behavior Laws for Titanium Alloys: Application to Ti-5553,” *Key Engineering Materials*, vol. 446, pp. 147–155, 2010.
- [74] J. Fluhner, “DEFORM TM-2D Version 8.02 User’s Manual,” 2004.
- [75] K. H. Grote and E. K. Antonsson, *Springer Handbook of Mechanical Engineering*. Springer-Verlag Berlin Heidelberg, 2009.
- [76] I. Weiss and S. L. Semiatin, “Thermomechanical processing of beta titanium alloys - an overview,” *Materials Science and Engineering A*, vol. 243, pp. 46–65, 1998.

- [77] M. Long and H. Rack, “High Temperature Discontinuous Yielding in beta-phase Ti3Al-(Nb,V,Mo) Alloys,” in *Titanium '95: Science and Technology*, P. Blenkinsop, W. Evans, and H. Flower, Eds. Institute of Materials, 1995, pp. 316 – 323.
- [78] N. G. Jones and M. Jackson, “On mechanism of flow softening in Ti-5Al-5Mo-5V-3Cr,” *Materials Science and Technology*, vol. 27, no. 6, pp. 1025–1032, 2011.
- [79] G. Dieter Jr, “Plastic deformation of single crystals,” in *Mechanical Metallurgy*. New York: McGraw-Hill Book Company, 1961, ch. 4, pp. 81 – 117.
- [80] N. G. Jones, R. J. Dashwood, D. Dye, and M. Jackson, “Understanding the behaviour of Ti-5Al-5Mo-5V-3Cr during subtransus isothermal forging,” in *Ti-2011 Science and Technology*, 2011, pp. 8–11.
- [81] F. Humphreys and M. Hatherly, “The microstructures of deformed two-phase alloys,” in *Recrystallization and Related Annealing Phenomena*, 2nd ed. Oxford: Elsevier Ltd, 2004, ch. 2, pp. 48 – 65.
- [82] K. Hua, X. Xue, H. Kou, J. Fan, B. Tang, and J. Li, “Characterization of hot deformation microstructure of a near beta titanium alloy Ti-5553,” *Journal of Alloys and Compounds*, vol. 615, pp. 531–537, 2014.
- [83] B. Verlinden, J. Driver, I. Samajdar, and R. Doherty, “Work hardening,” in *Thermo-Mechanical Processing of Metallic Materials*, 1st ed., R. Cahn, Ed. Oxford: Elsevier Ltd, 2007, ch. 4, pp. 57 – 81.
- [84] M. D. Richardson, “Microstructural and Mechanical Property Development in Metastable Beta Titanium Alloys,” Ph.D. dissertation, University of Sheffield, 2016.
- [85] C. Zener and J. H. Hollomon, “Effect of Strain Rate Upon Plastic Flow of Steel,” *Journal of Applied Physics*, vol. 15, pp. 22–32, 1944.
- [86] J. J. Jonas, C. M. Sellars, and W. J. M. Tegart, “Strength and structure under hot-working conditions,” *Metallurgical Reviews*, vol. 14, no. 1, pp. 1–24, 1969.
- [87] M. Jackson, “Microstructural Evolution of Titanium Alloys During Isothermal Subtransus Forging,” Ph.D. dissertation, Imperial College London, 2002.
- [88] P. Bate, “An Application of Computer Modelling to Isothermal Forging,” in *Aerospace Materials Process Modelling: 65th Meeting of the Structures and Materials Panel of AGARD*. Essex: Specialised Printing Services Limited, 1988, pp. 1–10.

- [89] J. W. Brooks, “Processing Wrought Nickel and Titanium Superalloys,” in *Thermomechanical processing in theory, modelling and practice (TMP): International conference organized in celebration of the 75th anniversary of the Swedish Society for Materials Technology*. Stockholm: Swedish Society for Materials Processing, 1997, pp. 52–77.
- [90] P. L. Blackwell, J. W. Brooks, and P. S. Bate, “Development of microstructure in isothermally forged Nimonic alloy AP1,” *Materials Science and Technology*, vol. 14, no. 11, pp. 1181–1188, 1998.
- [91] T. Sheppard and J. Norley, “Deformation characteristics of Ti-6Al-4V,” *Materials Science and Technology*, vol. 4, pp. 903–908, 1988.
- [92] J. C. Fanning and R. R. Boyer, “Properties of TIMETAL 555 - A New Near-Beta Titanium Alloy for Airframe Components,” in *10TH, World Conference on Titanium; 2003; Hamburg, Germany*. Weinheim: Wiley-VCH, 2003, pp. 2643–2650.
- [93] Latrobe, “300M VAC-ARC Technical Data Sheet,” pp. 1–2, 2007.
- [94] Smiths, “BS S155 Technical Data Sheet,” p. 1, 2017.
- [95] N. Jones, R. Dashwood, M. Jackson, and D. Dye, “ $\beta$  Phase decomposition in Ti-5Al-5Mo-5V-3Cr,” *Acta Materialia*, vol. 57, pp. 3830–3839, 2009.
- [96] R. Leucht and H. J. Dudek, “Properties of SiC-fibre reinforced titanium alloys processed by fibre coating and hot isostatic pressing,” *Materials Science and Engineering A*, vol. 188, pp. 201–210, 1994.
- [97] K. M. Rahman, V. A. Vorontsov, S. M. Flitcroft, and D. Dye, “A High Strength Ti-SiC Metal Matrix Composite,” *Advanced Engineering Materials*, vol. 19, pp. 3–8, 2017.
- [98] S. Grützner, L. Krüger, M. Radajewski, and I. Schneider, “Characterization of in-situ TiB/TiC Particle-Reinforced Ti-5Al-5Mo-5V-3Cr Matrix Composites Synthesized by Solid-State Reaction with B<sub>4</sub>C and Graphite through SPS,” *Metals*, vol. 8, pp. 1–18, 2018.
- [99] W. B. Pearson, *Handbook of Lattice Spacings and Structures of Metals and Alloys, Vol. 2*. London: Pergamon Press, 1967.
- [100] A. J. Knowles, N. G. Jones, O. M. D. M. Messé, J. S. Barnard, C. N. Jones, and H. J. Stone, “Phase equilibria in the Fe-Mo-Ti ternary system at 1000C,” *Int. Journal of Refractory Metals and Hard Materials*, vol. 60, pp. 160–168, 2016.

## REFERENCES

---

- [101] A. J. Knowles, T. S. Jun, A. Bhowmik, N. G. Jones, T. B. Britton, F. Giuliani, H. J. Stone, and D. Dye, “A new beta titanium alloy system reinforced with superlattice intermetallic precipitates,” *Scripta Materialia*, vol. 140, pp. 71–75, 2017.
- [102] A. J. Knowles, N. G. Jones, C. N. Jones, and H. J. Stone, “Phase Equilibria in the Fe-Mo-Ti Ternary System at 1173 K (900C) and 1023 K (750C),” *Metallurgical and Materials Transactions A*, vol. 48A, pp. 4334–4341, 2017.
- [103] J. Roesler, H. Harders, and M. Baeker, “Strengthening Mechanisms,” in *Mechanical Behaviour of Engineering Materials: Metals, Ceramics, Polymers, and Composites*, 1st ed. New York: Springer-Verlag Berlin Heidelberg, 2007, pp. 198–223.
- [104] D. Poddar, “Solid-State Diffusion Bonding of Commercially pure Titanium and Precipitation Hardening Stainless steel,” *International Journal of Recent Trends in Engineering*, vol. 1, no. 5, pp. 93–99, 2009.
- [105] N. Jones, R. Dashwood, M. Jackson, and D. Dye, “Development of chevron-shaped  $\alpha$  precipitates in Ti5Al5Mo5V3Cr,” *Scripta Materialia*, vol. 60, no. 7, pp. 571–573, apr 2009.
- [106] G. I. Nosova, N. B. D’Yakonova, and I. V. Lyasotskii, “Metastable phases of electron type in titanium alloys with 3d-metals,” *Metal Science and Heat Treatment*, vol. 48, no. 9-10, pp. 427–432, 2006.
- [107] D. Tomus and H. P. Ng, “In situ lift-out dedicated techniques using FIB-SEM system for TEM specimen preparation,” *Micron*, vol. 44, pp. 115–119, 2013.
- [108] J. Andersson, T. Helander, L. Höglund, P. Shi, and B. Sundman, “Thermo-Calc and DICTRA, Computational tools for materials science,” *Calphad*, vol. 26, pp. 273–312, 2002.
- [109] S. Banerjee and P. Mukhopadhyay, “Occurrence of the omega phase,” in *Phase transformations: Examples from Titanium and Zirconium Alloys*, 1st ed. Oxford: Elsevier, 2007, ch. 6.2, pp. 475–484.
- [110] Y. Zheng, R. E. Williams, and H. L. Fraser, “Characterization of a previously unidentified ordered orthorhombic metastable phase in Ti-5Al-5Mo-5V-3Cr,” *Scripta Materialia*, vol. 113, pp. 202–205, 2016.



- [111] Y. X. Qin, W. J. Lu, X. F. Sheng, Z. F. Yang, and D. Zhang, “Mechanical Properties of in situ Synthesized Titanium Matrix Composites at Elevated Temperature,” *Materials Transactions*, vol. 44, no. 11, pp. 2282–2287, 2003.
- [112] W. D. Callister Jr, “Imperfections in Solids,” in *Materials Science and Engineering: An Introduction*, 7th ed. New York: John Wiley & Sons Inc, 2007, ch. 4, pp. 80–108.
- [113] F. J. Humphreys and M. G. Ardakani, “Grain boundary migration and zener pinning in particle-containing copper crystals,” *Acta Materialia*, vol. 44, no. 7, pp. 2717–2727, 1996.
- [114] M. Sabeena, S. Murugesan, R. Mythili, A. K. Sinha, M. N. Singh, M. Vijayalakshmi, and S. K. Deb, “Studies on  $\omega$  Phase Formation in Ti-Mo Alloys Using Synchrotron XRD,” *Transactions of the Indian Institute of Metals*, vol. 68, no. 1, pp. 1–6, 2015.
- [115] Y. Zheng, D. Huber, and H. L. Fraser, “Investigation of a nano-scale, incommensurate, modulated domain in a Ti-Fe alloy,” *Scripta Materialia*, vol. 154, pp. 220–224, 2018.
- [116] G. Lütjering and J. Williams, “Technological Aspects,” in *Titanium*, 2nd ed., B. Derby, Ed. Berlin: Springer-Verlag Berlin Heidelberg, 2007, ch. 3, pp. 53–173.
- [117] J. J. Pope, E. L. Calvert, N. S. Weston, and M. Jackson, “FAST-DB : A novel solid-state approach for diffusion bonding dissimilar titanium alloy powders for next generation critical components,” *Journal of Materials Processing Tech.*, vol. 269, pp. 200–207, 2019.